Persistent firing and oscillations in the septo-hippocampal system and their relation to locomotion

Karolína Korvasová

Information
Band / Volume 86
ISBN 978-3-95806-654-0

Mitglied der Helmholtz-Gemeinschaft

JÜLICH
Forschungszentrum

Schriften des Forschungszentrums Jülich
Reihe Information / Information Band / Volume 86

Forschungszentrum Jülich GmbH
Institute of Neurosciences and Medicine (INM)
Computational and Systems Neuroscience (INM-6)
& Theoretical Neuroscience (IAS-6)

Persistent firing and oscillations in the septo-hippocampal system and their relation to locomotion

Karolína Korvasová

Schriften des Forschungszentrums Jülich
Reihe Information / Information Band / Volume 86

ISSN 1866-1777 ISBN 978-3-95806-654-0

Bibliografische Information der Deutschen Nationalbibliothek.
Die Deutsche Nationalbibliothek verzeichnet diese Publikation in der
Deutschen Nationalbibliografie; detaillierte Bibliografische Daten
sind im Internet über http://dnb.d-nb.de abrufbar.

Herausgeber und Vertrieb:	Forschungszentrum Jülich GmbH Zentralbibliothek, Verlag 52425 Jülich Tel.: +49 2461 61-5368 Fax: +49 2461 61-6103 zb-publikation@fz-juelich.de www.fz-juelich.de/zb
Umschlaggestaltung:	Grafische Medien, Forschungszentrum Jülich GmbH
Druck:	Grafische Medien, Forschungszentrum Jülich GmbH
Copyright:	Forschungszentrum Jülich 2022

Schriften des Forschungszentrums Jülich
Reihe Information / Information, Band / Volume 86

D 82 (Diss. RWTH Aachen University, 2022)

ISSN 1866-1777
ISBN 978-3-95806-654-0

Vollständig frei verfügbar über das Publikationsportal des Forschungszentrums Jülich (JuSER)
unter www.fz-juelich.de/zb/openaccess.

To my family.

Summary

The medial septum, diagonal band of Broca has received most attention as a putative pacemaker of the hippocampal theta rhythm. However, due to its high interconnectivity with various cortical and subcortical regions, the medial septum is involved in a variety of neural processes. This thesis focuses on the relation between medial septal spiking activity, hippocampal theta rhythm and locomotion. It was previously demonstrated that theta-periodic optogenetic activation of medial septal glutamatergic neurons entrains hippocampal theta oscillation and initiates persistent locomotion of the animal. We showed that hippocampal theta oscillation and locomotion, both persisting after the stimulus offset, can be induced by a brief continuous light stimulation of medial septal glutamatergic neurons. The hippocampal theta rhythm is not necessary for inducing persistent locomotion, as locomotion initiation is not affected by blocking synaptic transmission in the medial septum that abolishes the hippocampal theta. Furthermore, we observed persistent spiking activity of the medial septal neurons, lasting for many seconds after the stimulus offset. To test whether the persistent activity is generated locally in the medial septum, we repeated the stimulation experiment in an acute medial septal slice preparation. The persistent activity had a shorter duration than in vivo, but was present both in the intact slice and with blocked synaptic transmission, indicating that the persistent firing is a result of intrinsic dynamics of medial septal glutamatergic neurons. Further analysis of spontaneous spiking activity of neurons in the acute medial septal slice preparation revealed the existence of theta-rhythmic neurons that synchronize their firing, suggesting that the medial septum can generate the theta oscillation independently of external feedforward and feedback input. Even though medial septal synaptic connectivity is necessary for the hippocampal theta rhythm, our results suggest that the theta-rhythmic firing is a result of intrinsic cellular dynamics and a low level of synchrony can be achieved without synaptic coupling. It remains an open question how the septal theta-rhythmic input is transformed into a travelling theta wave observed in the hippocampus. The last part of the thesis offers a framework for studying the generation of periodic travelling waves in spiking neural networks. We developed a parameter mapping between a discrete network of neurons and a population model that describes the spatio-temporal spread of activity as a continuous process. Using this mapping, we derived conditions for the existence of periodic travelling waves in the spiking neural network.

Zusammenfassung

Das mediale Septum, diagonales Band von Broca, hat die meiste Aufmerksamkeit als mutmaßlicher Schrittmacher des im Hippocampus auftretenden Theta Rhythmus erhalten. Aufgrund seiner hohen Interkonnektivität mit verschiedenen kortikalen und subkortikalen Regionen ist das mediale Septum jedoch an einer Vielzahl von neuronalen Prozessen beteiligt. Diese Arbeit konzentriert sich auf die Beziehung zwischen Spiking-Aktivität des medialen Septums, Theta-Rhythmus des Hippocampus und Bewegung. In der Vergangenheit wurde gezeigt, dass die theta-periodische optogenetische Aktivierung glutamaterger Neuronen im medialen Septum die Theta-Oszillation des Hippocampus mitreißt und eine anhaltende Bewegung des Tieres initiiert. Wir zeigten, dass Theta-Oszillation des Hippocampus und Bewegung, die beide nach dem Stimulus-Offset anhalten, durch eine kurze kontinuierliche Lichtstimulation glutamaterger Neuronen im medialen Septum induziert werden können. Die Präsenz des Theta-Rhythmus im Hippocampus ist dabei für die Induktion anhaltender Bewegung nicht notwendig, da die Initiierung der Bewegung durch die Blockierung der synaptischen Übertragung im medialen Septum, die den Theta-Rhytmus aufhebt, nicht beeinflusst wird. Darüber hinaus beobachteten wir anhaltende Spiking-Aktivität der Neuronen im medialen Septum, die viele Sekunden nach dem Stimulus-Offset anhielt. Um zu testen, ob die anhaltende Aktivität lokal im medialen Septum erzeugt wird, wiederholten wir das Stimulationsexperiment in einem akuten medialen Septumschnittpräparat. Die anhaltende Aktivität hatte eine kürzere Dauer als in vivo, war aber sowohl in dem intakten Schnitt als auch bei blockierter synaptischer Übertragung vorhanden, was darauf hindeutet, dass die anhaltende Aktivität ein Ergebnis der intrinsischen Dynamik der glutamatergen Neuronen des medialen Septums ist. Weitere Analysen der spontanen Spiking-Aktivität von Neuronen in der akuten medialen Septum-Präparation zeigten die Existenz von theta-rhythmischen Neuronen, die ihr Feuern synchronisieren, was darauf hindeutet, dass das mediale Septum die Theta-Oszillation unabhängig von externem Feedforward- und Feedback-Input erzeugen kann. Obwohl die synaptische Konnektivität des medialen Septums für den Theta-Rhythmus des Hippocampus notwendig ist, deuten unsere Ergebnisse darauf hin, dass das theta-rhythmische Feuern ein Ergebnis intrinsischer Dynamik der Zellen ist und ein geringer Grad an Synchronisation auch ohne synaptische Kopplung erreicht werden kann. Es bleibt eine offene Frage, wie der septale theta-rhythmische Input in eine wandernde Theta-Welle umgewandelt wird, welche im Hippocampus bereits beobachtet wurde. Der letzte Teil der

Arbeit behandelt ein Rahmenwerk, mit welchem die Erzeugung von periodischen, sich ausbreitenden Wellen in gepulsten neuronalen Netzwerken (auch aus dem Englischen “Spiking Neural Networks”) untersucht werden kann . Wir entwickelten ein Parameter-Mapping zwischen einem diskreten Netzwerk von Neuronen und einem Populationsmodell, das die räumlich-zeitliche Ausbreitung der Aktivität als einen kontinuierlichen Prozess beschreibt. Unter Verwendung dieses Mappings haben wir Bedingungen für die Existenz periodischer, sich ausbreitender Wellen im gepulsten neuronalen Netzwerk abgeleitet.

I am very grateful to many people that helped me and supported me during my PhD. I learned a lot from them both on the professional and personal level.

First of all, I thank Tom Tetzlaff for guiding me through my entire PhD, for many hours he spent discussing various topics with me, for his patience, friendly approach and the support he gave me.

I thank Sanja Bauer Mikulovic for introducing me to the world of experimental neuroscience, for her active involvement, inspiration, heartfelt support and for encouraging me to pursue a scientific career.

I thank Stefan Remy for his trust, open-mindedness and support. I very much appreciate all the discussions we had throughout the years that were very eye-opening for me.

I thank Markus Diesmann for his active interest in the work of every member of his group and for creating a friendly and motivational atmosphere in the group meetings.

I am thankful to Markus Diesmann, Sonja Grün and Abigail Morrison for giving me the opportunity to enter the field of computational neuroscience and work in a very stimulating environment with family-like atmosphere. I am very grateful that I could combine the professional and maternal role.

I thank Johanna Senk for her understanding when she had to take on some of my work due to my parental leave. All the hours we spent working together were very enjoyable for me.

I thank Moritz Helias for his supervision of part of my work and for creating a friendly atmosphere.

I thank Björn Kampa, Markus Diesmann and Stefan Remy for their feedback to my work and for reviewing my thesis.

I also thank David Berling for his help with translating the summary of the thesis to German.

Last but not least, I thank my husband Matěj and my children Šimon and Tatiana for their love and support.

Contents

1 Introduction

1.1 The function of brain oscillations

Brain oscillations have been discovered almost a century ago by Hans Berger (Berger, 1929), the inventor of electroencephalography (EEG). Driven by his interest in telepathy (Buzsáki, 2009), he recorded EEG activity from the occipital lobe of a human subject and noticed strong power around 10 Hz when the subject's eyes were closed. With the eyes open, he observed a faster oscillation with frequency around 30 Hz. By giving these two rhythms the names "alpha" and "beta", he initiated the convention to call brain rhythms by Greek letters. Since then, oscillations in various frequencies have been described across the whole brain and measured by both non-invasive and invasive techniques. In humans, the following main frequency bands are distinguished: delta (0.5-4 Hz), theta (4-8 Hz), alpha (8-12 Hz), beta (12-30 Hz) and gamma (30-100 Hz) (Buzsáki, 2009), each with different behavioural correlates, mechanisms of generation and brain regions where they occur (Buzsáki, 2019).

Alterations of oscillatory activity have been reported in many psychiatric diseases (for a review see Buzsáki and Watson, 2012). Moreover, the induction of brain oscillation by various techniques modulates behavioural performance such as memory (Turnbull et al., 1994; McNaughton et al., 2006; Shirvalkar et al., 2010; Lipponen et al., 2012), attention (Dugué et al., 2015) or response time in a visual task (Bosman et al., 2012). Despite a large body of evidence that the occurence and properties of brain oscillations correlate with behavioural states and performance, the question whether oscillations are an epiphenomenon or have a functional role is still under debate (Singer, 2018; Sejnowski and Paulsen, 2006). According to a broadly accepted view, the brain oscillations organize transfer of spiking activity and thereby facilitate communication between neural populations on different scales, from local cell assemblies to whole brain areas (Singer, 1999, 2000; Buzsáki, 2009). The slow oscillations (e.g. theta) are generally thought to organize long-range communication and the fast oscillations (e.g. gamma) short-range communication (Buzsáki et al., 2013), although gamma-band synchronization was also observed between distant ar-

eas (Gregoriou et al., 2015). A different view on the origin of coherence between areas was recently formulated by Schneider et al. (2020). According to their model, coherence of two brain areas can be caused by synchronously firing neurons in one area that send output back to the same area as well as to some other area. Penttonen and Buzsáki (2003) noticed that the mean frequencies of the different frequency bands are equidistantly distributed on the natural logarithmic axis. According to their hypothesis, the non-rational relationship between the different frequencies ensures that they can serve as distinct communication channels that do not interfere. In general, synchrony increases robustness and efficiency of communication, at the expense of information processing capacity (Buzsáki and Watson, 2012; Pryluk et al., 2019). The binding role of oscillations has been extensively discussed in the context of visual processing. The gamma oscillation in the visual cortex has long been considered as the mechanism for the binding of visual features (Singer, 1999; Gray, 1999; Singer and Gray, 1995). However, even here concerns were raised (Ray and Maunsell, 2010) due to the dependence of the gamma frequency on visual contrast (Bartoli et al., 2019), leading to occurence of different frequencies in response to visual stimuli with non-homogeneous contrast. In the context of the hippocampus, gamma frequency variations were interpreted as a routing mechanism (Colgin et al., 2009).

There is also a debate about the direct influence of oscillations in the local field potential on activity of neurons. According to the traditional view, oscillations visible in the local field potential are regarded as a footprint of synchronized oscillatory activity of a group of neurons, rather than a functional system itself. However, some evidence for a direct influence of the field potential changes along the cell membrane, so called ephaptic coupling, on brain's function was found. Anastassiou et al. (2011) showed that ephaptic coupling of cortical neurons (changes in membrane potential caused by voltage changes in the extra-cellular space along the cell membrane) can affect precise spike timing, and therefore possibly modulate the level of synchrony and information transfer. Even more striking is the observation of Iaccarino et al. (2016) that the induction of gamma oscillation, but not other frequencies, activated microglia to remove amyloid plaques in mice, suggesting a possible coupling between brain oscillations and the immune system.

If a population of asynchronously active neurons receives correlated input, only those neurons with membrane potential sufficiently close to the threshold will respond with an action potential. However, if the post-synaptic neurons are synchronized, the incoming input will either result in a strong response by majority of neu-

rons if their membrane potentials are close to the threshold, or no response at all in the opposite case. Such routing mechanism is called "communication by coherence" (McLelland and VanRullen, 2016). According to this concept, the phase alignment of a slow oscillation (e.g. theta) with a faster oscillation (e.g. gamma) selects the representation to be attended. Moreover, the amplitude of the faster oscillation can be modulated by the phase of the slower oscillation, a phenomenon called "cross-frequency coupling" (Fries, 2005; Lisman and Jensen, 2013; Canolty and Knight, 2010). Some experimental studies suggested that the strength of cross-frequency coupling predicts behavioural performance for instance in mnemonic (Händel and Haarmeier, 2009) or visual tasks (Köster et al., 2018). Based on these two concepts, two mechanisms for simultaneous representations of multiple items, so called multiplexing, have been defined (McLelland and VanRullen, 2016): LJ-multiplexing and F-multiplexing (Figure 1.1 adapted from McLelland and VanRullen (2016)). The LJ-multiplexing, named after John E. Lisman and Ole Jensen, proposes that all items, each corresponding to one period of the faster oscillation, are represented in one period of the slower oscillations, whereby more strongly activated ensembles will participate at earlier phases than less strongly activated ensembles. The F-multiplexing corresponds to communication through coherence and was named after Pascal Fries. Here, only one item defined by the faster oscillation will be represented in a single cycle of the slower oscillation and the item is chosen based on phase-alignment. Some studies suggested that cross-frequency coupling and communication by coherence are two complementary multiplexing mechanisms that coexist and facilitate each other (McLelland and VanRullen, 2016; González et al., 2020).

1.2 The hippocampal theta oscillation

One of the most prominent brain rhythms is the hippocampal theta oscillation (7–14 Hz), typically recorded in the hippocampal CA1 region, but present in the whole hippocampus (Lubenov and Siapas, 2009; Buzsáki, 2002; Mikulovic et al., 2018; Goyal et al., 2020; López-Madrona et al., 2020) and beyond (Paz et al., 2008; O'Neill et al., 2013; Spaak and de Lange, 2020; Quilichini et al., 2010; Fournier et al., 2020). However, also other types of theta oscillations were reported in the cerebral cortex, unrelated to the hippocampal theta rhythm (Cashdollar et al., 2009). The hippocampal theta oscillation was initially associated with arousal (Green and Arduini, 1954; Petsche et al., 1962), but later many other behavioural correlates were identified, such as orienting, voluntary movement, anxiety, motivation, mem-

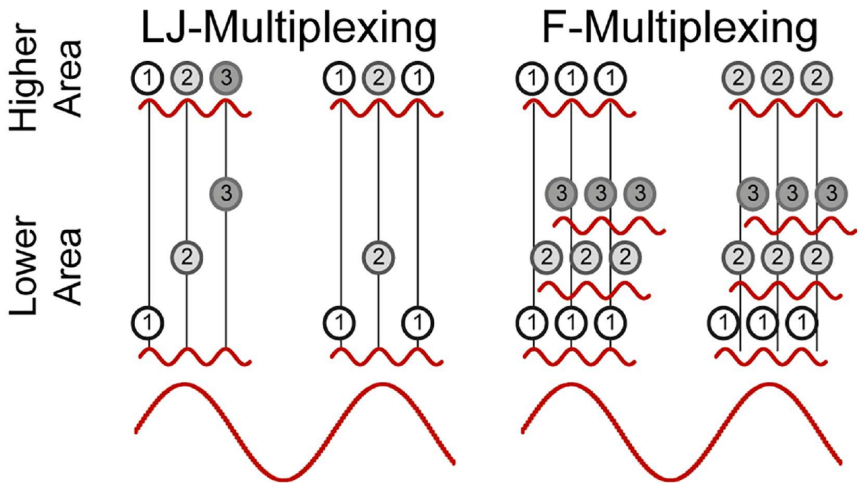

Figure 1.1: **Illustration of multiplexing mechanisms.** LJ-Multiplexing based on cross-frequency coupling (left) and F-multiplexing based on communication through coherence (right). In LJ-multiplexing, all items are represented in a single cycle of the slower oscillations, each corresponding to one cycle of the faster oscillation. In F-multiplexing, only a single item is represented during a single cycle of the slower oscillation. Here, each item is associated with a different phase of the faster oscillation and the one that is best aligned with the slower oscillation is chosen in every cycle of the slow oscillation. Adapted from McLelland and VanRullen (2016) with permission from PLOS Computational Biology.

ory or decision making (Buzsáki, 2005). Over 1500 experiments have been published that tried to identify the behavioural correlates of the hippocampal theta rhythm, without reaching a clear conclusion (Buzsáki, 2005). In the last decades, the theta rhythm has received most attention in the context of spatial navigation (Bose and Recce, 2001; Tingley and Buzsáki, 2018; Wang et al., 2015; Fuhrmann et al., 2015). The hippocampal pyramidal neurons, known as place cells, fire selectively at certain locations in the environment, so called place fields. Place cells were originally discovered in rodents (O'Keefe and Dostrovsky, 1971; O'Keefe, 1976), and later confirmed in humans (Ekstrom et al., 2003). Each place cell starts to fire when the animal enters its place field, with increasing firing rate as the animal progresses towards the center of the place field. The cell becomes silent again as the animal leaves its place field. Moreover, the place cell firing is organized by the theta oscillation. A place cell starts firing at a late phase of the theta cycle and the phase of locking systematically decreases as the animal traverses the correspoding place field, a phenomenon called phase precession (O'Keefe and Recce, 1993). This mechanism is thought to result from short-term synaptic depression and facilitation (Wang et al., 2015) and ensures that the order of place cells firing is preserved in each theta cycle (Skaggs et al., 1996). In rodents, both the frequency and power of the theta oscillation were thought to correlate with the speed of locomotion (McFarland et al., 1975). Contrary to this traditional view, Kropff et al. (2021) argue in a recent study that the frequency of theta oscillations correlates with positive acceleration, rather than speed. In humans, the movement onset is associated with an increase of both low and high theta power and the power is greater before and during longer translational paths, compared to shorter ones (Bush et al., 2017). Notably, the frequency of the theta rhythm in humans during virtual navigation is slower than during real navigation (Bohbot et al., 2017), challenging the view that the theta oscillation is generally slower in humans than in rodents (Jacobs, 2014). In the absence of the theta oscillation, the activity of place cells is mostly governed by sensory input (Wang et al., 2015). The function of the theta oscillation in facilitating inter-areal communication is nicely illustrated by the results of Fournier et al. (2020) who demonstrated that the activity of the mouse primary visual cortex during navigation in a virtual reality is modulated by the hippocampal theta oscillation. Moreover, Fournier et al. (2020) found neurons in the primary visual cortex that encode spatial position and show phase precession with respect to the theta rhythm.

According to Buzsáki (2002), the theta oscillation represents an online state of the hippocampus, a signal to cortical areas that it is ready to receive and process

information. The incoming information is then parsed into windows created by the theta oscillation (Lisman and Jensen, 2013; Buzsáki, 2019). The hypothesis of theta signal acting as a parser for neocortical messages is largely based on the discovery of cross-frequency coupling between the hippocampal theta and gamma oscillations (Bragin et al., 1995; Buzsáki et al., 2003; Tort et al., 2008). The gamma sequences represent the incoming messages from the neocortex that are temporally organized by the theta rhythm (Lisman and Jensen, 2013). The strength of the theta – gamma coupling varies depending on the behavioural state. In particular, theta – gamma coupling supports memory encoding (Tort et al., 2009) and retrieval (Vivekananda et al., 2020). The theta-gamma coupling is also less prominent in patients with Alzheimer's disease or mild cognitive impairment, and serves as the best predictor for performance in a working memory task (Goodman et al., 2018).

Two types of hippocampal theta oscillation have been reported: type 1 (7–14 Hz) and type 2 (4–9 Hz). Theta 1 occurs during active states such as locomotion or exploration (Whishaw and Vanderwolf, 1973; Oddie and Bland, 1998; Buzsáki, 2002; Fuhrmann et al., 2015) and disappears under anesthesia (Kramis et al., 1975). Type 2 theta, on the contrary, is related to emotions and occurs in inactive states including REM sleep and anesthesia (Kramis et al., 1975; Bland, 1986; Sainsbury et al., 1987). Recently, both types of theta oscillations were reported in the human anterior and posterior hippocampus (Goyal et al., 2020), which are structurally analogous to the rodent ventral and dorsal hippocampus (Zhang and Jacobs, 2015). Both types of theta oscillation critically depend on the input from the medial septal nucleus (Mizumori et al., 1989; Vinogradova, 1995). The mechanism of hippocampal theta generation and the involvement of the distinct medial septal cell populations is discussed in detail in Chapter 3. The complexity of the hippocampal theta generation was highlighted in the recent study of López-Madrona et al. (2020), who identified three different current generators of the theta hippocampal rhythm in the dorsal hippocampus of a rat with dynamically changing interactions.

Another aspect of the hippocampal theta oscillation is the spatio-temporal dynamics of its spread. Recordings from both the rodent (Lubenov and Siapas, 2009) and human (Zhang and Jacobs, 2015) hippocampus revealed that the theta oscillation is a travelling wave. The amplitude of the theta oscillation recorded in the dorsal hippocampus is strongly modulated by locomotion (Kropff et al., 2021; McFarland et al., 1975). In the ventral hippocampus, type 2 oscillation was reported (Mikulovic et al., 2018) and the locomotion-dependent modulation of amplitude is only very weak (Patel et al., 2012). In agreement with the differential involvement of

the dorsal and ventral hippocampus in spatial navigation, the amplitude of the type 1 theta oscillation decreases along the dorso-ventral axis (Patel et al., 2012). Several mechanisms have been suggested how the theta oscillation becomes a travelling wave (Lubenov and Siapas, 2009; Ermentrout and Kleinfeld, 2001). First, the projections from the medial septum, the pacemaker of the hippocampal theta oscillations, are topographically organized with potentially different transmission delays (Witter and Amaral, 2004). Other proposed mechanisms involve the generation of a propagating wave within the hippocampus, or dependence on topographically organized projections from the entorhinal cortex (Lubenov and Siapas, 2009). In Chapter 4 we present a mathematical framework for studying the generation of periodic travelling waves in neural network models.

1.3 The medial septum

The medial septum, diagonal band of Broca (MSDB) is often referred to as a subcortical hub. It is located in the basal forebrain and receives connections from the hippocampus, the amygdala, the thalamus, the ventral tegmental area and other structures. It sends axons, among others, back to the hippocampus, amygdala, the hypothalamus and the ventral tegmental area (Swanson and Cowan, 1979; Müller and Remy, 2018; Swanson and Risold, 2000). The most important target of the MSDB is the hippocampal formation.

The MSDB consist of three main neuronal populations: cholinergic (Frotscher and Léránth, 1985), GABAergic (Kiss et al., 1990) and glutamatergic (Hajszan et al., 2004). All three subpopulations are reciprocally connected (Leao et al., 2015). The GABAergic population is considered as the main pacemaker of the hippocampal theta oscillation (Robinson et al., 2016; Hangya et al., 2009). The cholinergic neurons provide slow excitation to the septal network and are thought to play a modulatory role in the theta generation (Müller and Remy, 2018). The involvement of the different MSDB subpopulations in the theta generation is described in detail in Chapter 3. Moreover, optogenetic activation of the MSDB glutamatergic cells reliably initiates locomotion, independently of glutamatergic synaptic transmission (Fuhrmann et al., 2015). Hence, the MSDB provides consistent input to motor-generating areas, as well as to the hippocampus by two distinct pathways. We provide further evidence for the dissociation of the theta- and motor-generating circuit in Chapter 2.

The MSDB can be regarded as an interface between emotions and cognitive functions such as memory and navigation. Septal lesion leads to a severe impairment

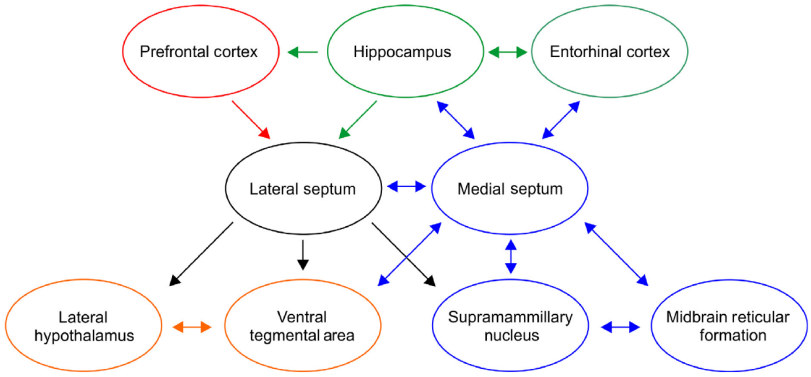

Figure 1.2: **Sketch of the MSDB functional connectivity.** The MSDB modulates the activity of several cortical and subcortical strutures via the theta oscillations and arousal (blue colour), and thereby is involved in their functions: spatial navigation and episodic memory (green), reward and navigation (orange) and divergent polyvalent signal processing (black), such as further processing of spatial position (Tingley and Buzsáki, 2018). The red colour indicates planning and cognitive behaviour. Reproduced from Tsanov (2018) with permission from John Wiley & Sons, Inc.

of memory (Winson, 1978; Vinogradova, 1995). As an essential structure for the theta-rhythm generation, the MSDB is indirecty involved in various functions that are modulated by the rhythm such as navigation, voluntary movement, anxienty or motivation (Section 1.2). Figure 1.2 adapted from (Tsanov, 2018) depicts how the MSDB modulates activity and function of other cortical and subcortical areas via the theta-rhythmic spiking. An interesting association between emotional states and spatial navigation has been made by Wells et al. (2013), who described differential effects of novelty and anxienty on the linear relationship between theta frequency and running speed. Apart from its involvement in the theta rhythm generation, the basal forebrain is the main source of acetylcholine in the brain and thereby modulates various functions, such as the circadian rhythms (Yamakawa et al., 2016), sleep states (Hasselmo and Giocomo, 2006), learning and memory (Hasselmo, 2006), attention (Hasselmo and McGaughy, 2004) or arousal (Everitt and Robbins, 1997).

The MSDB has also been investigated in the context of potential therapeutical manipulations. An improvement in memory performance was reported following a deep brain stimulation of the medial septum (Jeong et al., 2014). Electrical stimulation of the medial septum was also suggested as an effective therapy for temporal lobe

epilepsy by restoration of the hippocampal theta oscillation (Fisher, 2015). Furthermore, the medial septal electrical stimulation increases seizure threshold and improves cognitive abilities in epileptic rats (Izadi et al., 2019). Recently, a quick termination of an epileptic seizure was achieved by a closed-loop electrical stimulation of the medial septum (Takeuchi et al., 2020), where precise timing of stimulation determined by pre-stimulus internal rhythm was essential.

1.4 Mathematical and computational modelling of travelling waves

The theta oscillation spreads across the hippocampus as a periodic travelling wave (Lubenov and Siapas, 2009; Zhang and Jacobs, 2015, Section 1.2) that can be generated by a wealth of mechanisms, depending on different cellular and network properties. Computational models can provide mechanistic understanding of dynamic processes in the neural tissue, provided they are well constrained. Undoubtedly, the priority should always be to find sufficiently specific biological constraints both from the bottom-up and top-down perspective, that is by known cellular and network properties, as well as characteristics of the neural activity, respectively. However, in reality it is often not possible to fully constrain the model parameters, leading to a variety of possible dynamical states. At this point, mathematical analysis can provide the missing constrains from the top-down perspective.

Neural activity can be modelled at different levels of description in terms of both cellular dynamics and synaptic connections. The Hodgkin-Huxley neuron model is typically used as a detailed model of spike generation (Hodgkin and Huxley, 1952). When the phenomenon of interest relies on the network-level, rather than single-neuron mechanisms, more phenomenological single-cell models with simpler dynamics are suitable. Such models include the leaky-integrate-and-fire model with its several alternatives (Lapicque, 1907; Stein, 1967; Latham et al., 2000), the theta model (Ermentrout and Kopell, 1986) or the so called Izhikevich model (Izhikevich, 2003). Such networks enable large-scale simulations of cortical columns with realistic neural density (Potjans and Diesmann, 2014; Jordan et al., 2018). However, constraining parameters of such network simulations and investigating their dynamics typically requires large parameter scans that can be computationally costly and time consuming.

Neural mass models, on the other hand, allow for mathematical tractability at the expense of reduced biological detail. Here, individual cells are not modelled

explicitly, but as a continuum of points, so called mean-field, with average response properties (Wilson and Cowan, 1972a, 1973a; Amari, 1977; Amit and Brunel, 1997a; Brunel and Hakim, 1999; Brunel, 2000), for a review see (Deco et al., 2008). Travelling waves of spiking activity have been extensively studied in such models. However, even neural mass models might be difficult to analyze mathematically when certain biological phenomena are explicitly modelled. The best example of an important phenomenon that dramatically increases complexity of the model is the transmission delay. While the dynamical system generated by the system of equations describing the population dynamics without transmission delay resides in a finite dimensional state space, the addition of transmission delay moves it to an infinite-dimensional state space. Concerning linear stability analysis, this leads to transcendental characteristic equations with infinite number of solutions and increased complexity of possible dynamical states. Nevertheless, even in such case linear stability analysis can be applied (Veltz and Faugeras, 2011; Diekmann and Korvasová, 2016).

Constraining simulations of discrete spiking neural networks by mathematical analysis of continuous neural mass models requires a link between these two levels of description. Concretely, one has to know how to map parameters of one model to the other to be able to apply theoretically obtained results to defining parameters in the spiking network model. Such link has been provided for networks with both homogeneous connectivity (Ott and Antonsen, 2008; El Boustani and Destexhe, 2009; Buice et al., 2010; Schwalger et al., 2017; Schuecker et al., 2015), and distance-dependent connectivity (Kriener et al., 2014; Avitable and Wedgwood, 2017; Senk et al., 2020a). In relation to septal generation of the hippocampal theta oscillation, the mean-field description (Luke et al., 2013) of a network of theta neurons (named after the angular state variable of the model in Ermentrout and Kopell, 1986), or the equivalent quadratic leaky-integrate-and-fire neurons (Brunel and Latham, 2003), is of particular interest. These models are capable of producing theta-rhythmic bursting typically observed in a subpopulation of medial septal neurons (King et al., 1998; Borhegyi et al., 2004; Mamad et al., 2015; Kocsis et al., 2021). Recent results suggested that the theta rhythm is generated by a population of MSDB intrinsically rhythmic pacemakers that synchronize via the so called Huygens synchronization, similarly as clocks on a wall (Kocsis et al., 2021). Consequently, networks of pulse-coupled oscillators (Mirollo and Strogatz, 1990) that were already studied in the context of the hippocampal travelling waves (Ermentrout and Kleinfeld, 2001; Skinner et al., 2001) and were consistent with experimentally obtained results (Penn

et al., 2016; Goyal et al., 2020), could also be an appropriate model for the medial septal network.

1.5 The scope of the thesis

The aim of this thesis is to investigate the role of the medial septum, diagonal band of Broca in the generation of the hippocampal theta rhythm, and in initiation of locomotion. Furthermore, we developed a theoretical framework for studying the origin of oscillations and travelling waves in simulations of spiking neurons with distance-dependent connectivity. The main questions can be summarized as follows.

- **Can locomotion and hippocampal theta oscillation be triggered by continuous light stimulation of MSDB VGluT2 neurons? What is the response of MSDB neurons to the stimulation?**

  It has been previously shown that theta-periodic optical stimulation of the MSDB vesicular glutamate transporter type 2 (VGluT2) triggers locomotion and strong theta power in the hippocampal local field potential (Fuhrmann et al., 2015). In Chapter 2 we ask the question whether the theta-periodicity of the stimulus was necessary for both hippocampal theta and locomotion induction. Next, we study the response of the MSDB neurons to the optical stimulus under different pharmacological conditions. To further understand the dependence of the persistent firing on MSDB synaptic connections and external input, we repeat the same stimulation experiment in an acute MSDB slice preparation.

- **Can the medial septal network produce synchronous regular spiking in the theta frequency range independently of external input? What is the frequency-generating and synchronizing mechanism?**

  Despite decades of research, the origin of the hippocampal theta oscillation is still under debate (Buzsáki, 2019). The MSDB is seen as the pacemaker of the theta rhythm (Petsche et al., 1962, 1965; Robinson et al., 2016; Kocsis et al., 2021), but it still remains unclear whether it can synchronize the theta rhythm independently. Several successful attempts were made to induce the theta oscillation in a MSDB slice preparation, but in all cases specific receptors had to be activated (Wen et al., 2013; Garner et al., 2005; Lu et al., 2011). In Chapter 3, we analyze the spontaneous spiking activity in an acute MSDB slice preparation, in particular synchronization in the theta frequency range.

- **Can mean-field theory and linear stability analysis be used to understand the generation of periodic travelling waves in spiking neural networks?**

  Neural activity is modelled at different levels of description: from detailed biophysical simulations to differential equations describing the average population dynamics. These models provide an additional value when information obtained at one level of description can be transferred to the other level of description. In Chapter 4 we aim at bridging the gap between a spiking simulation of neurons with distance-dependent connectivity and a population neural field model. We define a mapping between parameters of the two models and use the obtained framework to investigate the generation of periodic travelling waves, so called wave trains, in spiking neural networks.

2 Persistent firing of medial septal glutamatergic neurons in response to optogenetic stimulation

* * *

This chapter is based on the publication (Korvasová et al., 2021). The author performed all data analysis, visualization, wrote the Results section and a part of the Methods section related to data analysis. Sanja Mikulovic took part in writing the Introduction and Discussion of the manuscript, the parts of the Methods section related to experimental procedures were written by Hiroshi Kaneko and Liudmila Sosulina. All authors of the manuscript participated in the review and editing. The project was supervised by Tom Tetzlaff, Sanja Mikulovic and Stefan Remy. Figures with captions were created by the author and already presented in (Korvasová et al., 2021).

* * *

Glutamatergic neurons in the medial septum and diagonal band of Broca (MSDB) are the most recently identified subpopulation of the MSDB (Hajszan et al., 2004). A growing body of evidence suggests their importance in modulating activity in the MSDB during locomotion and affecting the accompanying hippocampal theta rhythm (Manseau et al., 2005; Huh et al., 2010; Leao et al., 2015; Robinson et al., 2016; Fuhrmann et al., 2015; Zhang et al., 2018; Dannenberg et al., 2019). In particular, the activity of MSDB glutamatergic neurons (VGluT2 - vesicular glutamate transporter 2) is increased during locomotion and correlates with speed (Fuhrmann et al., 2015). Moreover, both locomotion and hippocampal theta can be induced by

theta-rhythmic optogenetic stimulation of MSDB VGluT2 neurons, outlasting the stimulus by several seconds (Fuhrmann et al., 2015; Justus et al., 2017). It remains unknown whether the rhythmicity of the stimulation is necessary for locomotion and theta induction, or whether the VGluT2 neurons only contribute tonic excitation to the local MSDB network and continuous stimulation would be sufficient. Furthermore, the mechanism leading to the persistence of the induced activity after the stimulus offset is not known, as is the relation between the persistent firing of MSDB VGluT2 neurons, persistent locomotion and persistent hippocampal theta oscillation.

A sustained increase in spiking activity, referred to as persistent firing, has been observed in several brain areas of primates (Gottlieb et al., 1989; Supèr et al., 2001; Zhou and Fuster, 1996), humans (Todd and Marois, 2004; Schluppeck et al., 2006; Srimal and Curtis, 2008) and more recently rodents (Pastalkova et al., 2008; Yoshida and Hasselmo, 2009; MacDonald et al., 2011; Harvey et al., 2012). From the behavioural point of view, persistent firing has been traditionally associated with working memory (Fuster, 1973; Kubota et al., 1974; Zylberberg and Strowbridge, 2017), but later a more general function was suggested such as motor control (Kiehn and Eken, 1998), decision making (Seo et al., 2007) or reinforcement learning (Seo et al., 2009). The existence of persistent firing in the MSDB has not yet been established and is of interest due to involvement of the MSDB in these behaviours (Turnbull et al., 1994; McNaughton et al., 2006; Shirvalkar et al., 2010; Lipponen et al., 2012; Fuhrmann et al., 2015).

In this study, we demonstrate that a one-second continuous light pulse reliably triggers locomotion and hippocampal theta oscillation, while the hippocampal theta oscillation is not causally related to locomotion. On the level of MSDB, we observed robust persistent firing both in vivo and in vitro that does not depend on synaptic connectivity within the MSDB. Hence, we hypothesize that the MSDB persistent firing is generated by single-cell mechanisms of MSDB VGluT2 neurons.

2.1 Optical stimulation of MSDB VGluT2 neurons induced locomotion, hippocampal theta oscillation and persistent firing of MSDB neurons

Mice were positioned on a spherical or linear treadmill and head-fixed (Figure 2.1A). The locomotion speed, CA1-hippocampal local-field potential (LFP) and MSDB multi-unit activity were simultaneously monitored (Figure 2.1B). To test whether non-rhythmic optogenetic stimulation of MSDB VGluT2 neurons triggers locomotion and CA1 theta oscillation, MSDB VGluT2 neurons were stimulated by 1s continuous light pulses (Figure 2.1C).

After the onset of the stimulation, we observed a reliable increase of MSDB spiking activity, CA1 LFP power in the theta-frequency range ($7 - 12$ Hz) and an onset of locomotion (Figure 2.1D, E, Figure 2.6). Moreover, all three effects were still present after the stimulus offset and were considered persistent if they lasted for more than 1s after the stimulus offset (persistent activity was defined as significantly higher firing rate in the interval $(2, 4)$ seconds after the stimulus onset, compared to the baseline computed from 2 seconds before to the stimulus onset). However, the duration of the persistent activity differed between the different modalities. Locomotion typically started before the onset of CA1 theta oscillation and lasted for less than 5 seconds (mean 4.4 s, standard deviation 2.9 s). The duration of the MSDB persistent spiking activity was much longer, outlasting the 20s recording. This dataset therefore cannot answer the question of when and how the MSDB persistent activity stops. To assess the relevance of MSDB elevated firing in physiological conditions, we also monitored the level of MSDB spiking activity during voluntary running and showed a significant increase compared to baseline, as predicted by the stimulation experiment (Figure 2.1F).

To get some understanding of the mechanism underlying the persistent activity, we tested whether it relies on synaptic connectivity by applying a synaptic blocker cocktail (Figure 2.2A) that inactivates glutamatergic, GABAergic and cholinergic connections in the MSDB (Figure 2.2B). Although this experiment cannot explain the mechanism in detail, it can uncover whether the activation of MSDB non-glutamatergic neurons is a necessary conditions for locomotion or the hippocampal theta oscillation. Our results suggested that activating MSDB non-glutamatergic neurons is necessary neither for locomotion initiation (Figure 2.2C-E upper panel),

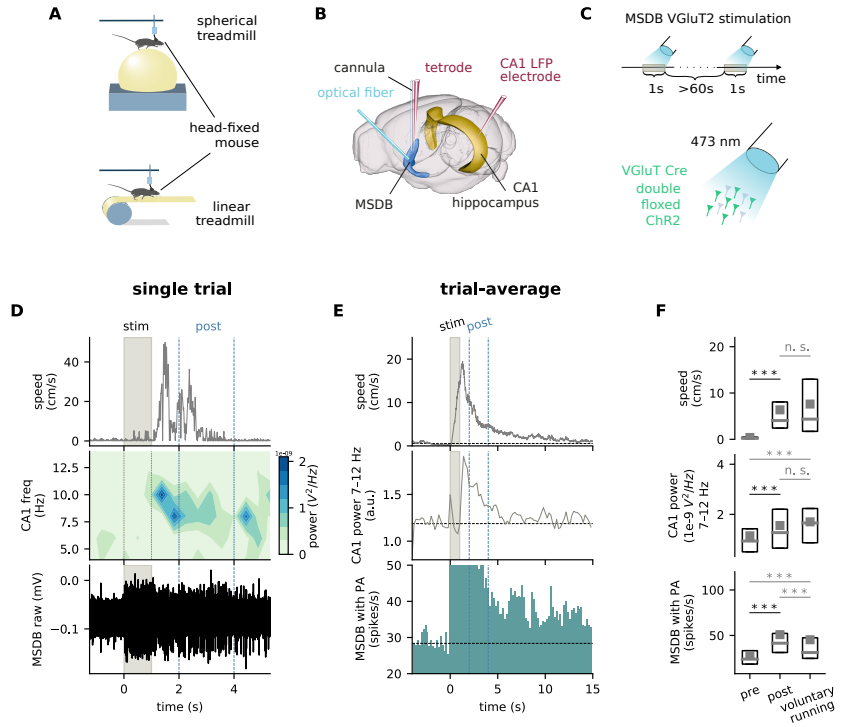

Figure 2.1: **Brief continuous MSDB VGluT2 stimulation triggers persistent activity in the MSDB, locomotion and hippocampal theta.** **A.** Experimental setup: a head-fixed mouse running on a spherical or linear treadmill. Produced using the SciDraw database (Branco and Costa, 2020). **B.** LFP electrode in CA1, optical fiber and tetrode in the MSDB. Produced using The Scalable Brain Atlas (Bezgin et al., 2009), based on The Allen Reference Atlas (Lein et al., 2007). **C.** Continuous 1s light stimulation of MSDB VGluT2 neurons. **D.** Representative recordings of speed, CA1 LFP with the corresponding spectrogram and MSDB extracellular potential. The grey vertical band marks the continuous light stimulus (0–1 s), the dotted lines mark the time interval used to analyze post-stimulus activity (2–4 s). **E.** Trial-averaged speed (upper panel), CA1 LFP power in the frequency range 7–12 Hz (middle panel) and the average histogram of multi-unit spiking activity of channels with persistent activity (PA) (lower panel). Average across all recording sessions with 4 mice. For significance of a single-channel positive response to one stimulus repetition, $p < 0.05$ from the one-sided Mann-Whitney U-test applied on inter-spike intervals was required. **F.** Distribution of time-averaged speed (upper panel), CA1 LFP power in the range 7–12 Hz (middle panel) and mean firing rate of channels with persistent activity (lower panel) for time periods 2 seconds before the stimulus when the mouse was at rest, in the interval 2–4 seconds and during voluntary running. The bar denotes the median, the square the mean and the box spans between the first and the third quartile. Additional information is provided in Section 2.6.2. Reproduced from (Korvasová et al., 2021).

nor for the persistent activity in the MSDB (Figure 2.2C-E lower panel, Figure 2.7). However, the CA1 theta oscillation was abolished by the synaptic blockade (Figure 2.2C-E middle panel). These results also imply that the hippocampal theta oscillation is not necessary for locomotion. The locomotion duration was similar as without blocked synaptic transmission in the MSDB (mean 3.7 s, standard deviation 2.9 s). The persistent activity again exceeded the recording and therefore could not be quantified. We did not observe any systematic difference between trials recorded on the spherical and linear treadmill (Figure 2.8). Finally, after blocking MSDB glutamatergic synapses only, we observed reliable locomotion initiation, as well as MSDB persistent activity (Figure 2.9).

2.2 Persistent activity is presumably a single-cell effect

The in vivo experiment described in Section 2.1 did not rule out the possibility that the persistent activity is driven by feedback from a different brain area. To test whether MSDB can generate persistent activity independently, we repeated the experiment with the same stimulation paradigm in an acute MSDB slice preparation (Figure 2.3A) and recorded the extracellular potential with a 6×10 microelectrode array (MEA) (Figure 2.3B). As in the previous section, a 1s continuous light pulse was used to activate VGluT2 neurons (Figure 2.3C). Subsequently, we also repeated the experiment with blocked synaptic transmission.

We observed robust persistent activity for a few seconds after the 1s continuous optical stimulus was turned off (Figure 2.3D). Persistent activity was detected in roughly one fifth of MSDB cells (Figure 2.3E) and the median firing rate of persistently firing cells increased increased from the baseline 5 spikes per second to 12 spikes per second (Figure 2.3F). The increase of firing rate above baseline was observable for at least 20s (Figure 2.3G), in line with the activity observed in vivo. The coefficient of variation of the inter-spike intervals was higher after the stimulus compared to baseline (Figure 2.3H). This effect might be caused by the activation of bursting neurons with possibly regularly spaced bursts, and is therefore not necessarily in contradiction with the elevated hippocampal theta power. In terms of reliability of responses, about one fifth of neurons showed persistent firing after all repetitions of the stimulus (Figure 2.3I).

Further, we blocked synaptic transmission in the MSDB (Figure 2.4A, B) to test the effect of the network on persistent activity. The elevated firing, persisting after

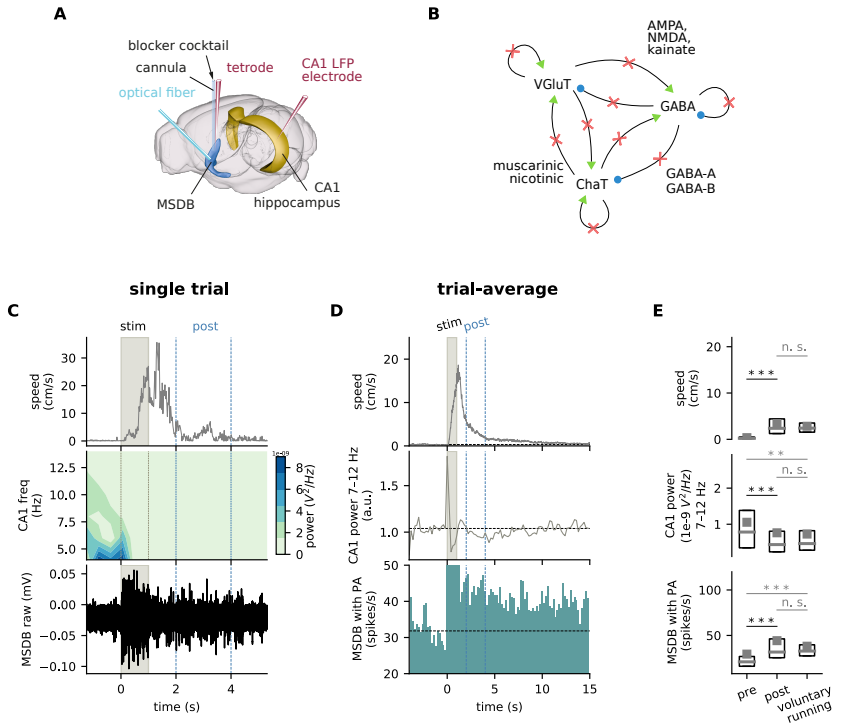

Figure 2.2: **Blocking intraseptal synaptic connectivity abolished CA1 theta, but not locomotion and MSDB persistent activity.** **A.** Blocker cocktail was applied through a cannula in the MSDB. Produced using The Scalable Brain Atlas (Bezgin et al., 2009), based on The Allen Reference Atlas (Lein et al., 2007). **B.** Types of synapses blocked by the blocker cocktail. Excitatory synapses are marked by green arrows and inhibitory by blue circles. **C.** Representative recordings of speed, CA1 LFP with the corresponding spectrogram and MSDB extracellular potential. The grey vertical band marks the continuous light stimulus (0–1 s), the dotted lines mark the time interval used to analyze post-stimulus activity (2–4 s). Same mouse as in Figure 2.1D. **D.** Trial-averaged speed (upper panel), CA1 LFP power in the frequency range 7–12 Hz (middle panel) and the average histogram of multi-unit spiking activity of channels with persistent activity (PA) (lower panel). Average across all recording sessions with 3 mice. For significance of a single-channel positive response to one stimulus repetition, $p < 0.05$ from the one-sided Mann-Whitney U-test applied on inter-spike intervals was required. **E.** Distribution of time-averaged speed (upper panel), CA1 LFP power in the range 7–12 Hz (middle panel) and mean firing rate of channels with persistent activity (lower panel) for time periods 2 seconds before the stimulus when the mouse was at rest, in the interval 2–4 seconds and during voluntary running. The bar denotes the median, the square the mean and the box spans between the first and the third quartile. Additional information is provided in Section 2.6.2. Reproduced from (Korvasová et al., 2021).

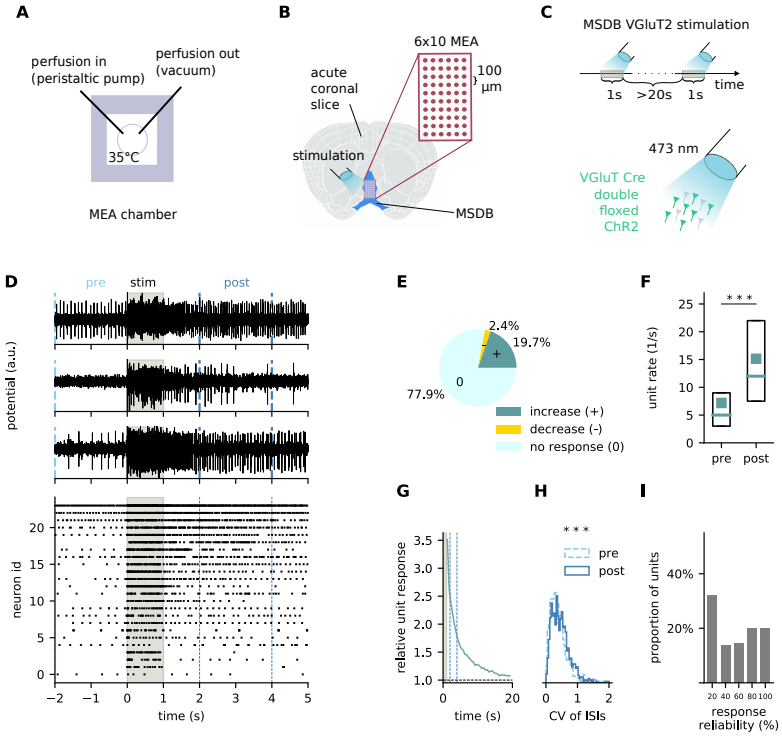

Figure 2.3: **Stimulus-induced persistent activity is generated locally in the MS.** **A.** Experimental setup: oxygenation chamber. **B.** An acute coronal slice was positioned on a 6x10 MEA with electrode distance 100 μm. Produced using The Scalable Brain Atlas (Bezgin et al., 2009), based on the Allen Reference Atlas (Lein et al., 2007). **C.** Continuous 1s light stimulation of MSDB VGluT2 neurons. **D.** Representative traces of the extracellular potential in the acute MSDB slice preparation. The grey vertical bands mark the continuous light stimulus (upper panel). Extracted single-unit activity for one representative slice (lower panel). **E.** Percentages of units with significant increase (dark green), significant decrease (yellow) and no significant change (light green) of firing rate in response to the stimulus. For significance of a single-unit response to one stimulus repetition, $p < 0.05$ from the one-sided Mann-Whitney U-test applied on pre- and post-stimulus inter-spike intervals was required (pre: $(-2, 0)$ s, post: $(2, 4)$ s). **F.** Distribution of firing rates before and after the stimulus (pre: $(-2, 0)$ s, post: $(2, 4)$ s). Only units with persistent activity were considered. Statistical significance of the difference between pooled mean firing rates pre and post: $p = 1.9{\cdot}10^{-40}$ (237 trials, first stimulus). **G.** Trial-averaged time course of single-unit spiking activity. Single stimulus response per unit. **H.** Distribution of coefficients of variation (CV) or inter-spike intervals (ISIs), pre stimulus ($(-2, 0)$ s, blue) and post stimulus ($(2, 4)$ s, red). Single stimulus response per unit. **I.** Percentages of units that respond with given reliability across five stimulus repetitions. (Two-sided Wilcoxon's signed-rank test, 19 brain slices.) Reproduced from (Korvasová et al., 2021).

the stimulus offset, was still reliably observed in roughly $\sim 30\%$ of cells, similarly as without blocked synapses (Figure 2.4C, D). However, the firing rate reached lower values with 9 spikes per seconds after the stimulus compared to the baseline median 6 spikes per second (Figure 2.4E), as non-VGluT neurons could not be recruited by fast glutamatergic excitation in the blocked scenario. The duration of the persistent activity, on the other hand, was not affected by blocking synaptic transmission (Figure 2.4F). The coefficient of variation showed more similar values before and after the stimulus, compared to the intact slice (Figure 2.4G). The reliability of inducing persistent activity by the stimulus was lower in the blocked network, with about half of units responding to only one from five repetitions (Figure 2.4H).

2.3 MSDB network amplifies persistent activity

In the previous two sections we showed that persistent activity in the MSDB occurs even with blocked synaptic transmission. However, the network may still have a quantitative effect on the activity such as increase the firing rates or prolong the duration of the persistent activity. We observed qualitatively different relations between measures with and without synaptic blockers when applied to the in vivo and in vitro recordings.

In vivo, the firing rate during the stimulus was higher in the blocked condition and did not significantly differ after the stimulus (Figure 2.5A). Also the durations of the persistent activity with and without synaptic blockers were comparable (Figure 2.5B). However, persistent activity was detected in a larger proportion of channels in the intact network as compared to blocked. As mentioned earlier, this effect may be caused by secondary synaptic activation of non-VGluT2 type neurons in the MSDB by the directly stimulated VGluT2 cells. Some cells stopped firing after the stimulus and resumed firing only after several seconds, as in the example in Figure 2.7. This phenomenon was observed more frequently in the blocked condition than in the intact (Figure 2.5C). In both cases, the channels with high levels of persistent activity also exhibited high levels of activity during the stimulus (Figure 2.5D), indicating that persistently firing cells are presumably mostly VGluT2 cells.

In the in vitro recordings, blocking synaptic transmission decreased the firing rate both during and after the stimulus (Figure 2.5E), but the duration of persistent activity did not seem to be strongly affected (Figure 2.5F). Similarly as in vivo, we observed persistent activity in a larger proportion of channels in the intact slice and stimulus-induced suppression of activity in a larger proportion of channels in

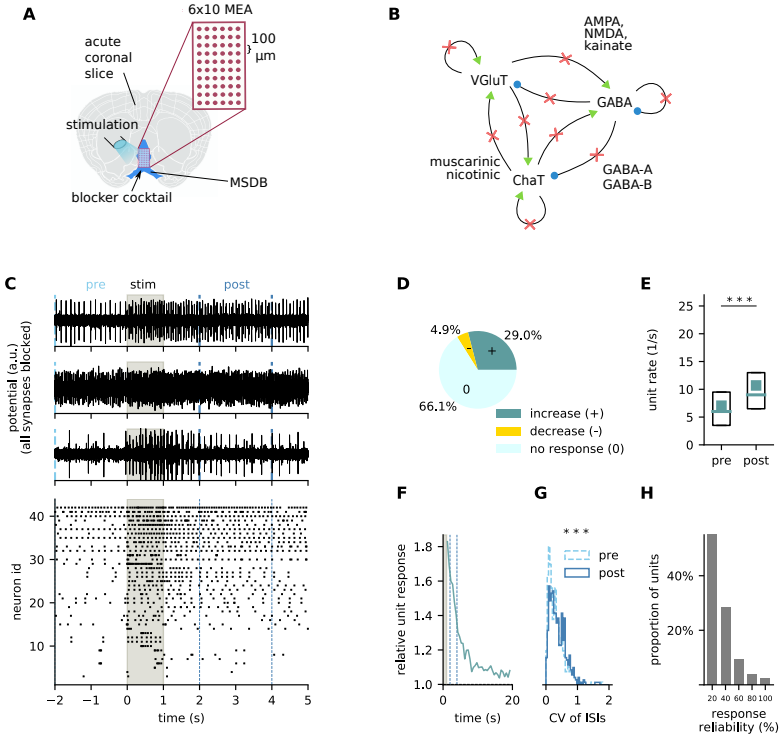

Figure 2.4: **Persistent activity is generated by intrinsic dynamics of MSDB VGluT2 neurons** **A.** Application of the blocker cocktail to the MSDB. Produced using The Scalable Brain Atlas (Bezgin et al., 2009), based on The Allen Reference Atlas (Lein et al., 2007). **B.** Types of synapses blocked by the blocker cocktail. Excitatory synapses are marked by green arrows and inhibitory by blue circles. **C.** Representative traces of the extracellular potential in an acute MSDB slice preparation. The grey vertical bands mark the continuous light stimulus (upper panel). Extracted single-unit activity for one representative slice (lower panel). **D.** Percentages of units with significant increase (dark green), significant decrease (yellow) and no significant change (light green) of firing rate in response to the stimulus. For significance of a single-unit response to one stimulus repetition, $p < 0.05$ from the one-sided Mann-Whitney U-test applied on pre- and post-stimulus inter-spike intervals was required (pre: $(-2, 0)$ s, post: $(2, 4)$ s). **E.** Distribution of firing rates before and after the stimulus (pre: $(-2, 0)$ s, post: $(2, 4)$ s). Only units with persistent activity were considered. Statistical significance of the difference between pooled mean firing rates pre and post: $p = 2.3 \cdot 10^{-31}$ (185 trials). **F.** Trial-averaged time course of single-unit spiking activity. Single stimulus response per unit. **G.** Distribution of coefficients of variation (CV) or inter-spike intervals (ISIs), pre stimulus ($(-2, 0)$ s, blue) and post stimulus ($(2, 4)$ s, red). Single stimulus response per unit. **H.** Percentages of units that respond with given reliability across five stimulus repetitions. (Two-sided Wilcoxon's signed-rank test, 11 brain slices.) Reproduced from (Korvasová et al., 2021).

the blocked network (Figure 2.5G). The fact that neurons with high firing rates post stimulus also show high firing rates during the stimulus (Figure 2.5H, Figure 2.11B) supports the hypothesis that the directly stimulated VGluT2 neurons are the main generators of the persistent activity.

2.4 Discussion

In this chapter we demonstrated that a 1 second continuous light stimulation of MSDB VGluTs neurons initiates locomotion, hippocampal theta oscillation and elevated firing rate in the MSDB, all persisting after the stimulus offset. Unlike the theta oscillation, the locomotion initiation was not affected by blocking synaptic transmission in the MSDB (Figure 2.2 D-F). In line with previous findings (Koenig et al., 2011; Brandon et al., 2011; Pastalkova et al., 2008; Robinson et al., 2016), our results suggest that synaptic connectivity within the MSDB is necessary for the generation of the hippocampal theta rhythm. Moreover, the observed MSDB persistent firing appears to be cell-intrinsic and potentially driving locomotion.

Our results support the view that MSDB activity passed by the direct septo-hippocampal glutamatergic projections alone cannot induce hippocampal theta oscillation (Robinson et al., 2016). However, the hippocampal theta might be modulated by the direct MSDB VGluT2 input as suggested by Fuhrmann et al. (2015). Kocsis et al. (2021) recently showed that the hippocamapal theta oscillation is driven by parvalbumin-positive neurons activated by tonic excitation. The elevated firing rate and persistent activity that we observed in the MSDB might serve as such tonic excitation for the MSDB interneurons.

Previous studies reported that the hippocampal theta oscillation appears together with the locomotion onset (Teitelbaum et al., 1975) or a few hundred milliseconds before (Green and Arduini, 1954; Vanderwolf, 1969; Whishaw and Vanderwolf, 1973; Bland et al., 2006; Fuhrmann et al., 2015). In the current study we observed first the onset of locomotion and only subsequently the increase in hippocampal theta power. A potential reason for the delayed onset of the hippocampal theta oscillation could be the high firing rate of MSDB cells during the continuous light stimulation (Figure 2.5A).

Despite the fact that the hippocampal theta oscillation is not necessary for locomotion initiation and maintenance, the effect on other functions necessary for ethologically relevant movement such as navigation or movement planning remains unclear. It was shown that the loss of theta oscillation induced by MSDB inhibition

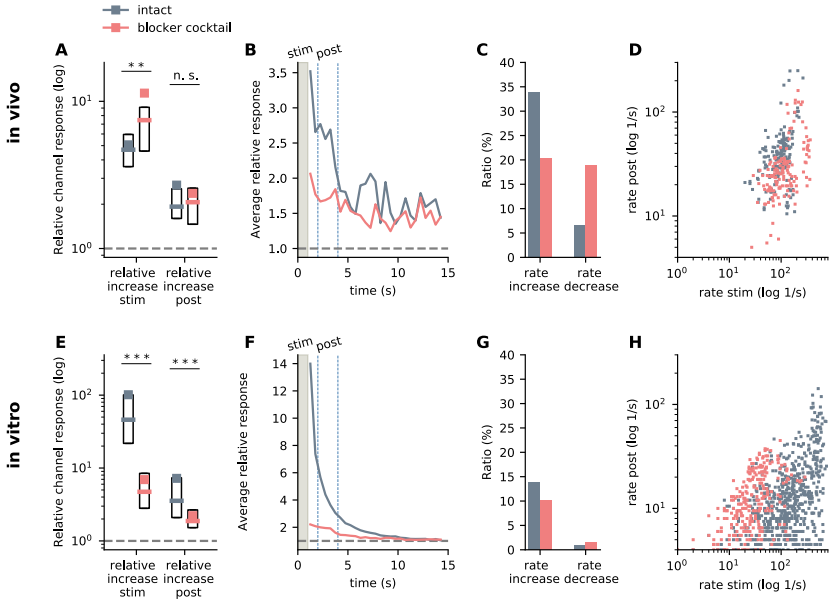

Figure 2.5: **MSDB network increased the strength of firing response.** **A.** Relative rate response during and after the stimulus in the intact network (blue-grey) and with the blocker cocktail (pink). The relative rate response during (resp. after) the stimulus was calculated as the mean firing rate during the stimulus (resp. in the interval $(2, 4)$ s) divided by the baseline calculated over 2 seconds prior to the stimulus in each channel. Numbers of trials: 56 in vivo intact, 33 in vivo blocker cocktail. Statistical significance: rate increase during the stimulus $p = 0.031$, post stimulus $p = 0.11$. The bar denotes the median, the square the mean and the box spans between the first and the third quartile. Statistical significance was calculated using the two-sided Mann-Whitney U-test. **B.** Trial-averaged instantaneous firing rate of the MSDB population divided by the pre-stimulus baseline. **C.** Percentages of channels where a significant increase, resp. decrease was observed compared to pre-stimulus baseline. Significance of rate increase or decrease in each channel was calculated using the one-sided Mann-Whitney U-test. **D.** Relationship between the multi-unit firing rate during (horizontal axis) and in the interval $(2, 4)$ s (vertical axis). **E.** As A in the acute MSDB slice preparation. Numbers of trials: 261 from 19 intact slices, 83 from 11 slices with blocker cocktail. Statistical significance: rate increase during the stimulus $p = 4 \cdot 10^{-30}$, post stimulus $p = 6 \cdot 10^{-12}$. **E-H.** As B,C in the acute MSDB slice preparation. Reproduced from (Korvasová et al., 2021).

impairs spatial memory (Winson, 1978), accurate navigation (Bolding et al., 2020), hippocampal firing fields (Pastalkova et al., 2008; Wang et al., 2015) and grid-cell periodicity (Brandon et al., 2011; Koenig et al., 2011).

Persistent activity in different parts of the brain was previously linked to working memory (Barak and Tsodyks, 2014), but also other functions such as reinforcement learning, decision making or defensive behaviour (Seo et al., 2007; Barraclough et al., 2004; Seo et al., 2009; Histed et al., 2009; Kennedy et al., 2020). The persistent activity that we observed may also be involved in these functions, as the MSDB takes part in behaviours such as working memory (Turnbull et al., 1994; McNaughton et al., 2006; Lipponen et al., 2012; Roland et al., 2014; Li et al., 2020) or decision making (Collins and Saunders, 2019). A likely scenario is that the MSDB VGluT2 neurons send direct projections to other brain areas that further project to motor-generating areas, as we observed reliable locomotion initiation even with blocked synaptic transmission in the MSDB (Figure 2.2). However, the functional relevance of the MSDB persistent firing still remains unknown.

Another open question is the mechanism of generation of the observed persistent firing in the MSDB, possibly involving both single-cell biophysical properties, as well as network effects. Persistent firing was previously observed with blocked synaptic transmission, pointing at intrinsic cellular mechanisms (Fransén et al., 2006; Pressler and Strowbridge, 2006; Navaroli et al., 2012; Jochems and Yoshida, 2015; Knauer et al., 2013). However, in other cases the synaptic circuit was necessary for persistent activity (Inagaki et al., 2019; Hart and Huk, 2020) and network-generated persistent firing was also successfully simulated in computational models based on attractor networks (Amit and Brunel, 1997b; Barak and Tsodyks, 2007; Nachstedt and Tetzlaff, 2017; Compte, 2006; Zylberberg and Strowbridge, 2017). In our experiments we observed robust persistent firing even after the application of synaptic blockers, supporting the hypothesis of intrinsic generation. The persistent firing was, however, stronger in the intact network, indicating that the network properties may also have a modulatory effect. Moreover, we cannot fully exclude the involvement of gap junctions and metabotropic glutamate receptors in the generation of MSDB persistent firing, as those were not blocked by the applied blocker cocktail. Further experiments are necessary to answer these questions.

2.5 Methods

2.5.1 Experimental procedure – in vivo recordings

2.5.2 Transgenic mice

Adult female VGluT2-cre mice Slc17a6$^{tm2(cre)Lowl}/J$, (The Jackson Laboratory, Bar Harbor, ME USA) were group-housed with 12-hour dark and light cycle and kept single-housed after the chronic surgery with ab libitum water and food. Experiments were performed during the light phase of the cycle. All experimental procedures were approved by the authorities of North Rhine-Westphalia and carried out in accordance with DZNE regulations in agreement with European Committees Council Directive.

2.5.3 Virus injection and surgical procedures

For the stereotactic injection of adeno-associated virus (AAV), the mice were anesthetized and head-fixed on a stereotactic frame. A craniotomy was drilled above the medial septum (+1.0 mm anterior-posterior and +0.7 mm lateral, relative to bregma, stereotactic coordinates from Franklin and Paxinos 2008). Channelrhodopsin-virus (pAAV2.1-EF1a-double floxed ChR2-EYFP-WPR (H134R), 1 μl) was then injected into both loci of the medial septum (−4.6 mm and −4.2 mm ventral, relative to bregma, with 10° laterally) through the craniotomy at 0.1 μl/min. The tetrode was placed 7 weeks after AAV injection. A fiber-optic cannula (OFC_400/430 0.37_5mm_SM3(P)_FLT, Doric Lenses, Quebec, Canada) was implanted 38° ventrally and 10° laterally, in the depth of 5.5 mm. Monopolar field potential electrode was placed into the CA1 stratum radiatum (−2.0 mm anterior-posterior, −2.0 mm lateral and −1.6 mm ventral, relative to bregma). For the tetrode recording, a craniotomy of 1.0 mm drilled on the right hemisphere (+1.0 mm anterior-posterior and +0.7 mm lateral from bregma). For the head-fixation during the recording, a metal-bar (Luigs-Neumann, Ratingen, Germany) was placed on the skull. Recovery time for the animals was 2 weeks.

2.5.3.1 Recording

Two types of treadmills were used for the recordings. First, a styrofoam spherical treadmill of diameter 20 cm, only rotating in one direction. Second, a linear treadmill of length 200 cm and width: 7 cm with virtual reality environment. Mice were head-fixed on the treadmill and let to run, while the running speed was detected by an optical computer mouse. Single/double shank tetrode ($0.5 - 0.8$ MΩ, Thomas

RECORDING GmbH, Gießen, Germany) was glued to a 34G cannula and placed to the MSDB in (depth $3400 - 4300$ μm, angle of 10° laterally). Multi-unit activity was recorded and filtered with $500 - 2000$ Hz bandpass filter using a 16 channels extracellular amplifier (EXT-16DX, npi, Tamm, Germany). Local-field potential was extracted using a $3 - 700$ Hz bandpass filter and recorded by an extracellular amplifier (EXT-02F/2, npi, Tamm, Germany). All signals were sampled at 25 kHz using an ITC-18 interface (HEKA Elektronik, Lambrecht, Germany) and recorded in Igor Pro 6.3 (WaveMetrics, Portland, USA). Light stimulation was performed using a 488 nm diode laser (Excelsior-488C-200-CDRH, Spectra-Physics, Santa Clara, USA). For synaptic blocker application, a UltraMicroPump with Hamilton syringe (Word Precision Instruments, Berlin, Germany) via the 34G cannula was used.

2.5.4 Experimental procedure – in vitro recordings

2.5.4.1 Slice preparation

Acute MSDB sliced of 400 μm thickness were cut as described in (Fuhrmann et al., 2015). Slices were then transferred to an interface chamber (Warner Instruments, Hamden, USA) with ACSF (Maier et al., 2009) for recovery (mM): 119 NaCl, 2.5 KCl, 2.5 $CaCl_2$, 1.0 NaH_2PO_4, 26 $NaHCO_3$, 1.3 $MgCl_2$, 10 glucose, oxygenated with 95% O_2 and 5% CO_2 and kept inside on a lens cleaning tissue (Grade 105, Whatman, Maidenstone, England) that ensures optimal oxygenation thanks to the flow of ACSF (35°C) for at least 3 hours.

2.5.4.2 Recording

Extracellular potential was recorded from the MSDB with a microelectrode array (MEA), MEA2100-System (Multi Channel Systems, Reutlingen, Germany, RRID:SCR_014809) on 60pMEA100/30iR-Ti MEAs with round titanium nitride (TiN) electrodes, for details see (Sosulina et al., 2021). The MS slices was placed onto a 6×10 grid of electrodes with 30 μm diameter and 100 μm distances. The temperature of the ACSF was maintained at 35°C using a heatable perfusion cannula PH01 with a TC01 controlling unit (Multi Channel Systems, Reutlingen, Germany). The placement of the slice was stabilized by a constant negative pressure of $25 - 30$ mBar. Signals were recorded using the MC_Rack (V 4.5.16.0, Multi Channel Systems, Reutlingen, Germany) at 25 kHz sampling rate with the MEA2100-lite-Interface Board.

MSDB VGluT2 neurons were stimulated with a light fiber coupled 473 nm diode laser (LuxX473-80, Omicron-Laserage) with the tip placed $\leq$ 5mm from the slice. Continuous stimulation with 1s duration was repeated 5 times in each recording. In some trials the recordings was then repeated after the application of synaptic blockers: glutamatergic blockers NBQX (10 μM) and DAP5 (50 μM), subsequently glutamatergic blockers together with GABA-ergic blockers SR-95531 (10 μM), CGP52432 (1 μM) and cholinergic blockers Atropin (10 μM), MLA (200nM).

2.5.5 Data analysis

For analysis, 19 slices without any synaptic blocker were used, 11 with NBQX, D-AP5 and 11 slices with the blocker cocktail.

2.5.5.1 Software implementation

Data analysis was performed using custom-written scripts in Python v3.6.10, all are available online: `https://gin.g-node.org/kkorvasova/medial_septum_persistent_activity`. In particular, the following packages were used: Numpy v1.19.2, Scipy v1.5.2, Neo v0.7.1, Elephant v0.6.2 and Matplotlib v3.3.2. Single units were isolated from extracellular potentials using Mountainsort v3 (Barnett et al., 2016).

2.5.5.2 Speed calculation

The position was first differentiated to obtain speed, then down-sampled to 1 ms (0.2 ms in Figures 2.1F, 2.2E, 2.9E and 2.8) and low-pass filtered at 20 Hz using the Butterworth filter of order 5. Only recordings where the average speed of the mouse within 3s prior to the stimulus onset did not exceed 3 cm/s were considered. For testing the duration of movement, we considered intervals of minimal length 1s where the speed of the mouse did not drop below 3 cm/s for more than 1 s.

2.5.5.3 Power spectrum analysis

Fourier transform with frequency resolution 2 Hz and 62.5 ms overlap of 500 ms time intervals was used to compute all spectrograms. To obtain a higher temporal resolution while keeping the frequency resolution of the spectrograms, the average power in the theta frequency range was calculated as an average of wavelets centered around frequencies $7, 7.5, 8, \ldots, 12$ Hz from a downsampled signal to 5000 Hz.

2.5.5.4 Statistical tests

The two-sided Wilcoxon's signed-rand test was used in cases where respective pairs of tested quantities could be identified (e.g. pre- and post-stimulus value of the mean firing rate). The two-sided Mann-Whitney U-test was used in other cases.

2.5.5.5 Analysis of MSDB spiking activity

Single-unit activity was extracted from the extracellular potentials using Mountainsort v3 (Barnett et al., 2016) with clip-size corresponding to a 2ms window, isolation threshold for curation 0.85, noise overlap 0.03 and threshold 7. For multi-unit activity extraction, the signal was band-pass filtered between 300 Hz and 3000 Hz using the Butterworth filter of order 5. Spike times were defined at waveform peaks and extracted using Elephant v0.6.2 by thresholding with the threshold set to 3, resp. 4.5 times the standard deviation of the band-pass filtered signal in vivo, resp. in vitro. Instantaneous firing rates were computed as histograms of spiking activity with bin size 200 ms. Single units with less than 10 spikes during the whole recording were not considered for analysis.

Persistent activity was defined as significantly (Wilcoxon's signed-rank test) increased firing rate 1–3 s after the stimulus offset (i.e. 2–4 s after the stimulus onset) relative to baseline 2 s before the stimulus onset. The first second after the stimulus offset was cut out for testing the persistence of elevated firing rate, because some units showed extreme values of instantaneous firing rate in a short time period after the stimulus offset that would distort the interpretation of mean firing rate after the stimulus offset and create false positives. The mean firing rate pre- and post-stimulus was calculated as the average firing rate over the respective intervals $(-2, 0)$s and $(2, 4)$s relatively to the stimulus onset. In Figures 2.1, 2.2, 2.9, only one channel per trial was considered and the minimum number of channels available in every trial. In Figures 2.3F, 2.4E and 2.10E only the first stimulus realization was analyzed because the firing rate before the stimulus in subsequent repetitions still seemed to be elevated from the previous stimulation. The relative firing rate response during (resp. before) the stimulus in Figure 2.5 was calculated as the mean firing rate during the stimulus (resp. in the interval $1 - 3$ seconds after the stimulus offset) normalized by the mean firing rate 2 seconds prior to the stimulus.

2.6 Supplementary materials

2.6.1 Supplementary figures

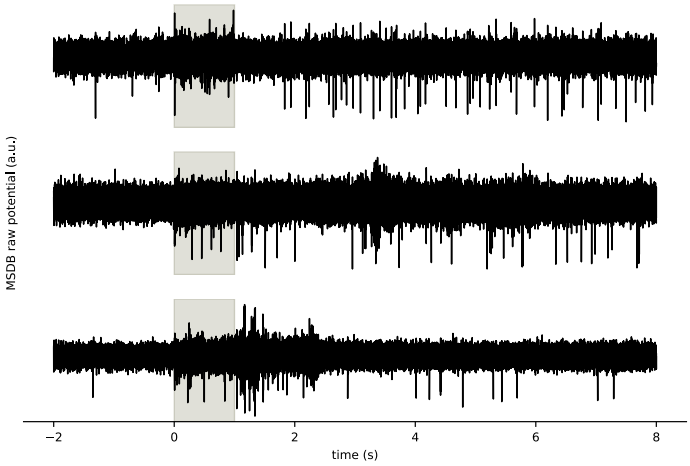

Figure 2.6: **Examples of potential traces in vivo.** Representative traces of raw potentials from the MSDB in vivo. Stimulus period is indicated with the grey region. Reproduced from (Korvasová et al., 2021).

2.6.2 Additional information to figures

This section contains additional information to figures reproduced from figure captions in (Korvasová et al., 2021).

Figure 2.1 All recordings of 4 mice were used, for firing rates only one channel per mouse was considered. Numbers of trials: 165 trials with one stimulus realization, out of them 122 show persistent activity, 121 trials with voluntary running, out of them 80 show persistent activity. Statistical significance: pre- vs post-stimulus speed $p = 2.6 \cdot 10^{-28}$, post-stimulus vs voluntary running $p = 0.94$, LFP power pre vs post $3 \cdot 10^{-6}$, post-stimulus vs voluntary running $p = 0.07$, pre-stimulus vs voluntary running $p = 1.4 \cdot 10^{-7}$, PA pre vs post $p = 9 \cdot 10^{-22}$, post-stimulus vs

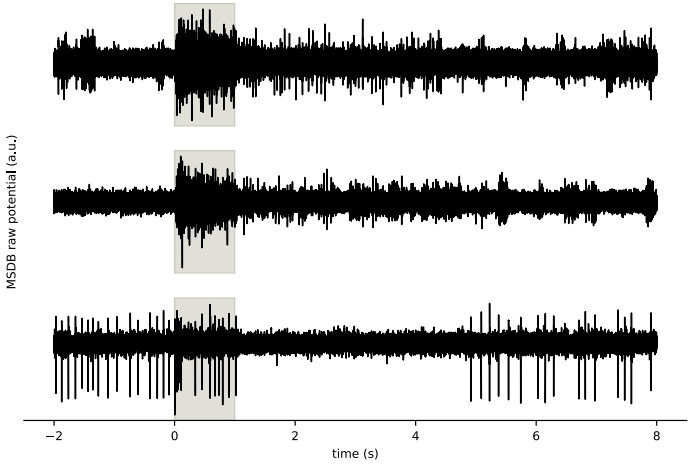

Figure 2.7: **Examples of potential traces in vivo with blocked MS synapses.** Representative traces of raw potentials from the MSDB in vivo after the application of the blocker cocktail. With the blocker cocktail cessation of activity after the stimulus was observed more often than in the intact network, see also Figures 2.3, 2.4. Stimulus period is indicated with the grey region. Reproduced from (Korvasová et al., 2021).

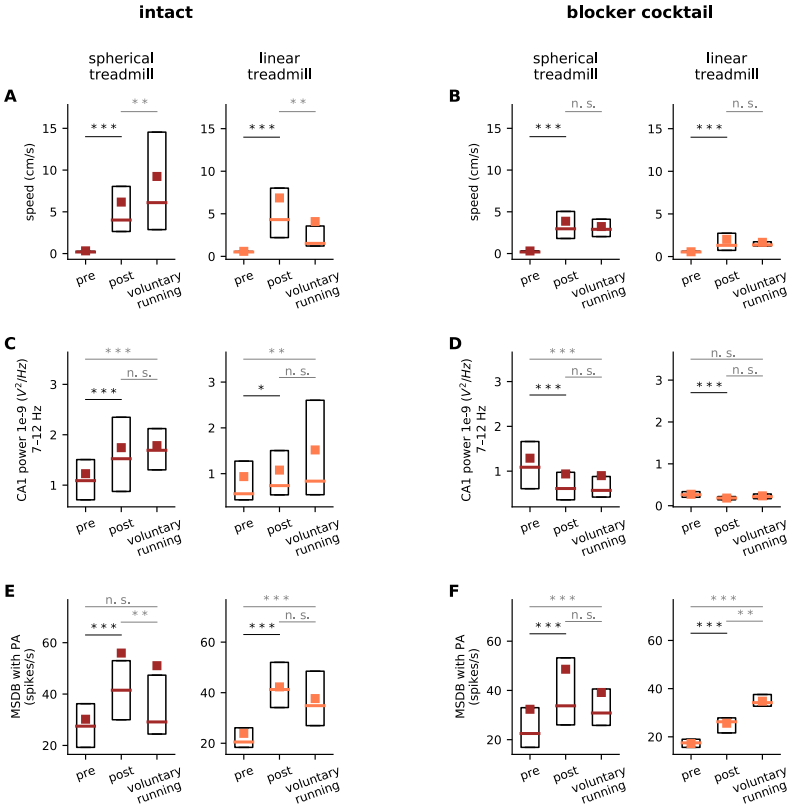

Figure 2.8: **Comparison of results recorded on the spherical (left subcolumn) and linear treadmill (right subcolumn) pre-, post-stimulus and during voluntary running. A.** Running speed with intact MSDB network. **B.** Running speed with blocked synaptic transmission in the MSDB. **C.** Mean CA1 power in the range 7–12 Hz in the intact MSDB network. **D.** Mean CA1 power in the range 7–12 Hz with blocked synaptic transmission in the MSDB. **E.** Mean firing rate in MSDB channels with persistent activity in the intact MSDB network. **F.** Mean firing rate in MSDB channels with persistent activity with blocked synaptic transmission in the MSDB. Additional information is provided in Section 2.6.2. Reproduced from (Korvasová et al., 2021).

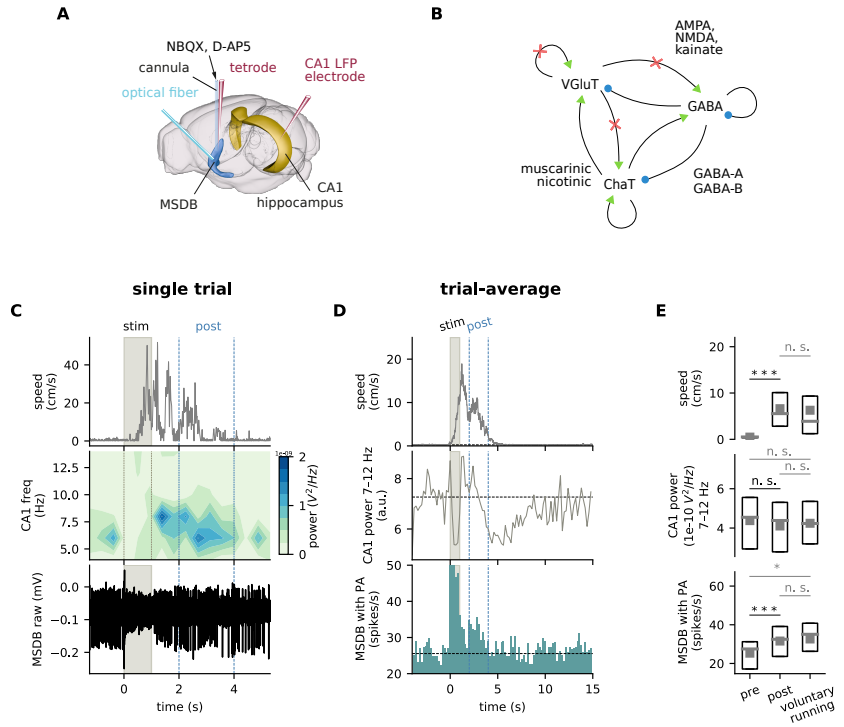

Figure 2.9: **Stimulus response in vivo with blocked MSDB glutamatergic synapses.**
A. NBQX, D-AP5 was applied through a cannula in the MSDB. Produced using The Scalable Brain Atlas (Bezgin et al., 2009), based on The Allen Reference Atlas (Lein et al., 2007). **B.** Types of synapses blocked by NBQX, D-AP5. Excitatory synapses are marked by green arrows and inhibitory by blue circles. **C.** Representative recordings of speed, CA1 LFP with the corresponding spectrogram and MSDB extracellular potential. The grey vertical band marks the continuous light stimulus (0–1s). The grey vertical band marks the continuous light stimulus (0–1 s), the dotted lines mark the time interval used to analyze post-stimulus activity (2–4 s). Same mouse as in Figure 2.1D. **D.** Trial-averaged speed (upper panel), CA1 LFP power in the frequency range 7–12 Hz (middle panel) and the average histogram of multi-unit spiking activity of channels with persistent activity (PA) (lower panel). Average across all recording sessions with 2 mice. For significance of a single-channel positive response to one stimulus repetition, $p < 0.05$ from the one-sided Mann-Whitney U-test applied on inter-spike intervals was required. **E.** Distribution of time-averaged speed (upper panel), CA1 LFP power in the range 7–12 Hz (middle panel) and mean firing rate of channels with PA (lower panel) for time periods when the mouse was at rest, during voluntary running, and within 2 seconds after the stimulus offset. Bar denotes the median, square the mean and the box spans between the first and the third quartile. Additional information is provided in Section 2.6.2. Reproduced from (Korvasová et al., 2021).

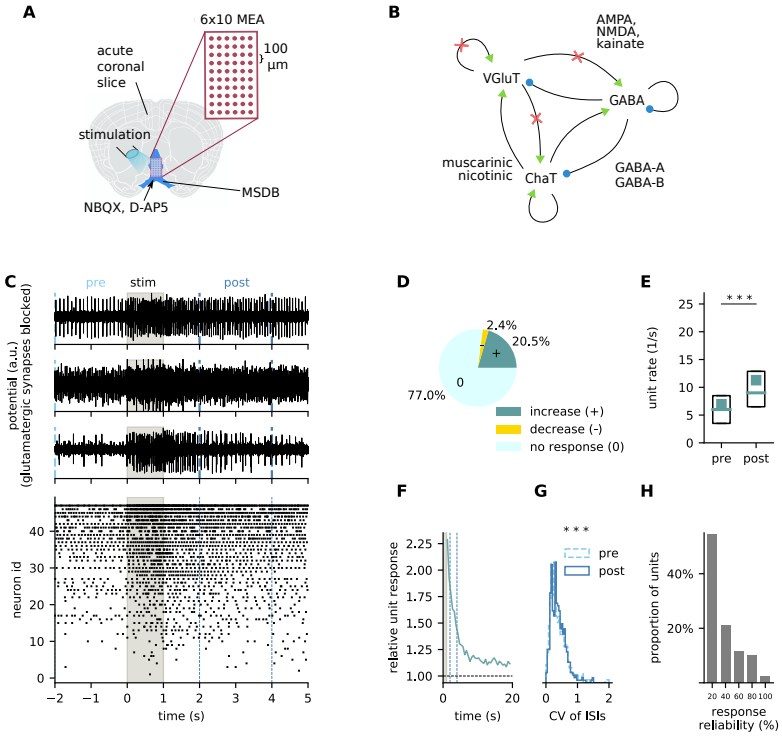

Figure 2.10: **Single-unit response to stimulus in vitro with blocked MSDB glutamatergic synapses.** **A.** Application of NBQX, D-AP5 to the MSDB. Produced using The Scalable Brain Atlas (Bezgin et al., 2009), based on the Allen Reference Atlas (Lein et al., 2007). **B.** Types of synapses blocked by NBQX, D-AP5. Excitatory synapses are marked by green arrows and inhibitory by blue circles. **C.** Representative traces of the extracellular potential in the acute MSDB slice preparation. The grey vertical bands mark the continuous light stimulus (upper panel). Extracted single-unit activity for one representative slice (lower panel). **D.** Percentages of units with significant increase (dark green), significant decrease (yellow) and no significant change (light green) of firing rate. For significance of a single-unit response to one stimulus repetition, $p < 0.05$ from the one-sided Mann-Whitney U-test applied on inter-spike intervals was required. **E.** Distribution of firing rates before and after the stimulus (pre: $(-2, 0)$ s, post: $(2, 4)$ s). Only units with significantly elevated post-stimulus firing rate were considered. Statistical significance of the difference between pooled mean firing rates pre and post: $p = 7.3 \cdot 10^{-29}$ (171 trials, second stimulus repetition out of five). **F.** Trial-averaged time course of single-unit spiking activity. **G.** Distribution of coefficients of variation (CV) or inter-spike intervals (ISIs), pre stimulus ($(-2, 0)$ s, blue) and post stimulus ($(2, 4)$ s, red). **H.** Percentages of units that respond with given reliability across five stimulus repetitions. (Two-sided Wilcoxon's signed-rank test, 13 brain slices.) Reproduced from (Korvasová et al., 2021).

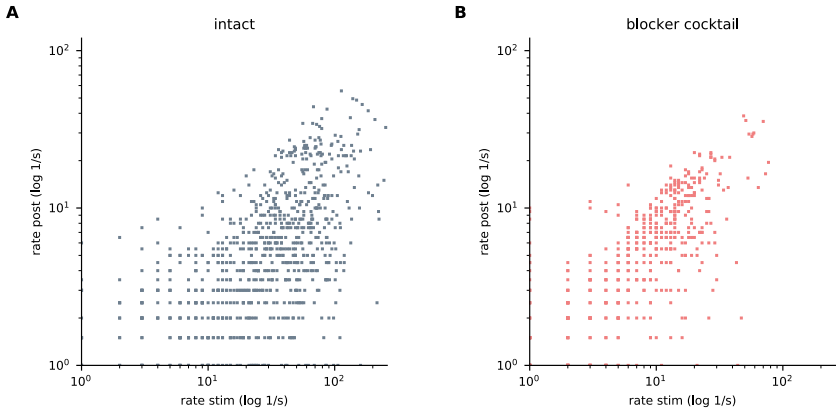

Figure 2.11: **Relationship between the single-unit firing rate during and after the stimulus in vitro.** **A.** Single unit firing rate during the stimulus (horizontal axis) and in the time interval $(2, 4)$ s (vertical axis) in the acute MSDB slice preparation. **B.** As A with blocked synaptic transmission in the MSDB. Reproduced from (Korvasová et al., 2021).

voluntary running $p = 0.0007$, pre-stimulus vs voluntary running $p = 7. \cdot 10^{-6}$. The difference between the speed before the stimulus and during voluntary running was significant by construction. Statistical significance was calculated using the two-sided Wilcoxon's signed-rank test for pre- vs post-stimulus difference (black) and the two-sided Mann-Whitney U-test in other cases (grey).

FIGURE 2.2 All recordings of 3 mice were used, for firing rates only one channel per mouse was considered. Numbers of trials intact: 143 trials with one stimulus realization, out of them 76 show persistent activity, 81 trials with voluntary running, out of them 43 show persistent activity. Statistical significance: pre- vs post-stimulus speed $p = 9.6 \cdot 10^{-24}$, post-stimulus vs voluntary running $p = 0.89$, LFP power pre vs post $7.3 \cdot 10^{-6}$, post-stimulus vs voluntary running $p = 0.56$, pre-stimulus vs voluntary running $p = 0.002$, PA pre vs post $p = 3.6 \cdot 10^{-14}$, post-stimulus vs voluntary running $p = 0.52$, pre-stimulus vs voluntary running $p = 5.9 \cdot 10^{-7}$. The difference between the speed before the stimulus and during voluntary running was significant by construction. Statistical significance was calculated using the two-sided Wilcoxon's signed-rank test for pre- vs post-stimulus difference (black) and the two-sided Mann-Whitney U-test in other cases (grey).

FIGURE 2.8 All recordings of 4 mice in intact and 3 mice in blocked condition were used. For firing rates only one channel per mouse is considered. Statistical significance was calculated using the two-sided Wilcoxon's signed-rank test for pre- vs post-stimulus difference (black) and the two-sided Mann-Whitney U-test in other cases (grey). Numbers of trials intact on the spherical treadmill: 118 with stimulus, 75 of them with persistent activity, 83 trials with voluntary running, 45 of them with persistent activity; intact on the treadmill: 47 trials with stimulus, 44 of them with persistent activity, 38 trials with voluntary running, 34 of them with persistent activity. Blocker cocktail on the spherical treadmill: 110 with stimulus, 60 of them with persistent activity, 60 with voluntary running, 31 of them with persistent activity. Statistical significance, p-values calculated using the two-sided Wilcoxon's signed-rank test for pre- vs post-stimulus difference (black) and the two-sided Mann-Whitney U-test in other cases (grey) in the order pre vs post, post vs voluntary running, pre vs voluntary running:

intact	spherical treadmill	linear treadmill
speed	$\sim 10^{-21}$, 0.0098, –	$\sim 10^{-9}$, 0.002, –
CA1 power 7–12 Hz	$\sim 10^{-5}$, 0.31, $\sim 10^{-7}$	0.02, 0.16, 0.007
firing rate MSDB multi-unit with PA	$\sim 10^{-14}$, 0.006, 0.074	$\sim 10^{-9}$, 0.056, $\sim 10^{-6}$

blocker cocktail	spherical treadmill	linear treadmill
speed	$\sim 10^{-19}$, 0.9, –	$\sim 10^{-6}$, 0.6, –
CA1 power 7–12 Hz	0.0003, 0.6, 0.0002	0.0003, 0.05, 0.18
firing rate MSDB multi-unit with PA	$\sim 10^{-11}$, 0.4, 0.0007	0.0004, 0.0002, $\sim 10^{-5}$

FIGURE 2.9 All recordings of 2 mice were used. Numbers of trials: 47 trials with one stimulus realization, out of them 30 show persistent activity, 18 trials with voluntary running, out of them 12 show persistent activity. Statistical significance: pre- vs post-stimulus speed $p = 2.4 \cdot 10^{-9}$, post-stimulus vs voluntary running $p = 0.48$, LFP power pre vs post 0.72, post-stimulus vs voluntary running 0.88, pre-stimulus vs voluntary running $p = 0.92$, PA pre vs post $p = 1.7 \cdot 10^{-6}$, post-stimulus vs voluntary running $p = 0.73$, pre-stimulus vs voluntary running $p = 0.03$. The difference between the speed before the stimulus and during voluntary running was significant by construction. Statistical significance was calculated using the two-sided Wilcoxon's signed-rank test for pre- vs post-stimulus difference (black) and the two-sided Mann-Whitney U-test in other cases (grey).

3 Spontaneous synchronization of medial septal neurons in the theta frequency range

* * *

The author performed all data analysis and wrote this chapter. The work was supervised by Tom Tetzlaff.

* * *

Hippocampal theta oscillations belong to the most prominent brain rhythms, yet their origin is, despite extensive investigation, still under debate. The hypothesis that the complex of the medial septum and the diagonal band of Broca (MSDB) drives the theta activity was formulated decades ago (Petsche et al., 1962, 1965; Green and Arduini, 1954). Since then, many experiments have been performed aiming at mechanistic understanding of the underlying circuits (for a review see Colom 2006). Two types of theta oscillations have been identified: type 1 theta (7–14 Hz) present during locomotion and explorative behaviour (Whishaw and Vanderwolf, 1973; Oddie and Bland, 1998; Buzsáki, 2002; Fuhrmann et al., 2015), and type 2 (4–9 Hz) that appears during immobility, REM sleep and emotional states such as anxiety (Kramis et al., 1975; Bland, 1986; Sainsbury et al., 1987). Both types of hippocampal theta oscillation critically depend on the input from the MSDB (Mizumori et al., 1989; Vinogradova, 1995; Green and Arduini, 1954). However, the detailed mechanisms of their generation, particularly the dependence on the specific projections from the thee different MSDB cell populations (cholinergic, GABAergic and glutamatergic) differ.

Type 1 hippocampal theta oscillation is only present in active states and disappears under anesthesia (Kramis et al., 1975). It is reliably triggered by optogenetic

stimulation of MSDB glutamatergic (VGluT2) cells (Chapter 2, Fuhrmann et al., 2015; Robinson et al., 2016) or parvalbumin-expressing GABAergic cells (Zutshi et al., 2018). Moreover, the synaptic connectivity within the MSDB appears to be necessary (Chapter 2, Fuhrmann et al., 2015; Robinson et al., 2016). According to the currently accepted view, the rhythmic firing in the theta frequency range is produced by the GABAergic MSDB neurons upon tonic excitation from the MSDB glutamatergic population (Robinson et al., 2016; Kocsis et al., 2021), and projected to the CA1 interneurons. Along with providing rhythmic inhibition, the MSDB further facilitates the hippocampal theta oscillation by disinhibiting hippocampal CA1 pyramidal cells via an interneuron-interneuron circuit. MSDB glutamatergic cells directly activate the hippocampal alveus/oriens interneurons (Fuhrmann et al., 2015) that in turn inhibit another class of hippocampal interneurons, leading to disinhibition of the excitatory input to CA1 pyramidal neurons from the hippocampal area CA3 and the medial entorhinal cortex (Fuhrmann et al., 2015; Leão et al., 2012). It is possible that MSDB VGluT2 cells further depolarize CA1 pyramidal cells by direct septo-hippocampal projections (Fuhrmann et al., 2015), or via activating MSDB cholinergic neurons that target the hippocampal oriens-lacunosum moleculare interneurons with nicotinic receptors (Leao et al., 2015; Fuhrmann et al., 2015).

Type 2 hippocampal theta oscillation occurs during immobility, sleep and anesthesia (Kramis et al., 1975) and can be induced by optogenetic activation of MSDB cholinergic neurons (Vandecasteele et al., 2014; Mikulovic et al., 2018). Unlike type 1 theta, it is abolished by blocking cholinergic transmission in the MSDB by the application of atropine (Kramis et al., 1975; Bland, 1986). The MSDB cholinergic neurons provide excitation to the local MSDB network and to the CA1 pyramidal cells via direct septo-hippocampal projections. Cholinergic neurons do not show strong phase coupling to the theta rhythm measured in the dorsal hippocampus, but increase their firing rate when the theta rhythm is present (Simon et al., 2006; Zhang et al., 2010). However, it is unclear whether the cholinergic neurons phase-lock to a theta oscillation measured at other locations such as the ventral hippocampus, as oscillations with variable frequencies where detected along the hippocampal dorso-ventral axis (Mikulovic et al., 2018; Zhang and Jacobs, 2015). The MSDB interneurons exhibit strong phase coupling to either the peak or the trough of the theta rhythm (Borhegyi et al., 2004) and their activity temporally precedes the emergence of the hippocampal theta oscillation (Hangya et al., 2009). Moreover, Gangadharan et al. (2016) showed that the MSDB GABAergic neurons control object exploration

through modulating type 2 theta oscillation. Thus, the MSDB GABAergic population can be considered as a putative pacemaker of type 2 theta oscillation as well.

Taken together, the MSDB GABAergic subpopulation is a candidate for the pacemaker of both type 1 and type 2 hippocampal theta oscillation, although more experiments will be needed to describe the mechanism. Under this hypothesis, MSDB glutamatergic and cholinergic neurons provide excitatory drive to the network and thereby possibly modulate the theta oscillation in a state-dependent manner, e.g. during locomotion (Fuhrmann et al., 2015) or arousal (Sainsbury et al., 1987), respectively. A recent study (Kocsis et al., 2021) proposed that the theta rhythm is generated by MSDB PV cells that, upon tonic excitation provided by the glutamatergic cells, intrinsically produce regular firing in the theta frequency range. They are then synchronized by the network, similarly to initially asynchronous clocks attached to one wall. However, detailed understanding of the underlying cellular and network mechanism is still missing. Theta rhythmicity among the MSDB interneurons strongly correlates with the expression of hyperpolarization-activated cation channels that promote membrane oscillations, but their activation is not necessary for the existence of theta-rhythmic firing in the MSDB (Varga et al., 2008).

Several attempts have been performed to induce theta oscillation in a MSDB slice preparation, with the help of activating specific receptors types. Theta oscillation in the local field potential was recorded from a rat medial septal slice upon the application of nicotine (Wen et al., 2013), kainate (Garner et al., 2005) or a metabotropic glutamate receptor agonist (Lu et al., 2011). However, the application of the cholinergic agonists nicotine (Lu and Henderson, 2010) or carbachol (Manseau et al., 2008) induces theta oscillation also in a hippocampal slice preparation. These experiments show the ability of both the septal and hippocampal local networks to support theta oscillations, but specific external input substituted by specific receptor activation may still be necessary. In this study, we investigated whether the MSDB network generates rhythmic firing in the theta frequency range spontaneously in an acute MSDB slice preparation without any additional activation of specific receptors. Furthermore, we pharmacologically blocked synaptic transmission in the MSDB to test whether the oscillation is generated by intrinsic mechanisms of the MSDB cells or critically relies on synaptic connectivity.

3.1 Medial septal cells spontaneously synchronize in the theta frequency range

The same dataset as in Chapter 2 was analyzed. An acute coronal MSDB slice preparation was placed inside an oxygenation chamber (Figure 3.1A) onto a 6x10 micro-electrode array (Figure 3.1B). To investigate the existence of spontaneous spiking activity and synchronization in the theta frequency range, we extracted the time intervals prior to the first optical stimulation in each trial, with length up to 1 minute. For each slice, single unit activity was extracted and the population activity was computed as a histogram of pooled single-unit activities of all units. Experimental and analysis methods are described in detail in Sections 2.5 and 3.3, respectively.

Spontaneous spiking activity was present but too sparse for the theta oscillation to be detectable by eye in the population signal (Figure 3.1C). However, the autocorrelation function of the population signal showed a clear rhythmicity in the theta-frequency range (Figure 3.1D, black). The theta oscillation in the autocorrelation function were not fully determined by single-unit autocorrelations, as the average of single-unit autocorrelations (orange) was more flat, indicating synchonization between different units. The power spectral density also showed a clear peak in the theta frequency range (Figure 3.1E). To quantify the significance of the theta oscillation and the importance of cross-correlations in its generation, we performed surrogate analysis with two types of surrogate data: spike dither and spike train dither (see Section 3.3 for details). With spike dither, each individual spike is dithered by a random displacement, destroying the structure of both population and single-unit autocorrelation functions. The significance threshold obtained by this methods therefore tests significance of the theta oscillation per se. The spike train dither only affects population autocorrelations and preserves single-unit autocorrelations, thereby testing significance of pairwise cross-correlations between different units. Both methods preserve the mean firing rate of each unit. The theta peak in the power-spectral density was significant in 39 out of 86 trials according to the spike dither surrogate method and the cross-correlations were significant in 37 trials according to the spike train dither surrogate method (Figure 3.1F). The dominant frequency of the theta oscillation typically lay in the high theta band (8-14 Hz, Figure 3.1G).

To test whether the synchronization observed in the intact slice critically depends on synaptic connectivity, we repeated the same analysis with recordings obtained

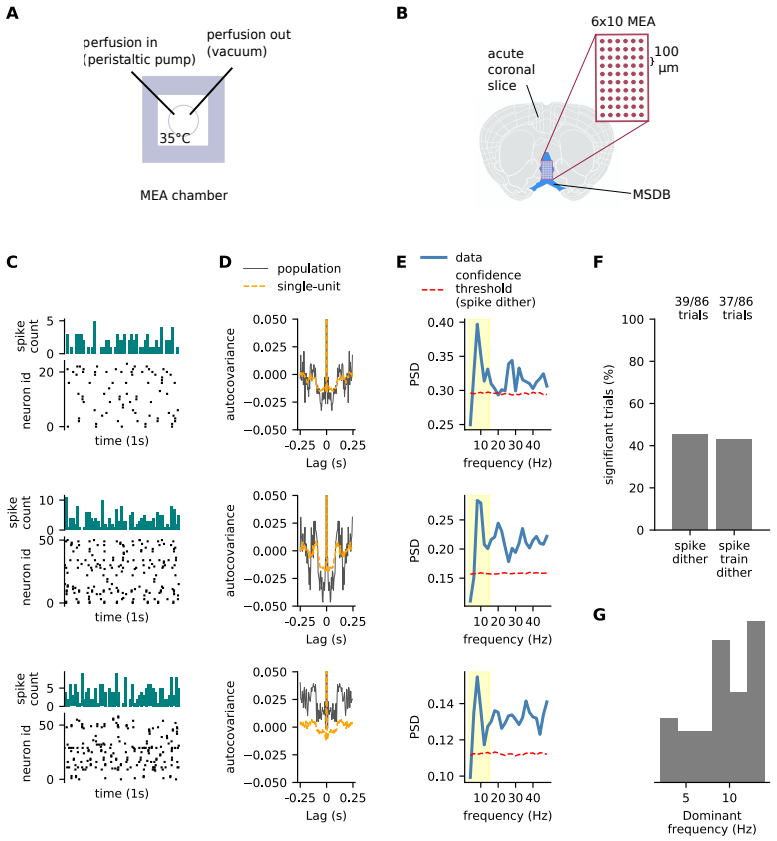

Figure 3.1: **Synchronization of neurons in the MSDB acute slice preparation in the theta frequency band.** **A.** Sketch of the experimental setup. **B.** An acute coronal slice is positioned on a 6x10 MEA with electrode distance 100 μm. Produced using The Scalable Brain Atlas (Bezgin et al., 2009), based on the Allen Reference Atlas (Lein et al., 2007). **C.** Examples of single-unit spiking activity in 3 MSDB acute slices (lower panel). Instantaneous population firing rate (bin size 20ms; upper panel, green). **D.** Normalized autocovariance function of the population firing rate (black) and the average of the single-unit autocovariance functions (orange), corresponding to the examples in A. Spikes were binned with 5 ms bin size. **E.** Power spectral density of the instantaneous population firing rate (bin size 2 ms) (blue). The confidence threshold (red) was calculated using surrogate analysis (spike dither, 1000 surrogate sets) with confidence threshold $\alpha = 0.05$. Significance was tested in the interval 4-14 Hz (yellow). **F.** Percentage of slices with significant theta power based on two surrogate methods: spike dither and spike train dither. **G.** Distribution of the dominant frequency in the range 4-14 Hz across slices.

from slices with blocked synaptic transmission (Figure 3.2A-C). We observed even more pronounced peaks in the autocorrelation functions and power spectra (Figure 3.2D,E). Moreover, the theta power was significant in almost all trials 3.2E. The level of theta-band interactions between neurons was not affected by the blocker, as the proportion of significant trials with respect to spike-train dither was similar as in the intact network (Figure 3.2E). On the contrary, the proportion of significant trials with respect to spike dither was much higher compared to the intact network and also compared to spike-train dither, indicating more regular spiking after the application of the blocker. In many trials, the significant theta power in the population activity therefore recflected periodic single-unit activity. The dominant frequency was even more biased towards the high theta range than in the intact network (Figure 3.2G).

Next, we sought to understand the role of the different types of MSDB synaptic connections in the generation of the theta activity by performing pharmacological manipulations. We first applied NBQX, D-AP5 that block glutamatergic receptors and then blocked all synaptic connections by the application of the blocker cocktail (Figure 3.3A). The dominant theta frequency was higher in the blocked conditions than in the intact network (Figure 3.3B) with the highest relative power (normalized by mean power) after the application of the blocker cocktail (Figure 3.3C). However, the coefficients of variation of the inter-spike intervals were lowest in the fully blocked condition (Figure 3.3D), which is consistent with our previous observation that without synaptic transmission the theta power is mainly a result of single-unit autocorrelations, rather than synchrony. On the contrary, the relatively low dominant frequencies in the intact network (Figure 3.3B) seem to depend on the MSDB network dynamics, as the firing rates were on average higher than in the other two conditions (Figure 3.3E). Indeed, the units with most regular spiking (lowest coefficient of variation of the inter-spike intervals) tend to have high firing rates (typically above 10 spikes/s) compared to the less regular units in all three conditions (Figure 3.3F).

To test how synchrony of neurons depends on their distance, we computed the Pearson's correlation coeficient and coherence for every pair of neurons. The Peason's correlation coefficient is phase-sensitive, whereas coherence describes the spectrum of the cross-correlation function and is therefore phase-independent. Synchronous firing, as measured by the Peason's coefficient of variation, was not affected by the synaptic blockers and occured mostly between neurons recorded at the same electrode (Figure 3.4B). The theta-band coherence between neurons was also highest between neighbouring neurons. In the intact network and after the application of

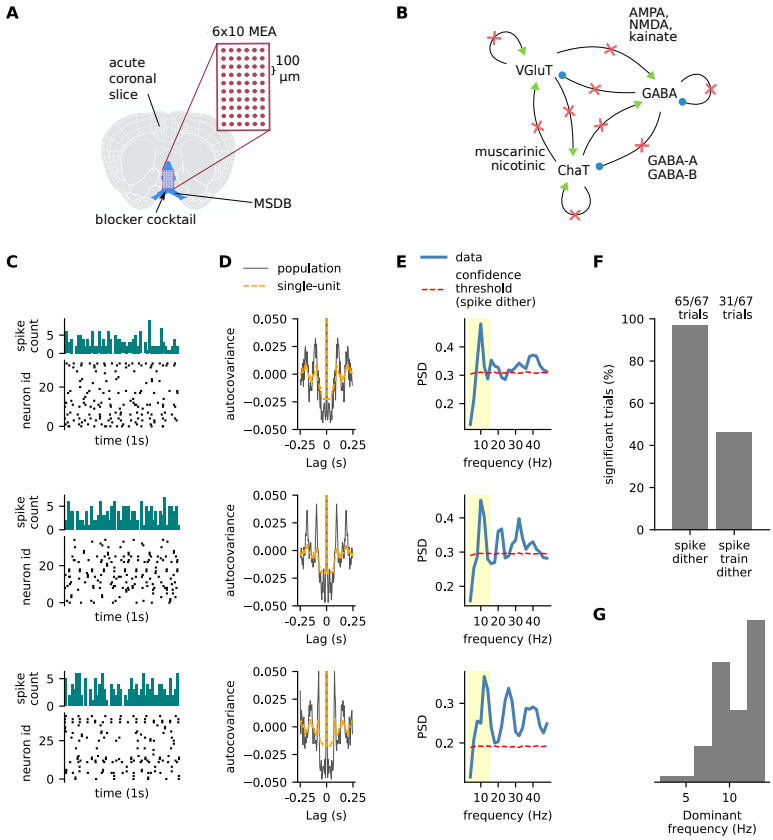

Figure 3.2: **Synchronization of neurons in the MSDB acute slice preparation with blocked synaptic transmission. A.** Application of the blocker cocktail to the MSDB. Produced using The Scalable Brain Atlas (Bezgin et al., 2009), based on The Allen Reference Atlas (Lein et al., 2007). **B.** Types of synapses blocked by the blocker cocktail. Excitatory synapses are marked by green arrows and inhibitory by blue circles. **C-G.** Same arrangement as in Figure 3.1 C-G.

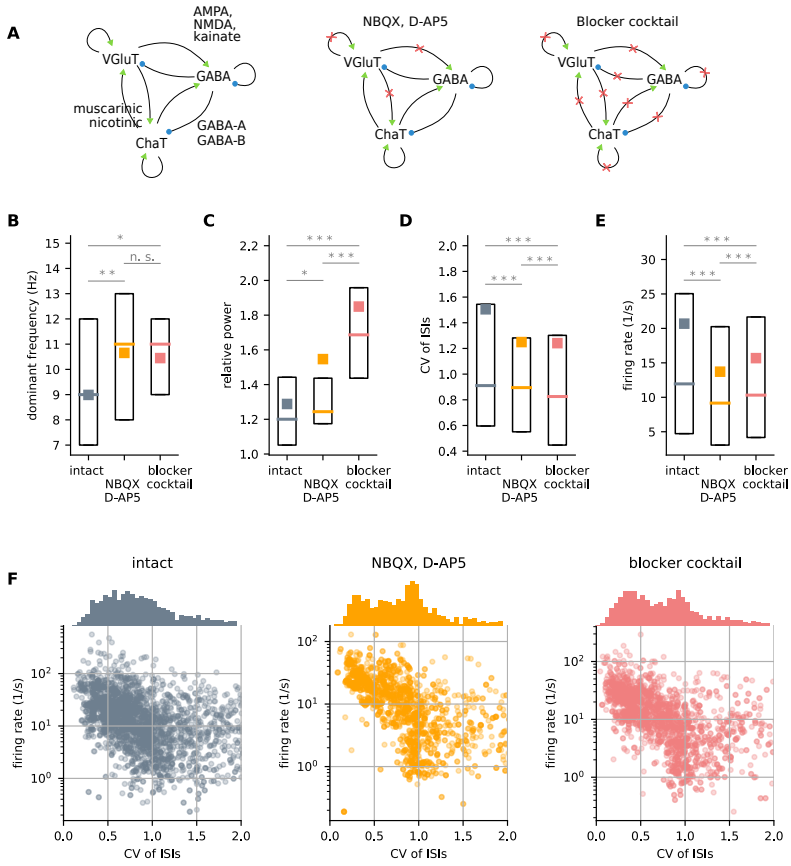

Figure 3.3: **Effect of synaptic transmission on theta synchronization in the acute MSDB slice. A.** Sketches of MSDB connectivity in the intact slice, with glutamatergic synapses blocked by NBQX, D-AP5 and with all synapses blocked by the blocker cocktail. Excitatory synapses are marked by green arrows and inhibitory by blue circles. **B.** Dominant frequencies in the range 4-14 Hz in the intact MSDB slice preparation (grey), with blocked glutamatergic transmission by NBQX, D-AP5 (orange) and with all synapses blocked (pink). Bar denotes the median, square the mean. Mann-Whitney U-test, p-values top to bottom: 0.02, 0.44, 0.007. **C.** Relative power (power at dominant frequency normalized by the mean power) in the three pharmacological conditions . Mann-Whitney U-test, p-values top to bottom: $7.8 \cdot 10^{-12}$, $4.6 \cdot 10^{-7}$, 0.01. **D.** Coefficients of variation (CV) of the inter-spike intervals (ISIs) in the three pharmacological conditions. Mann-Whitney U-test, p-values top to bottom: $4.4 \cdot 10^{-18}$, 0.0006, $4.7 \cdot 10^{-6}$. **E.** Distribution of the mean firing rate across slices in the three pharmacological conditions. Mann-Whitney U-test, p-values top to bottom: $1.8 \cdot 10^{-6}$, 0.0002, $1.6 \cdot 10^{-16}$. **F.** The mean coefficient of variation of the inter-spike intervals vs. the mean firing rate. One dot corresponds to one trial.

the blocker cocktail, somewhat elevated levels of coherence were observed at all distances (Figure 3.4D), indicating a tendency of MSDB neurons to fire at consistent frequencies. The notably lower coherence across all frequencies with blocked glutamatergic transmission (Figure 3.4C) was possibly caused by a group of irregularly firing neurons that generated the dominant peak in the distribution of coefficients of variation of the inter-spike intervals around 1 (Figure 3.3, NBQX, D-AP5).

3.2 Discussion

We have shown that MSDB neurons in an acute slice preparation spontaneously synchronize in the theta frequency band (Figure 3.1). These results support the view of the MSDB as a pacemaker of the hippocampal theta oscillation and show for the first time that the MSDB can generate theta oscillation intrinsically, independently of any external input or specific receptor activation. In particular, the hippocampal feedback to the MSDB is not necessary for generating the MSDB theta-rhythmic activity.

Garner et al. (2005) demonstrated that a kainate-induced MSDB theta oscillation in vitro is abolished by pharmacological blockade of gap junctions. Our results further support the hypothesis that gap junctions are involved in synchronizing the MSDB cells, as we observed significant (Figure 3.2) and mostly local (Figure 3.4) synchronization in the theta frequency band even in the presence of synaptic blockers. However, the theta oscillation in the hippocampal local field potential disappears when MSDB recurrent synaptic connections are blocked (Chapter 2, Robinson et al. (2016)). As opposed to the thalamic theta rhythm (Hughes et al., 2004), the hippocampal theta rhythm is synchronized by a more complex mechanism than by the gap junctions alone. In particular, $GABA_A$ signaling seems to be involved (Garner et al., 2005). With blocked synapses we typically observed dominant theta frequencies above 8 Hz (Figure 3.3). It is therefore possible that MSDB synaptic connections are necessary to achieve the low theta frequencies ($4 - 7$ Hz) often detected in the hippocampus (Kramis et al., 1975; Sainsbury et al., 1987).

The relative theta power was highest with blocked synaptic transmission (Figure 3.3), where the theta peak in the power spectrum is largely (but not only) determined by regular spiking of individual units. The mechanism how such regular spiking is generated is unknown, but might involve the metabotropic glutamate receptors (mGluRs). In line with this hypothesis, Lu et al. (2011) induced theta oscillations in the local field potential in a rat MSDB slice preparation by activating

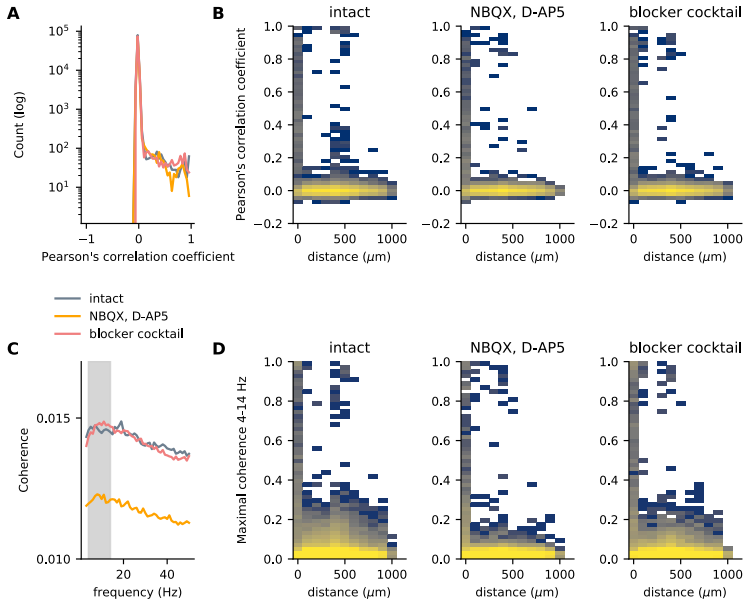

Figure 3.4: **Dependence of cross-correlation and coherence of two units on their distance.** **A.** Histogram of Pearson's correlation coefficients between binned single unit activities (bin size 10 ms) within each slice for the three different pharmacological conditions (intact MSDB slice, blocked glutamatergic transmission with NBQX, D-AP5 and entirely blocked synaptic transmission by the blocker cocktail). **B.** Two-dimensional histogram of Pearson's correlation coefficients between two units vs. their distance. Pooled data from different slices for the each pharmacological condition. **C.** Trial-averaged coherence of binned single-unit activities (bin size 10 ms) within each slice for each pharmacological condition. Grey region marks the interval 4-14 Hz. Note that the y-axis does not start from 0. **D.** Two-dimensional histogram of the maximal coherence in the range 4-14 Hz between two units vs. their distance. Pooled data from different slices for each pharmacological condition.

the metabotropic glutamate receptors. As ionotropic glutamatergic receptors were blocked by competitive blockers in our study, it is likely that mGluRs were more strongly activated in the blocked condition, possibly leading to more regular spiking and higher frequencies (Figure 3.3).

Our approach of studying the generation of theta oscillations in the MSDB by analyzing single-unit spiking activity allowed us to detect synchrony that was not exhibited in the local field potential, possibly due to the morphology of MSDB cells. On the other hand, this method is obviously limited by undersampling. It would therefore be of high value to confirm our results using modern micro-electrode arrays with a high number of channels. Furthermore, repeating the experiment with pharmacologically blocked gap junctions and mGluRs respectively would lead to a better understanding of the underlying mechanisms.

3.3 Methods

3.3.1 Experimental procedure

The experimental procedure was described in detail in Section 2.5. For the analysis presented in this section we extracted time intervals before the first optical stimulation. Recordings with any type of stimulation were used, as the stimulus period did not enter the analysis. In total we analyzed 19 intact slices, 11 slices with NBQX, D-AP5 and 11 slices with the blocker cocktail.

3.3.2 Data analysis

3.3.2.1 Software

Data analysis was performed using custom-written scripts in Python v3.6.10, with the packages Numpy v1.19.2, Scipy v1.5.2, Neo v0.7.1, Elephant v0.6.2 and Matplotlib v3.3.2. Single units were isolated from extracellular potentials using Mountainsort v3 (Barnett et al., 2016).

3.3.2.2 Data selection

The time interval before the first stimulus was extracted from recordings with any stimulus paradigm. Only slices with at least 10 extracted units were considered.

3.3.3 Instantaneous firing rate, correlations and spectral analysis

The instantaneous firing rate is calculated as a histogram of spikes normalized by the bin size. In the case of a population firing rate, the signal is normalized by the number of neurons to account for different population sizes in different slices.

Normalized autocovariance function in Figures 3.1D and 3.2D was calculated from the instantaneous firing rate (5 ms bin size) by taking a z-score, dividing by the euclidean norm of the z-scored signal and computing the autocorrelation function using `scipy.signal.correlate`. The black trace was calculated from the population instantaneous firing rate. The yellow trace is an average of normalized autocovariances of the single-unit instantaneous firing rates.

Power spectral density was calculated using Fourier analysis (`scipy.signal.welch`) with minimal frequency resolution of 2 Hz.

The Pearson's correlation coefficient of vectors x and y is defined as

$$\frac{\sum_i (x_i - \mu(x))(y_i - \mu(y))}{\sigma(x)\sigma(y)},$$

where μ denotes the mean and σ the standard deviation.

Coherence of vectors x and y, sometimes referred to as magnitude squared coherence, is defined as $|P_{xy}|^2/(P_x P_y)$, where P_x, resp. P_y, are power spectral densities of x, resp. y, and P_{xy} is the cross-spectral density of the two vectors.

3.3.3.1 Statistical testing

Surrogate data sets were generated by randomly dithering the spike times (spike dither) or the whole single-unit spike trains (spike train dither) within ± 200 ms. A theta peak in the power spectral density was considered significant when the maximum of the power-spectral density in the range 4-14 Hz was above the maximum of the 95th percentile of surrogate power spectra in the same range.

Statistical significance in Figure 3.3 was calculated using the non-parametric Mann-Whitney U-test.

4 Framework for studying the generation of periodic travelling waves in spiking neural networks

* * *

This chapter is based on the publication (Senk et al., 2020a). The author performed the initial linear stability analysis of the neural field model, wrote the simulation with rate neurons, contributed to the parameter mapping between the two models and to the writing of the manuscript. The work was done under supervision of Moritz Helias and Markus Diesmann. Figures in this chapter were reproduced from (Senk et al., 2020a) including the captions.

* * *

Travelling waves of electrical activity in the brain have attracted attention for decades, yet their functional role and origin are to date not well understood. They occur both spontaneously and as a response to a stimulus, in awake and anesthetized states, in vivo and in vitro (Muller and Destexhe, 2012; Muller et al., 2018). Their characteristics, however, differ between the conditions (Muller et al., 2018).

Travelling waves have also been observed in neural network models with distance-dependent connectivity (Mehring et al., 2003; Yger et al., 2011; Voges and Perrinet, 2012; Keane and Gong, 2015), where the probability of a connection between two neurons decays with their distance, as reported by experimental studies (Hellwig, 2000; Perin et al., 2011; Schnepel et al., 2015). The origin of travelling waves and other spatio-temporal patters was extensively studied in neural-field models (Wilson and Cowan, 1972b, 1973b; Amari, 1977) that describe the evolution of the popula-

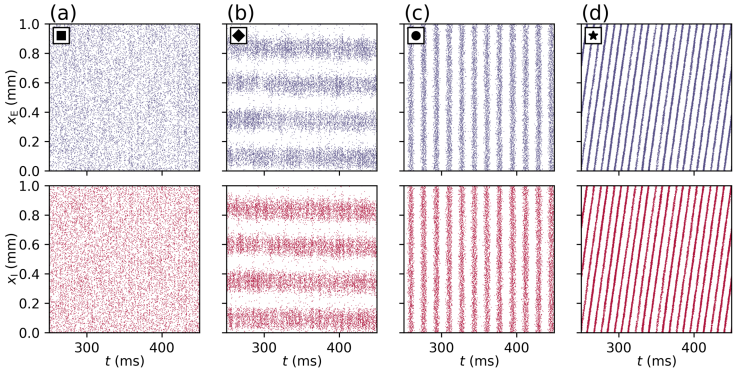

Figure 4.1: Spatiotemporal patterns in a spiking neural network model. Spiking activity of recurrently connected populations of excitatory (E, blue) and inhibitory (I, red) leaky integrate-and-fire neurons. Each dot represents the spike-emission time of a particular neuron. Neurons are positioned on a ring with a circumference of 1 mm. Each neuron receives a fixed number of incoming connections from its excitatory (inhibitory) neighbors uniformly and randomly drawn within a distance of R_E (R_I). The spike-transmission delay d, the widths R_E and R_I of the spatial connectivity profiles, and the relative inhibitory synaptic weight g are varied. (a) Asynchronous-irregular activity ($d = 1\,\text{ms}$, $R_E = R_I = 0.4\,\text{mm}$, $g = 6$). (b) Oscillations in space ($d = 3\,\text{ms}$, $R_E = 0.1\,\text{mm}$, $R_I = 0.15\,\text{mm}$, $g = 5$). (c) Oscillations in time ($d = 6\,\text{ms}$, $R_E = R_I = 0.4\,\text{mm}$, $g = 7$). (d) Propagating waves ($d = 3\,\text{ms}$, $R_E = 0.2\,\text{mm}$, $R_I = 0.07\,\text{mm}$, $g = 5$). For remaining parameters, see Table 4.4. Reproduced from (Senk et al., 2020a).

tion activity in a spatially-resolved manner by nonlinear integro-differential equations. These models are ideal for studying the existence and uniqueness of various spatio-temporal patterns such as travelling waves, stationary patters or travelling bumps (Ermentrout, 1998; Coombes, 2005; Wyller et al., 2007a; Coombes, 2010; Bressloff, 2012, 2014; Coombes et al., 2014), as they are analytically tractable. Such spatio-temporal patterns can either be directly constructed (Amari, 1977; Ermentrout, 1998; Bressloff, 2012) or their existence can be proven by linear stability analysis (Ermentrout and Cowan, 1979b,a, 1980a,b; Hutt et al., 2003). The first, constructive approach has the advantage of working directly with the nonlinear system and therefore providing exact solutions. The latter approach, on the other hand, leads to approximate results that are valid only locally, but offers a more general understanding of the dynamical system.

In this chapter, we employ linear stability analysis to study bifurcations of a homogeneous steady state (Figure 4.1a, in neural networks also called asynchronous,

irregular activity; Brunel, 2000) that give rise to spatial oscillations (constant in time, oscillatory in space, often called "Turing patterns"[1], Figure 4.1b), temporal oscillations (constant in space, oscillatory in time Figure 4.1c) or wave trains (oscillatory both in time and space, also called periodic travelling waves, Figure 4.1d). Our analysis builds on previous work of Veltz and Faugeras (2011) who proved the principle of linearized stability for neural field models of the type considered in this chapter. The existence and uniqueness of solutions, as well as conditions for asymptotic stability of the trivial steady state were previously shown by (Faye and Faugeras, 2010). Numerous other works investigated pattern formation in relation to reach of excitation and inhibition (Ermentrout, 1998), in systems without transmission delays (Wyller et al., 2007b; Folias and Ermentrout, 2012), with constant delays (Roxin et al., 2005, 2006), distance-dependent delays (Jirsa and Kelso, 2000; Hutt et al., 2003; Atay and Hutt, 2005, 2006; Coombes et al., 2007; Bressloff and Kilpatrick, 2008; Hutt, 2008; Bojak and Liley, 2010; Hutt and Rougier, 2010) or both (Veltz, 2011, 2013).

The goal of this chapter is to provide a link between the analytically obtained conditions for the emergence of travelling waves in the neural-field model, and conditions for parameters of a network of leaky-integrate-and-fire neurons that will lead to the same behaviour at the macroscopic level. The latter model is a bottom-up model described on the level of individual neurons (modelled as points in space) and the connections between them. Its parameters are therefore more easily constrained by electro-physiological experiments, but the resulting complexity of the model does not allow for analytical investigation. So far, a quantitative link between the two levels of description is missing.

Several studies have already attempted to create a link between spatio-temporal patterns in models at different levels of description. To name a few, Roxin et al. (Roxin et al., 2005, 2006) used bifurcation theory to compare spatio-temporal patterns in a neural-field model and a network of Hodgkin-Huxley neurons. However, the network simulation did not reveal travelling waves as predicted by the neural field model. Crook et al. (1997) found travelling waves both in a network of coupled oscillators and its mean-field description. An analytical reduction of dynamics of a spiking neural network was performed in the limit of slow synaptic interactions (Ermentrout, 1994; Bressloff and Coombes, 1998, 2000), in spatially extended networks

[1]The term "Turing patterns" refers to the original work by Alan Turing (Turing, 1952) who studied stationary spatial patterns that emerge due to diffusion in reaction-diffusion equations. The term has later acquired a broader meaning of stationary spatial patterns of any origin (Coombes, 2005; Coombes et al., 2007; Venkov et al., 2007).

of leaky-integrate-and-fire (LIF) neurons without transmission delays (Rosenbaum and Doiron, 2014; Rosenbaum et al., 2017) and with constant delays (Kriener et al., 2014), but without the explicit spatial dependence in the mean-field description.

In this chapter, we present a quantitative link between a ring network of LIF neurons with delays and the corresponding neural-field model. We derive an explicit parameter mapping between the two models and apply it to find conditions for parameters of both neural-field and LIF network models when wave trains (periodic travelling waves) occur. We validate the results obtained by linear stability analysis of the neural-field model by a simulations of networks of LIF or rate neurons.

4.1 Bifurcation analysis of a neural-field model

Let us first consider a one-dimensional domain $\mathbb{R}$ populated with one neural population. Let $u : \mathbb{R}^2 \to \mathbb{R}$ be the instantaneous firing rate of infinitely small neurons described as a continuous field, $\psi : \mathbb{R} \to \mathbb{R}$ a translation-invariant gain function, $d > 0$ the transmission delay and $\tau > 0$ the effective time constant. Let $m : \mathbb{R} \to \mathbb{R}$ be a translation in variant, isotropic connectivity kernel that specifies the effective strength of connection between two neurons at positions $x \in \mathbb{R}$ and $y \in \mathbb{R}$,

$$m(r) \coloneqq w\, p(r), \tag{4.1}$$

where $r = x - y$ is the displacement, $w \in \mathbb{R}$ is the strength of connection and $p : \mathbb{R} \to (0, \infty)$ a symmetric probability density function such that $p(r) = p(-r)$ and $\int_{-\infty}^{\infty} p(r)\,\mathrm{d}r = 1$. The temporal evolution of u is then described by the neural-field model

$$\tau \frac{\partial u}{\partial t}(x,t) + u(x,t) = \int_{-\infty}^{\infty} m(x-y)\, \psi(u(y, t-d))\,\mathrm{d}y. \tag{4.2}$$

In Section 4.3 we extend the analysis to a two-population model, with one excitatory ($w > 0$) and one inhibitory ($w < 0$) population. We restrict our analysis to a one-dimensional ring domain, i.e. $n = 1$. We consider a boxcar-shaped connectivity kernel of width R (Figure 4.2(a)) ,

$$p(r) = \frac{1}{2R}\Theta(R - |r|), \tag{4.3}$$

where Θ denotes the Heaviside function.

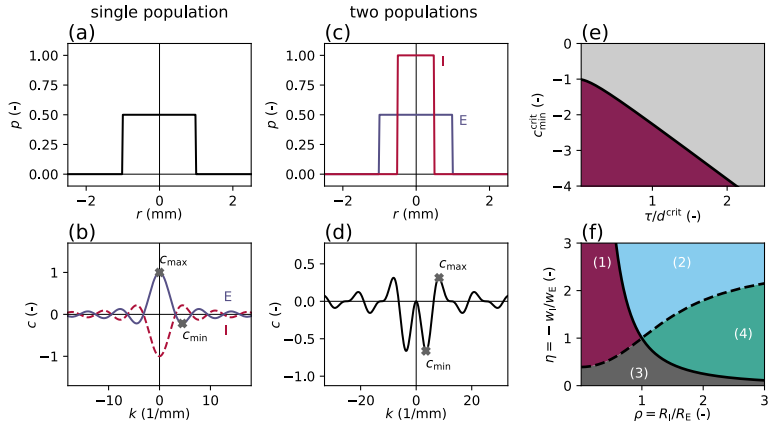

Figure 4.2: Effective profile yields conditions for wave trains. (a) Boxcar-shaped spatial profile p of width $R = 1\,\text{mm}$ for a single population. (b) Effective profile c (blue curve) denotes Fourier transform of spatial profile $\widehat{p}$ times positive weight $w_\text{E} = 1$. Gray crosses indicate maximum c_max and minimum c_min. Same spatial profile but with negative weight ($w_\text{I} = -w_\text{E}$) yields mirrored curve (red, dashed line). (c) Spatial profiles of different widths for two populations E ($R_\text{E} = 1\,\text{mm}$, blue) and I ($R_\text{I} = 0.5\,\text{mm}$, red). (d) Effective profile: $c(k) = w_\text{E}\widehat{p}_\text{E}(k) + w_\text{I}\widehat{p}_\text{I}(k)$. (e) Transition curve $c_\text{min}^\text{crit}(\tau/d^\text{crit})$ given by Equation 4.13 for Hopf bifurcation indicating onset of delay-induced oscillations (appearing in purple region) with time constant τ and delay d. (f) Transition curves for relative width $\rho = R_\text{I}/R_\text{E}$ and relative weight $\eta = -w_\text{I}/w_\text{E}$. Colored regions indicate which extremum, the minimum c_min or the maximum c_max, has larger absolute value and if the dominant one occurs at $k = 0$ or at $k > 0$. Purple (1): c_min appears at $k_\text{min} > 0$. Light blue (2): c_min appears at $k_\text{min} = 0$. Dark gray (3): c_max appears at $k_\text{max} = 0$. Green (4) c_max appears at $k_\text{max} > 0$. Reproduced from (Senk et al., 2020a).

To analyze stability of the stationary steady state $u(x,t) = u_0$, we linearize the system in the neighbourhood of the steady state u_0: $\delta u(t) = u(t) - u_0$. Without loss of generality we assume $\psi'(u_0) = 1$, as it can be compensated by rescaling the coupling strength w. We apply the standard ansatz

$$\delta u(x,t) = \mathrm{e}^{\mathrm{i}kx}\mathrm{e}^{\lambda t}, \tag{4.4}$$

where the wave number $k \in \mathbb{R}$ is real and the temporal eigenvalue $\lambda \in \mathbb{C}$ is complex, and arrive at the characteristic equation

$$(1 + \tau\lambda)\,\mathrm{e}^{\lambda d} = c(k), \tag{4.5}$$

with $c(k) \coloneqq \widehat{m}(k) \coloneqq w\widehat{p}(k)$. For more details on the derivation see Equation 4.36. The Fourier transform of the spatial profile $\widehat{p}(k)$ is maximal at $k = 0$ with $\widehat{p}(0) = 1$ (see Eqs. 4.42 and 4.43). Figure 4.2(b) shows the effective profile derived from the boxcar spatial profile for excitatory and inhibitory weights.

Next, we extend the model to a system of coupled excitatory (E) and inhibitory (I) populations, assuming identical time constants τ and delays d. Then u becomes a vector, $u = (u_\mathrm{E}, u_\mathrm{I})^T$, and the connectivity $m(r)$ a matrix

$$M(r) = \begin{pmatrix} w_{\mathrm{EE}}\, p_{\mathrm{EE}}(r) & w_{\mathrm{EI}}\, p_{\mathrm{EI}}(r) \\ w_{\mathrm{IE}}\, p_{\mathrm{IE}}(r) & w_{\mathrm{II}}\, p_{\mathrm{II}}(r) \end{pmatrix}. \tag{4.6}$$

By applying the ansatz $\delta u(x,t) = v e^{\mathrm{i}kx}\mathrm{e}^{\lambda \mathrm{t}}$ with a constant vector v, we arrive at an auxiliary eigenvalue problem (see Equation 4.37) with the two solutions

$$c_{1,2}(k) = \frac{1}{2}\Big(w_{\mathrm{EE}}\,\widehat{p}_{\mathrm{EE}}(k) + w_{\mathrm{II}}\,\widehat{p}_{\mathrm{II}}(k) \pm \sqrt{D}\Big), \tag{4.7}$$

where the discriminant reads

$$D = \left(w_{\mathrm{EE}}\,\widehat{p}_{\mathrm{EE}}(k) - w_{\mathrm{II}}\,\widehat{p}_{\mathrm{II}}(k)\right)^2 + 4w_{\mathrm{EI}}\,\widehat{p}_{\mathrm{EI}}(k)\, w_{\mathrm{IE}}\,\widehat{p}_{\mathrm{IE}}(k). \tag{4.8}$$

For further analysis we assume that the weights and the spatial profiles are independent of the target population: $w_{\alpha\mathrm{E}} =: w_\mathrm{E}$, $w_{\alpha\mathrm{I}} =: w_\mathrm{I}$ for $\alpha \in \{\mathrm{E}, \mathrm{I}\}$. Equation 4.7 then reduces to $c_1(k) = w_\mathrm{E}\widehat{p}_\mathrm{E}(k) + w_\mathrm{I}\widehat{p}_\mathrm{I}(k) =: c(k)$ and $c_2 \equiv 0$ for all k. Figure 4.2 illustrates the two spatial profiles of widths R_E and R_I (Figure 4.2(c)) and the resulting effective profile (Figure 4.2(d)).

To prove asymptotic stability of the homogeneous steady state u_0, it is sufficient to show that all eigenvalues λ determined by Equation 4.5 have negative real parts (Veltz and Faugeras, 2011). The principle of linearized stability from (Veltz and Faugeras, 2011) is applied rather heuristically in our work, as Veltz and Faugeras (2011) performed their analysis rigorously on a ring (a bounded domain with periodic boundary conditions), while we consider an unbounded domain. The choice of the unbounded domain leads to eigenvalues that depend continuously on the wavenumber κ, while a system defined on a bounded domain has a discrete set of eigenvalues. Since the eigenvalue λ varies only slowly with changing wave number κ, this approximation will not influence the conditions for stability.

To solve the characteristic equation Equation 4.5, we employ the Lambert W function defined implicitly by the equation $z = W(z)\mathrm{e}^{W(z)}$ for $z \in \mathbb{C}$ (Corless et al., 1996) as follows. The characteristic equation (Equation 4.5) can be transformed to obtain

$$\begin{aligned}(1+\tau\lambda)\mathrm{e}^{\lambda d} &= c(k) \mid \cdot \frac{d}{\tau}\mathrm{e}^{\frac{d}{\tau}} \\ \left(d\lambda + \frac{d}{\tau}\right)\mathrm{e}^{d\lambda+\frac{d}{\tau}} &= c(k)\frac{d}{\tau}\mathrm{e}^{\frac{d}{\tau}} \\ d\lambda + \frac{d}{\tau} &= W\left(c(k)\frac{d}{\tau}\mathrm{e}^{\frac{d}{\tau}}\right),\end{aligned} \tag{4.9}$$

where in the last step the definition of the Lambert W function $z = W(z)\mathrm{e}^{W(z)}$ with $z \in \mathbb{C}$ was used. The Lambert W function has infinitely many branches, indexed by b, that are equivalent (upon rescaling as demonstrated in Equation 4.9) to the solutions of the characteristic equation Equation 4.5. The branch corresponding to the eigenvalue with the largest real part is called the principle branch ($b = 0$), see Eqs. 4.40–4.41 for a proof. To determine stability of the steady state u_0, we thus need to show whether the principle branch of the Lambert W function,

$$\lambda_b(k) = -\frac{1}{\tau} + \frac{1}{d}W_b\left(c(k)\frac{d}{\tau}\mathrm{e}^{\frac{d}{\tau}}\right). \tag{4.10}$$

has a negative real part.

4.2 Conditions for linearized stability in a single-population model

As discussed in the previous section, the homogeneous steady state u_0 is locally asymptotically stable if all eigenvalues λ_b have negative real parts.

$$\mathrm{Re}\left[W_b\left(c(k)\frac{d}{\tau}\mathrm{e}^{\frac{d}{\tau}}\right)\right] < \frac{d}{\tau}, \tag{4.11}$$

for all branches b of the Lambert W function. At the point where the real part of the eigenvalue λ_0 on the principle branch becomes positive, the system undergoes a bifurcation. Let us denote the wavenumber corresponding to the bifurcation point $k = k^*$, the maximum of c as $c_{\max}$ and the minimum as $\mathrm{c}_{\min}$ occurring at $k_{\max}$ and $k_{\min}$, respectively, as indicated in Figure 4.2(b) and (d). For $c_{\max} = 1$, the homogeneous steady state becomes unstable by definition of the Lambert W function,

$$W\left(\frac{d}{\tau}\mathrm{e}^{\frac{d}{\tau}}\right) = \frac{d}{\tau},$$

as equality in Equation 4.11 then holds for any $d > 0$ and $\tau > 0$. At this transition, the imaginary part of λ_0 is zero because the principal branch of the Lambert W function has real values for positive real arguments. If the instability occurs at a wavenumber $k^* = 0$, then the transitions corresponds to the transition between the asynchronous irregular (AI) state and the synchronous regular (SR) state without any spatial structure. If this transition appears at a wavenumber $k^* > 0$, it will give rise to spatial patterns (Equation 4.4).

For a negative argument of W of less than $-1/e$, a complex-conjugate pair of eigenvalues Equation 4.10 crosses the imaginary axis when the condition

$$\mathrm{Re}\left[W_0\left(c_{\min}\frac{d}{\tau}\mathrm{e}^{\frac{d}{\tau}}\right)\right] = \frac{d}{\tau} \tag{4.12}$$

is fulfilled with $c_{\min} < -1$, corresponding to a Hopf bifurcation of the temporal dynamics, giving rise to temporal oscillations. Equation 4.12 then, according to (Helias et al., 2013, Eq. 10), reduces to

$$\frac{d^{\mathrm{crit}}}{\tau} = \frac{\pi - \arctan\left(\sqrt{c_{\min}^{\mathrm{crit}^2} - 1}\right)}{\sqrt{c_{\min}^{\mathrm{crit}^2} - 1}}, \tag{4.13}$$

	homogeneous	spatial oscillations	temporal oscillations	wave trains
$c_{\max}$	< 1	1	< 1	< 1
$c_{\min}$	$> c_{\min}^{\text{crit}}$	$> c_{\min}^{\text{crit}}$	$c_{\min}^{\text{crit}}$	$c_{\min}^{\text{crit}}$
d	$< d^{\text{crit}}$	$< d^{\text{crit}}$	d^{crit}	d^{crit}
k^*	-	> 0	0	> 0

Table 4.1: Conditions for the onset of spatial and temporal oscillations, and wave trains. Gray cells in each column indicate the conditions required for the instability causing the bifurcation. White cells denote the conditions for the respective other bifurcation not to occur. Last row indicates whether the bifurcation happens for zero or nonzero wave number k^*. Here d^{crit} and $c_{\min}^{\text{crit}}$, as defined in Equation 4.13 and shown in Figure 4.2E, denote the critical delay and the minimum of the effective profile on the transition curve for a Hopf bifurcation.

where d^{crit} is the critical delay and $c_{\min}^{\text{crit}}$ a critical minimum of the effective profile for points on the transition curve. The system is stable for $c_{\min} > -1$ for all delays. For larger absolute values of $c_{\min}$, the bifurcation point is given by the critical value of the ratio between the time constant and the delay (Figure 4.2(e)). For transitions at $k^* = 0$, temporal oscillations emerge in which all neurons of the population oscillate in phase, corresponding to the transition from the AI regime to the 'synchronous irregular fast (SI fast)' (Brunel and Hakim, 1999). At transitions with $k^* > 0$, spatial and temporal oscillations give rise to so called 'wave trains' (Ermentrout, 1998, Section 8) or equivalently periodic travelling waves. If the homogeneous steady state becomes unstable due to $c_{\max} = 1$, the transition curve in Figure 4.2E also provides a lower bound $c_{\min}^{\text{crit}}(\tau/d^{\text{crit}})$ above which temporal oscillations do not occur prior to the transition due to $c_{\max}$. The analysis presented in this chapter does not distinguish between the super- and subcritical Hopf bifurcations, and therefore does not guarantee the existence of an asymptotically stable limit cycle. It was, however, observed in the corresponding network simulations presented in the subsequent chapters. Table 4.1 summarizes the (necessary) conditions for asymptotic stability, spatial and temporal oscillations and wave trains.

Finally, we observe that the absolute value of $\widehat{p}$ is strictly maximal at $k = 0$ (see Eqs. 4.42–4.43). For a purely excitatory population ($w > 0$) the critical minimum $c_{\min}^{\text{crit}}(\tau/d^{\text{crit}})$ cannot be reached while keeping the maximum $c_{\max}$ in the region of stability as $c_{\max} > |c_{\min}|$. For a purely inhibitory population ($w < 0$), the condition $k_{\min} > 0$ is not fulfilled because $c_{\min}$ occurs at $k = 0$ as $\widehat{p}$ has its global maximum at the origin. As a consequence, wave trains cannot occur in a system with only one neural population.

4.3 Conditions for linearized stability in a two-population model

In this section we derive conditions analogous to Table 4.1 for a model with an excitatory and an inhibitory population, assuming the boxcar spatial profile described in Section 4.1. The effective profile from Equation 4.7 then takes the form

$$c(k) = w_{\mathrm{E}} \frac{\sin(R_{\mathrm{E}}k)}{R_{\mathrm{E}}k} + w_{\mathrm{I}} \frac{\sin(R_{\mathrm{I}}k)}{R_{\mathrm{I}}k}. \tag{4.14}$$

Since the stability properties of the homogeneous steady state in the case of an excitatory-inhibitory model depend on the relative magnitudes of the minima and maxima of the effective profile (Equation 4.14), it is convenient to introduce the relative width $\rho \coloneqq R_{\mathrm{I}}/R_{\mathrm{E}} > 0$ and the relative weight $\eta \coloneqq -w_{\mathrm{I}}/w_{\mathrm{E}} > 0$. For the sake of simplicity, it is then possible to divide Equation 4.14 by w_{E}, rescale the wavenumber $\kappa = R_{\mathrm{E}}k$ and introduce the dimensionless effective profile

$$\tilde{c}(\kappa) = \frac{\sin(\kappa)}{\kappa} - \eta \frac{\sin(\rho\kappa)}{\rho\kappa}. \tag{4.15}$$

Figure 4.2(a)-(d) shows the different dynamical states together with the bifurcation diagrams (e)-(g) where the respective regions of the parameter space can be identified. The curves separating those regions are derived in detail in 4.9.5. Above the dashed transition curve $\eta_{t1}(\rho)$ given by Equation 4.50), the following inequality is satisfied, $\|\widetilde{c}_{\min}\| > \widetilde{c}_{\max}$ (regions 1 and 2), and holds with the opposite sign below the dashed curve (regions 3 and 4). The solid transition curve $\eta_{t2}(\rho)$ given by Equation 4.53) indicates whether the extreme value with the largest absolute value occurs at $k = 0$ (regions 2 and 3) or at $k > 0$ (regions 1 and 4). Hence, a wave train will occur when the effective profile has a minimum at $k^* \neq 0$ and a maximum lower than 1 (Table 4.1). It is necessary that $\rho < 1$, i.e. that the reach of excitation is wider than inhibition. Concretely, parameters of the model need to lie within the region 1 of Figure 4.2(f).

4.4 Validation in a network of nonlinear rate neurons

To validate the theoretically obtained results in a network simulation, we first consider a network of $N_{\mathrm{E}} = 4,000$ excitatory (E) and $N_{\mathrm{I}} = 1,000$ inhibitory (I) rate

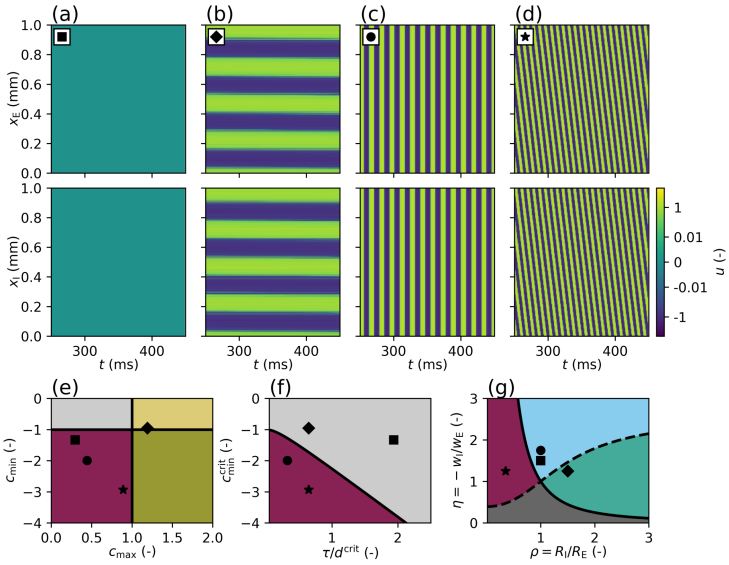

Figure 4.3: Predictions from linear stability analysis lead to spatiotemporal patterns in simulated network of nonlinear rate neurons. Different parameter combinations, selected according to stability conditions in Table 4.1, cause pattern formation in rate-neuron network with tanh gain function. (a)–(d) Color-coded activity per neuron over time. Neurons are shown at their position on the ring. (e)–(g) Phase diagrams showing conditions and parameter choices indicated by corresponding markers. Purple regions indicate the possibility for wave trains. (e) Color code indicates stability based on minimum c_{min} and maximum c_{max}. Gray: Both c_{min} and c_{max} stable. Dirty yellow: c_{max} unstable and c_{min} stable. Dirty green: c_{max} unstable and c_{min} undetermined. Purple: c_{max} stable and c_{min} undetermined. (a) Stable activity (square marker). (b) Spatial oscillations (diamond marker). (c) Temporal oscillations (circular marker). (d) Wave trains (star marker). Parameters: d, R_{E} and R_{I} as in Figure 4.1(a)–(d), $w_{\mathrm{E}} = 2.73$ in all panels. (a) $w_{\mathrm{I}} = -4.10$. (b) $w_{\mathrm{I}} = -3.42$. (c) $w_{\mathrm{I}} = -4.79$. (d) $w_{\mathrm{I}} = -3.42$. Reproduced from (Senk et al., 2020a).

neurons described by a discrete version of the neural-field equation Equation 4.2 (see Table 4.3 for details). The neurons are distributed on a ring with perimeter $L = 1\,\mathrm{mm}$ as described in 4.9.9. Every neuron receives K_X incoming connections per source population $X \in \{\mathrm{E}, \mathrm{I}\}$. Connections are selected according to the boxcar-shaped spatial profile, i.e. uniformly distributed with within an interval of width R_X. In order to give p the interpretation of connection probability, we normalized the weights by the in-degree, $w'_X = w_X/K_X$. The parameters τ and d are chosen as in the neural-field model.

The behaviour of the simulated system agrees well with the theoretical predictions In Figure 4.3(a), the homogeneous steady state is stable. Its parameter values, indicated by a square marker in Figure 4.3(e)-(g), satisfy $c_{\max} < 1$ (Figure 4.3(e)) and the delay is small enough to ensure stability.

In Figure 4.3(b), the homogeneous steady state loses stability due to $c_{\max} > 1$, as indicated by the diamond marker in Figure 4.3(e). Since the Hopf bifurcation curve in Figure 4.3(f) was not crossed and $k_{\max} > 0$ (Figure 4.3(g)), this parameter combination satisfies the conditions for a stationary spatial pattern. Indeed, we observed spatial oscillations in the network simulation with 4 cycles across the spatial domain, matching the theoretical prediction of $L \cdot k_{\max}/(2\pi) \approx 3.74\,\mathrm{mm}^{-1}$.

Figure 4.3(c) shows a network state with temporal oscillations. The corresponding parameter combination, indicated by the circular marker, falls into the region with $c_{\max} < 1$ and $c_{\min} < -1$ (Figure 4.3(e)). The delay was chosen on the left from the Hopf bifurcation curve in Figure 4.3(f). As indicated in Figure 4.3(g), the state will be spatially homogeneous due to $k_{\min} = 0$. The theoretical prediction of the temporal frequency of $\mathrm{Im}[\lambda_{\min}]/(2\pi) \approx 66.68\,\mathrm{Hz}$ well agrees with the outcome of the simulation.

Figure 4.3(d) shows the last dynamical state – the wave trains denoted by a star. In this case, the homogeneous steady state lost stability due to $c_{\min} < c_{\min}^{\mathrm{crit}}$ (Figure 4.3(f)) with $k_{\min} > 0$ (Figure 4.3(g)), while $c_{\max}$ remains in the region of stability (Figure 4.3(e)). The propagation speed of the wave train can again by theoretically predicted, $\mathrm{Im}[\lambda_{\min}]/(k_{\min}) \approx 0.04\,\mathrm{mm/ms}$, with the temporal frequency $\mathrm{Im}[\lambda_{\min}]/(2\pi) \approx 121.01\,\mathrm{Hz}$ and the spatial frequency $k_{\min}/(2\pi) \approx 3.02\,\mathrm{mm}^{-1}$. Also in the case of wave trains we observed a good agreement with the theoretically predicted behaviour and the outcome of the network simulation.

4.5 Conditions for linearized stability in the spiking network model

In order to create a link between the linearized dynamics of the neural-field model and the simulated network of leaky-integrate-and-fire (LIF) neurons, we need to derive a linear mean-field model that describes the population dynamics of the LIF network. To that end, we linearize the system defining the dynamics of a LIF neuron with exponentially decaying synaptic currents,

$$\begin{aligned} \tau_{\mathrm{m}} \frac{\mathrm{d}V_i}{\mathrm{d}t} &= -V_i + I_i(t), \\ \tau_{\mathrm{s}} \frac{\mathrm{d}I_i}{\mathrm{d}t} &= -I_i + \tau_{\mathrm{m}} \sum_j J_{ij} s_j(t-d), \end{aligned} \tag{4.16}$$

with the membrane potential V_i and the synaptic current I_i. We adopt the convention of (Fourcaud-Trocmé and Brunel, 2005) and formulate the system in terms of rescaled quantities, as explained in Equation 4.59. We assume that the synaptic time constant τ_{s} is much smaller than the membrane time constant $\tau_{\mathrm{m}} = R_{\mathrm{m}} C_{\mathrm{m}}$, with the membrane resistance R_{m} and membrane capacitance C_{m}. A spike train of neuron j is given by the equation $s_j(t) = \sum_k \delta\left(t - t_k^j\right)$, J_{ij} is the strength of the synapse from neuron j to neuron i and d the transmission delay. A spike is emitted whenever the membrane potential V_i reaches the threshold V_θ and the membrane potential is then reset to the resting potential V_{r}, where is stays for the refractory period τ_{ref}.

Next, we approximate the firing of each neuron by a Poisson process (Brunel and Hakim, 1999, Section 3.5), assume that spike trains of different neurons are not correlated and the amplitudes of post-synaptic potentials small. A second-order expansion as in (Ricciardi et al., 1999; Risken, 1996) yields the expressions for the first and second order moments

$$\begin{aligned} \mu_i(t) &= \tau_{\mathrm{m}} \sum_j J_{ij}\, \nu_j(t-d), \\ \sigma_i^2(t) &= \tau_{\mathrm{m}} \sum_j J_{ij}^2\, \nu_j(t-d). \end{aligned} \tag{4.17}$$

Under the assumption that neurons are uniformly distributed on the ring domain with density ρ_x, we consider a continuum limit such that an element of volume $\mathrm{d}x$ contains $\rho_x \mathrm{d}x$ neurons. The probability of a neuron at a position y being connected

to a neuron at a position x is given by the same probability density function $\widetilde{p}(x-y)$ for any two positions x, y, independently between different pairs of points. Then the moments from Equation 4.17 can be rewritten as

$$\begin{aligned}\mu(x,t) &= \tau_{\mathrm{m}} J \int_{-\infty}^{\infty} \widetilde{p}(x-y)\,\nu(y,t-d)\,\rho_x \mathrm{d}y,\\ \sigma^2(x,t) &= \tau_{\mathrm{m}} J^2 \int_{-\infty}^{\infty} \widetilde{p}(x-y)\,\nu(y,t-d)\,\rho_x \mathrm{d}y.\end{aligned} \tag{4.18}$$

For the sake of convenience, we rescale the density function

$$p(x-y) = \frac{\widetilde{p}(x-y)}{\int \widetilde{p}(x')\,\mathrm{d}x'}, \tag{4.19}$$

and denote the in-degree (the number of incoming connections to a neuron)

$$K := \int \widetilde{p}(x')\,\rho_x\,\mathrm{d}x'. \tag{4.20}$$

Let us denote the firing rate of a LIF neuron at position x at time t by

$$\nu(x,t) = F[\mu(x,\circ),\,\sigma(x,\circ)](t) \tag{4.21}$$

and assume that it is driven by a white noise with mean $\mu(x,t)$ and variance $\sigma^2(x,t)$. Then $[\mu(\circ),\sigma(\circ))](t) := \langle \delta(t-t_k)\rangle_\xi$, where t_k are the time-points of the threshold crossings of Equation 4.16 and ξ denotes realizations of the white noise with moments Equation 4.18. By plugging Equation 4.18 into Equation 4.21, we obtain the evolution equation

$$\nu(x,t) = F\left[\tau_{\mathrm{m}} JK \int_{-\infty}^{\infty} p(x-y)\,D_d\,\nu(y)\,\mathrm{d}y,\ \tau_{\mathrm{m}} J^2 K \int_{-\infty}^{\infty} p(x-y)\,D_d\,\nu(y)\,\mathrm{d}y\right](t), \tag{4.22}$$

where the delay operator D_d is defined as $[D_d\nu(x)](t) = \nu(x,t-d)$. In order to perform linearized stability analysis, we consider ν of the form

$$\nu(x,t) = \nu_0 + \delta\nu(x,t), \qquad \delta\nu \ll \nu_0. \tag{4.23}$$

and by a Taylor expansion obtain

$$\nu_0 + \delta\nu(x,t) = F\Big[\mu_0, \sigma_0^2\Big] + \int_{-\infty}^{\infty} p(x-y) \int_{-\infty}^{t} h_\nu(\mu_0, \sigma_0, t-s)\, \delta\nu(y, s-d)\, \mathrm{d}s\, \mathrm{d}y + \mathcal{O}\Big(\delta\nu^2\Big),$$

with

$$h_\nu(\mu_0, \sigma_0, t-s) = \tau_\mathrm{m} JK\, \frac{\delta F[\mu_0, \sigma_0^2](t)}{\delta\mu(s)} + \tau_\mathrm{m} J^2 K\, \frac{\delta F[\mu_0, \sigma_0^2](t)}{\delta\sigma^2(s)}, \tag{4.24}$$

where $\mu_0 = \tau_\mathrm{m} JK\nu_0$ and $\sigma_0^2 = \tau_\mathrm{m} J^2 K\nu_0$ and the first terms on both sides cancel due to $\nu_0 = F[\mu_0, \sigma_0^2]$. The stationary firing rate ν_0 in the limit of short synaptic time constants ($\tau_\mathrm{s} \ll \tau_\mathrm{m}$) can be determined self-consistently from this condition (Fourcaud and Brunel, 2002; Helias et al., 2013, Eq. A.1),

$$\begin{aligned} \nu_0^{-1} &= \tau_\mathrm{r} + \tau_\mathrm{m}\sqrt{\pi}(F(y_\theta) - F(y_\mathrm{r})) \\ f(y) &= \mathrm{e}^{y^2}(1 + \mathrm{erf}(y)), \qquad F(y) = \int^y f(y)dy \\ \text{with} \quad y_{\{\theta,r\}} &= \frac{V_{\{\theta,r\}} - \mu}{\sigma} + \frac{\beta}{2}\sqrt{\frac{\tau_\mathrm{s}}{\tau_\mathrm{m}}}, \qquad \beta = \sqrt{2}\left|\zeta\left(\frac{1}{2}\right)\right|, \end{aligned} \tag{4.25}$$

where ζ denotes the Riemann's zeta function (Abramowitz and Stegun, 1974). We denote the functional derivatives by

$$\begin{aligned} h_\mu(t-s) &\equiv \frac{\delta F[\mu_0, \sigma_0^2](t)}{\delta\mu(s)}, \\ h_{\sigma^2}(t-s) &\equiv \frac{\delta F[\mu_0, \sigma_0^2](t)}{\delta\sigma^2(s)}, \end{aligned} \tag{4.26}$$

These function can be expressed analytically (Eqs. 4.55–4.56) under first order approximation in $\mathcal{O}(\sqrt{\tau_s/\tau_m})$ (Schuecker et al., 2015) and are therefore valid for sufficiently short synaptic time constants. The resulting convolution equation describing the linearized dynamics in the vicinity of the stationary state reads

$$\delta\nu(x,t) = \int_{-\infty}^{\infty} p(x-y) \int_{-\infty}^{t} h_\nu(t-s)\, \delta\nu(y, s-d)\, \mathrm{d}y\, \mathrm{d}s, \tag{4.27}$$

and can be directly compared to the neural-field model presented in Section 4.1.

For the subsequent analysis we assume that the contribution of the term h_{σ^2} is negligible.

4.6 Parameter mapping between the models

To create a link between the linearized systems of the neural-field model and the spiking model, we express the deviations from the steady state,

$$\delta o(x,t) = \begin{cases} \delta u(x,t) & \text{neural field} \\ \delta \nu(x,t) & \text{spiking} \end{cases} \tag{4.28}$$

as a convolution equation

$$\begin{aligned} \delta o(x,t) &= [h * \delta i](x,t) \\ \delta i(x,t) &= \int_{-\infty}^{\infty} p(x-y)\, \delta o(y, t-d)\, \mathrm{d}y, \end{aligned} \tag{4.29}$$

where the two models only differ in the convolution kernel,

$$h(t) := \begin{cases} h^{\mathrm{nf}}(t) := \Theta(t)\, \frac{w}{\tau}\, \mathrm{e}^{-\frac{t}{\tau}} & \text{neural field} \\ h^{\mathrm{s}}(t) := \tau_{\mathrm{m}} JK\, h_\mu(t) & \text{spiking.} \end{cases} \tag{4.30}$$

Then also the characteristic equations for both systems can be derived simultaneously by plugging in the ansatz $\delta o(x,t) = \mathrm{e}^{\mathrm{i}kx}\mathrm{e}^{\lambda t}$ and take the form

$$H(\lambda) \cdot \mathrm{e}^{-\lambda d} \cdot \widehat{p}(k) = 1. \tag{4.31}$$

The effective transfer function H can be obtained as a Laplace transform of Equation 4.30 and in the case of a neural field model read

$$H^{\mathrm{nf}}(\lambda) = \frac{1}{1+\lambda\tau} w. \tag{4.32}$$

The effective transfer function for the spiking model is given by Equations 4.55–4.56.

Despite having the same form, the characteristic equations of the two models specified by Equation 4.31 with the respective transfer functions H may produce qualitatively different sets of eigenvalues. To show that this is not the case, we follow (Brunel et al., 2001; Lindner and Schimansky-Geier, 2001; Brunel et al., 2001; Helias et al., 2013) and approximate the transfer function corresponding to the spiking model by a low-pass filter with effective parameters H_0 and τ,

$$H_\mu(\lambda) \approx H_{\mathrm{LP}}(\lambda) = \frac{H_0}{1+\lambda\tau}, \tag{4.33}$$

where H_μ is the Fourier transform of h_μ defined in Equation 4.26 and the effective parameters H_0 and τ can be obtained numerically. This approximation creates a mapping between the phenomenological parameters w and τ of the neural field model and the lower-level parameters of the spiking model,

$$w = H_0 \tau_\mathrm{m} J K, \tag{4.34}$$

which follows from the fact that $\int h_\mu(t) = H_\mu(0) \approx H_0$.

4.7 Validation in a network of leaky-integrate and fire neurons

To practically test our results, we simulate a network of LIF neurons with parameters corresponding to those of the rate network presented earlier (Figure 4.3) via the parameter mapping from Section 4.6. This results in a connectivity matrix

$$M(r) = \tau_m J_\mathrm{E} K_\mathrm{E} \begin{pmatrix} p_\mathrm{E}(r) & -\gamma g\, p_\mathrm{I}(r) \\ p_\mathrm{E}(r) & -\gamma g\, p_\mathrm{I}(r) \end{pmatrix}. \tag{4.35}$$

with the relative in-degree $\gamma = K_\mathrm{I}/K_\mathrm{E}$ and the relative synaptic strength $g = -J_\mathrm{I}/J_\mathrm{E}$. The stability of the stationary state is again determined by the relative magnitudes of the minimum and the maximum of the effective profile $c(k)$ (Equation 4.14), this time with $w_\mathrm{E} = H_0 \tau_\mathrm{m} J_\mathrm{E} K_\mathrm{E}$ and $w_\mathrm{I} = -H_0 \tau_\mathrm{m} g J_\mathrm{E} \gamma K_\mathrm{E}$ (Equation 4.34). The critical delay can also be derived from Equation 4.13.

Figure 4.4 illustrates different types of bifurcations in the spiking network. Figure 4.4(a) shows a transition from a stable (so called asynchronous irregular) state to a spatial oscillation caused by an amplitude increase of the excitatory postsynaptic current $J_\mathrm{E}^{'}$, where $J^{'} = C_\mathrm{m} J/\tau_s$ (see Equation 4.59 for an explanation of the rescaling). The working point was kept fixed via increasing the amplitude of the external Poisson drive. An increasing synaptic delay d may either lead to a transition to temporal oscillation (Figure 4.4(b)) if instability occurs at $k = 0$, or to a wave train (Figure 4.4(c)) for $k > 0$. The gradual shift across a wave train with a higher spatial frequency to a wave train with a lower spatial frequency is caused by the competing minimum and maximum of the effective profile, c_max and c_min. Panels (d)-(f) show the respective states in different projections of the parameter space, with arrows indicating an increase of the bifurcation parameter. Some markers in panels (d) and (f) have fixed positions because they have no impact on the effective spatial profile.

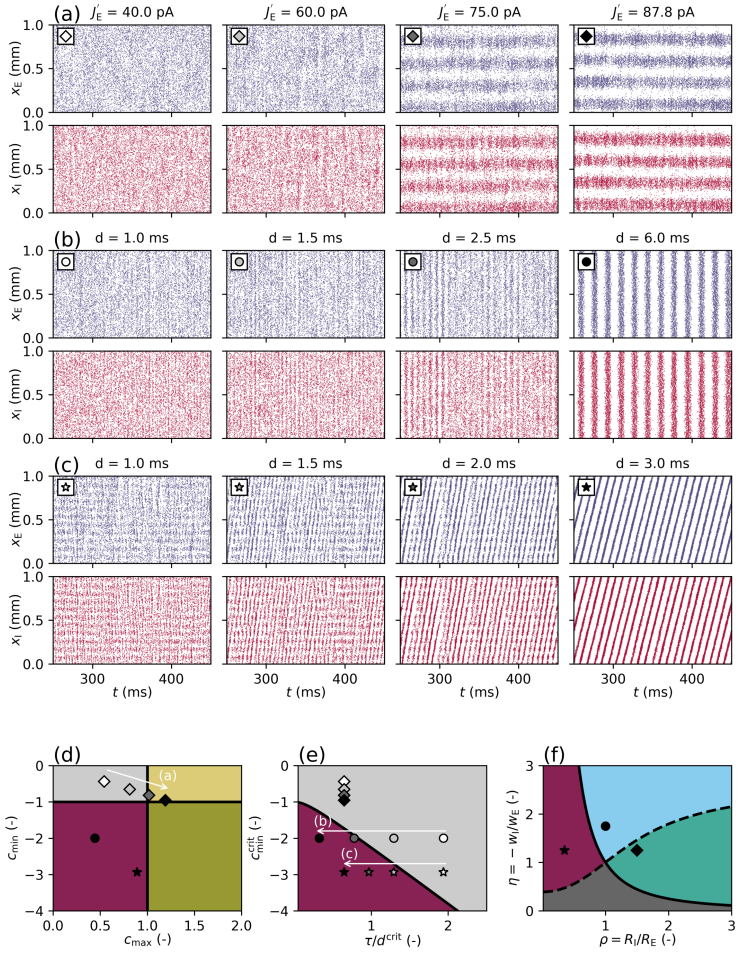

Figure 4.4: Transitions from theoretically stable states to spatiotemporal patterns in spiking network simulation. (a)–(c) Spike rasters showing transition to network states in Figure 4.1(b)–(d) (same markers, same parameter combinations). The changed parameter value is given on top of each raster plot. (a) Increasing recurrent weight $J_E^{'}$ leads to onset of spatial oscillations. (b) Increasing synaptic delay d leads to onset of temporal oscillations at $k = 0$. (c) Increasing delay d leads to onset of temporal oscillations at $k > 0$, i.e., wave trains. (d)–(e) Gray shaded markers and white arrows labeled according to respective panel (a)-(c) in phase diagrams indicate sequences of parameter combinations and breakdown of stability at $c_{max} = 1$ or at $c_{min} = c_{min}^{crit}$. For each sequence in panels (a)–(c), delay d, excitatory profile width R_E, inhibitory profile width R_I, and the relative synaptic strength g correspond to the values given in Figure 4.1(b)–(d) with corresponding markers. Reproduced from (Senk et al., 2020a).

4.8 Discussion

In this chapter we presented a method that can be used to transfer knowledge about pattern formation in high-level neural field models to a simulation of a spiking neural network and vice versa. Such a link between models at different levels of description is important for testing generality of results and for understanding the mechanisms that underlie them.

Moreover, we derived conditions for the emergence of wave trains in both models. Using linear stability analysis, we found regions in the parameter space where the dynamical systems converge to solutions of the same topological nature: a stationary state (in the context of neural networks corresponding to an asynchronous irregular regime), temporal oscillations, spatial oscillations or wave trains (periodic travelling waves) of activity. The propagation speed of the waves trains in the example model (0.04 mm/ms) was comparable to experimentally observed speeds on the mesoscopic scale (Girard et al., 2001; Muller et al., 2018). Our analysis also showed that, under the assumptions of the model, the emergence of wave trains requires a two-population model and broader excitation than inhibition, observed for instance in the primary auditory cortex (Sun et al., 2013). The resulting criteria for parameters of the dynamical system, particularly the delay and the characteristics of the effective spatial connectivity profile, can be applied both in the neural field model and the spiking neural network thanks to the established mapping.

The presented mapping between two models of neural activity at different levels of description facilitates transfer of knowledge between two subfields of computational neuroscience: neural field models, extensively studied by mathematically inclined neuroscientists, and simulations of spiking networks, used more often to reproduce results of concrete electrophysiological experiments. In particular, the framework offers a dimensionality reduction that can assist mathematical analysis of network models on one hand, and data integration into high-level mathematical models on the other. The analysis presented in this chapter could be extended in several ways, e.g. to a two-dimensional spatial domain, spatial profiles with different shapes or a distance-dependent delay representing the axonal delay. Extensions to other neuron models are possible, provided the transfer function resembles a first-order low-pass filter, such as the exponential leaky-integrate-and-fire neuron (Fermani and Richardson, 2015), leaky-integrate-and-fire neurons with alpha-shaped synaptic currents (Nordlie et al., 2010) or models with conductance-based synapses (Heiberg et al., 2013).

Neural field models are often defined using the effective spatial profile as a starting point (Hutt et al., 2003; Atay and Hutt, 2005; Coombes, 2005; Roxin et al., 2005). Typical examples of such effective spatial profiles are the Mexican hat or the inverse Mexican hat connectivity. Due to not separating the excitatory and inhibitory populations explicitly, certain biological features such as the Dale's law (Eccles et al., 1954) cannot be accounted for and the underlying assumptions on the corresponding neural network are not apparent. As an example, several neural field models describing a single homogeneous population defined using the effective spatial profile produce wave trains (Roxin et al., 2005; Atay and Hutt, 2006; Venkov et al., 2007). We have shown in this chapter that wave-train generation in a model with only one neural population requires the synaptic weight to depend on distance.

Neural activity, whether spontaneous or evoked, typically varies over time and changes on a faster time scale than anatomical connectivity. It is therefore important for biological relevance of our results that wave trains can emerge without any changes in the network structure. This property is achieved due to the dependence of the transfer function on the working point, particularly on the mean and the variance of its input. Hence, changes in the network activity, e.g. due to external input, may bring the network to a different dynamical regime and potentially give rise to wave trains or other spatio-temporal patterns. Furthermore, spatially localized external input may act as a gating mechanism controlling the spatial spread of the waves.

4.9 Methods

In this section we collect detailed calculations that were omitted in the main text for brevity.

4.9.1 Derivation of the characteristic equation

The characteristic equation in Equation 4.5 is derived by linearizing Equation 4.2 and plugging in the ansatz $\delta u(x,t) = e^{\mathrm{i}kx}\mathrm{e}^{\lambda t}$. Then

$$\begin{aligned}
\tau\lambda\,\mathrm{e}^{ikx}\mathrm{e}^{\lambda t} &= -\mathrm{e}^{ikx}\mathrm{e}^{\lambda t} + \int_{-\infty}^{\infty} wp(x-y)\mathrm{e}^{iky}\mathrm{e}^{\lambda(t-d)}\,\mathrm{d}y \\
\tau\lambda &= -1 + w\mathrm{e}^{-\lambda d}\int_{-\infty}^{\infty} p(x-y)\mathrm{e}^{-ik(x-y)}\,\mathrm{d}y \\
&= -1 - w\mathrm{e}^{-\lambda d}\int_{\infty}^{-\infty} p(r)\mathrm{e}^{-ikr}\,\mathrm{d}r, \qquad r = x-y \\
&= -1 + w\mathrm{e}^{-\lambda d}\underbrace{\int_{-\infty}^{\infty} p(r)\mathrm{e}^{-ikr}\,\mathrm{d}r}_{\equiv\widehat{p}(k)},
\end{aligned} \tag{4.36}$$

where $\widehat{p}$ is the Fourier transform of the spatial profile p.

4.9.2 Effective connectivity profile for a two-population model

In the case of a two-population model, the characteristic equation is derived analogously to the one population case. The ansatz $\delta u(x,t) = v\mathrm{e}^{\mathrm{i}kx}\mathrm{e}^{\lambda t}$, with v denoting a vector, leads to

$$c(k)\,v = \widehat{M}(k)\,v, \tag{4.37}$$

with an eigenvalue c and an auxiliary matrix $\widehat{M}$ derived from the connectivity matrix M by the Fourier transform,

$$\widehat{M}(k) = \begin{pmatrix} w_{\mathrm{EE}}\,\widehat{p}_{\mathrm{EE}}(k) & w_{\mathrm{EI}}\,\widehat{p}_{\mathrm{EI}}(k) \\ w_{\mathrm{IE}}\,\widehat{p}_{\mathrm{IE}}(k) & w_{\mathrm{II}}\,\widehat{p}_{\mathrm{II}}(k) \end{pmatrix}. \tag{4.38}$$

There exists a non-trivial solution v of Equation 4.37 if and only if

$$\det\Big(\widehat{M}(k) - c(k)\mathbb{I}\Big) = 0.$$

The resulting eigenvalues $c_{1,2}$, given by Equation 4.7, define the effective profile in the characteristic equation in Equation 4.5.

4.9.3 The principle branch of Lambert W function determines stability

To be able to practically use the Lambert W function to determine stability of the stationary state, one has to show that the eigenvalue with the largest real part is given by its particular branch. The function $x(W) = W\,\mathrm{e}^W$ has a minimum at $W = -1$, no real solution for $x < -\mathrm{e}^{-1}$, one real solution for $x > 0$, and two solutions for $x \in [-e^{-1}, 0)$. The branch defined on the interval $[-e^{-1}, \infty)$ is called the principle branch (for negative arguments the largest solution is considered). The definition of the principle branch is then extended to the real line by the maximal real part and positive imaginary part of the complex eigenvalues on $(-\infty, -e^{-1})$.

Here we show that the branch of the Lambert W function with the largest real part is the principal branch. Assuming $x \in \mathbb{R}$, we write $W(x) = |W(x)|\mathrm{e}^{i\varphi} = \alpha + i\beta$ and

$$W(x)\mathrm{e}^{W(x)} = |W(x)|\,\mathrm{e}^{\alpha}\,\mathrm{e}^{i(\varphi+\beta)} = x \in \mathbb{R} \tag{4.39}$$

$$\rightarrow \mathrm{e}^{i(\varphi+\beta)} = \pm 1, \tag{4.40}$$

where $\varphi \in [-\pi, \pi]$ is the principal value. The branches are indexed by $q \in \mathbb{Z}$ according to the number of half-cycles of the exponential in Equation 4.40: $\varphi + \beta = q \cdot \pi$. The branch number can be written as $b = \lfloor \frac{q}{2} \rfloor$ with the floor function $\lfloor \cdot \rfloor$. Then the principle branch has the index $q = 0$ for $x \geq 0$ and $q = 1$ for $x < 0$.

Taking the absolute square of Equation 4.39, we obtain

$$x^2\,\mathrm{e}^{-2\alpha} = \alpha^2 + \beta^2. \tag{4.41}$$

Without loss of generality, we assume $\beta \geq 0$; this assumption holds for the real solutions with $\beta = 0$ and for one of the complex solutions. Complex solutions come in conjugate pairs due to the symmetry $(\varphi, \beta) \rightarrow (-\varphi, -\beta)$ and we consider the one with positive imaginary part $\beta > 0$, as only the real part determines the stability properties.

To prove that the real part α of W is maximal for $b = 0$, we first show that α is a decreasing function of β along the solutions of Equation 4.39. The left hand-side of

Equation 4.41 is a decaying function of α with the intercept x^2. The right hand-side is a parabola with the offset β^2. For $x \in (-\infty, -e^{-1}) \cup [0, \infty)$, an intersection can be attained either at a positive real part $\alpha \geq 0$ if $x^2 \geq \beta^2$, or at a negative real part $\alpha < 0$ if $x^2 < \beta^2$. If we increase β, the parabola defined by the right hand-side moves the up and the intersection to the left, meaning that α decreases with increasing β.

For $x \in [-e^{-1}, 0)$, either $\beta = 0$ or $\beta > 0$, but in both cases the solutions have negative real parts $\alpha < 0$. There are in total three intersections: two correspond to the real solutions ($q = \pm 1$) and the third intersection is created by taking the square of Equation 4.41, but does not solve Equation 4.39. The intersection with a larger real part corresponds to the principal branch ($q = 1$). Moreover, the complex solutions are indexed by odd numbers q with $|q| > 1$. Taking into account the interval where φ is defined, the imaginary part is bounded from below such that $\beta \geq 2\pi$ for non-principal branches. Analogically, there exists only one intersection between the exponential function and the parabola for large values of β for which α decreases with increasing β.

In summary, the eigenvalues with the maximal real part are determined by the principle branch of the Lambert W function.

4.9.4 Properties of the spatial profile

The spatial profile p is defined as a symmetric probability density function. Then it follows that its Fourier transform $\widehat{p}$ is real valued and even, $\widehat{p} \in (-1, 1]$ and $\widehat{p}$ attains 1 only at the origin:

- $|\widehat{p}(k)| \leq 1$ for all $k \in \mathbb{R}$:

$$\begin{aligned} |\widehat{p}(k)| &= \left| \int_{-\infty}^{\infty} p(r) \mathrm{e}^{-ikr} \, \mathrm{d}r \right| \leq \int_{-\infty}^{\infty} \left| p(r) \mathrm{e}^{-ikr} \right| \mathrm{d}r \\ &= \int_{-\infty}^{\infty} p(r) \, \mathrm{d}r = 1 \quad \text{for all } k \in \mathbb{R}, \end{aligned} \tag{4.42}$$

- $|\widehat{p}(k)| < 1$ for all $k \neq 0$:

$$\begin{aligned} \left| \int_{-\infty}^{\infty} p(r) \mathrm{e}^{-ikr} \mathrm{d}r \right| &\leq \int_{-\infty}^{\infty} p(r) |\cos(kr)| \, \mathrm{d}r \\ &< \int_{-\infty}^{\infty} p(r) \, \mathrm{d}r = 1 \quad \text{for all } k \neq 0, \end{aligned} \tag{4.43}$$

because $|\cos(kr)| < 1$ almost everywhere (except for a set of measure zero in r if $k \neq 0$) which has no effect on the value of the integral.

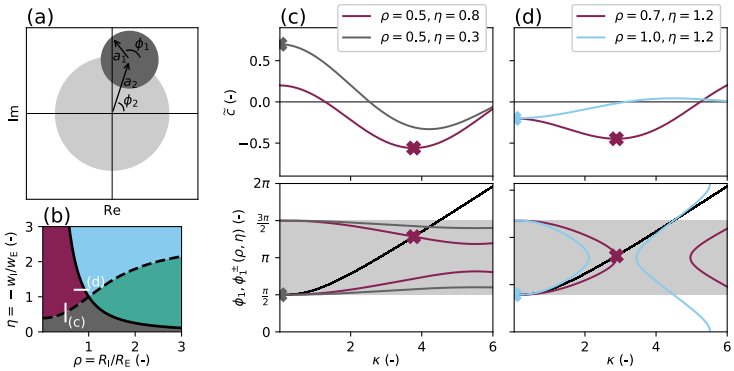

Figure 4.5: Graphical analysis for extrema of reduced profile for derivation of transition curves. (a) The condition for the extremum (Equation 4.45) amounts to the addition of two vectors in the complex plane whose sum is purely imaginary. The vectors have lengths a_1 and a_2 and angles ϕ_1 and ϕ_2, defined in Equation 4.46. (b) Diagram of Figure 4.2(f) with indicated parameter combinations (ρ, η) as used in panels (c) and (d). (c)–(d) Reduced profile $\widetilde{c}$ (top) and ϕ_1 and $\phi_1^{\pm}$ from Equation 4.47 vs. κ (bottom) for two different combinations of (ρ, η) with line colors corresponding to regions in panel (b). (c) $|\widetilde{c}_{\min}| > \widetilde{c}_{\max}$ in purple and vice versa in dark gray. (d) $\widetilde{c}_{\min}$ at $\kappa = 0$ in light blue and at $\kappa > 0$ in purple. Reproduced from (Senk et al., 2020a).

4.9.5 Bifurcation diagram for the reduced spatial profile

Using a graphical approach, we derive the transition curves from the bifurcation diagram in Figure 4.2(f). Equation 4.15 for the reduced profile $\widetilde{c}(\kappa)$ at κ^* yields

$$\tfrac{\partial}{\partial\kappa}\widetilde{c}(\kappa)|_{\kappa^*} \quad = \quad 0. \ ,$$

where the derivative can be written as

$$\frac{\partial}{\partial\kappa}\widetilde{c}(\kappa) = \frac{\cos(\kappa)}{\kappa} - \frac{\sin(\kappa)}{\kappa^2} - \eta\frac{\cos(\rho\kappa)}{\kappa} + \eta\frac{\sin(\rho\kappa)}{\rho\kappa^2}. \tag{4.44}$$

Hence, we obtain

$$\begin{aligned} 0 &= \mathrm{Re}\Big[(\kappa+i)\mathrm{e}^{i\kappa} - \frac{\eta}{r}(\rho\kappa+i)\mathrm{e}^{i\rho\kappa}\Big] \\ &= \mathrm{Re}\Big[a_1\mathrm{e}^{i\phi_1} + a_2\mathrm{e}^{i\phi_2}\Big] \\ &= a_1\cos(\phi_1) + a_2\cos(\phi_2), \end{aligned} \tag{4.45}$$

where a_1 and a_2 are the absolute values of the complex numbers and ϕ_1 and ϕ_2 their phases, given by

$$\begin{aligned} a_1(\kappa) &= \sqrt{1+\kappa^2}, \\ \phi_1(\kappa) &= \kappa + \frac{\pi}{2} - \arctan(\kappa), \\ a_2(\kappa;\rho,\gamma) &= \frac{\eta}{\rho}\sqrt{1+\rho^2\kappa^2}, \\ \phi_2(\kappa;\rho) &= \rho\kappa + \frac{3\pi}{2} - \arctan(\rho\kappa). \end{aligned} \tag{4.46}$$

Figure 4.5(a) shows an example solution for the case $a_1 < a_2$ in the complex plane. As illustrated in Figure 4.5(a), we express ϕ_1 as

$$\phi_1^{\pm} = \pi \pm \arccos\Big(\frac{a_2}{a_1}\cos(\phi_2)\Big). \tag{4.47}$$

The extrema are then determined by the intersections of $\phi_1^{\pm}$ with $\kappa+\pi/2-\arctan(\kappa)$ (see Equation 4.46) and ϕ_2 is determined from Equation 4.45.

The calculation is illustrated in Figure 4.5(a). Figure 4.5(b) essentially reproduces Figure 4.2(f), with the white bars connecting points given by parameter combinations (ρ,η) on both sides of the transition curves, and the parameters are specified in panels (c) and (d). The first transition curve $\eta_{t1}(\rho)$ (dashed line in Figure

4.5(b)) is given by $\widetilde{c}_{\max}(\kappa_{\max}) = |\widetilde{c}_{\min}(\kappa_{\min})|$. In other words, the first transition curve is determined by such a combination (ρ, η) for which the absolute values of the positive and the negative extremum of the profile coincide. The top panel of Figure 4.5(c) compares two reduced profiles with a fixed ρ and two values of η (the cross indicates the maximum absolute value of the profile). At the transition either $\kappa_{\max}$ or $\kappa_{\min}$ vanishes. From Equation 4.15 we then deduce $|\widetilde{c}(\kappa_0)| = |\widetilde{c}(\kappa_1)| = |1-\eta|$. From the condition $\frac{\partial}{\partial\kappa}\widetilde{c}(\kappa)|_{\kappa_1} = 0$ and Equation 4.44 we obtain two equations for $\kappa = \kappa_1$:

$$\begin{aligned} 1-\eta &= \frac{\sin(\kappa)}{\kappa} - \eta\frac{\sin(\rho\kappa)}{\rho\kappa} \\ 1-\eta &= \cos(\kappa) - \eta\cos(\rho\kappa). \end{aligned} \tag{4.48}$$

Consequently,

$$\frac{1}{\kappa}\sin(\kappa)[1+\cos(\rho\kappa)] - \frac{1}{\rho\kappa}\sin(\rho\kappa)[1+\cos(\kappa)] + \cos(\rho\kappa) - \cos(\kappa) = 0, \tag{4.49}$$

which defines $\kappa(\rho)$ for each fixed ρ. The bottom panel of Figure 4.5(c) shows ϕ_1 from Equation 4.46 as a black line and $\phi_1^{\pm}$ from Equation 4.47 for the parameters of the two effective profiles. This results in an interval for κ in which Equation 4.49 is solved at an extreme value of the profile, $\kappa \in (0,\, 4.49341)$, with the lower limit corresponding to $\phi_1 = \frac{\pi}{2}$ and the upper limit to $\phi_1 = \frac{3\pi}{2}$. The transition curve is then given by

$$\eta_{t1}(\rho) = \frac{1+\cos(\kappa(\rho))}{1+\cos(\rho\kappa(\rho))}, \tag{4.50}$$

where $\kappa(\rho)$ is determined by Equation 4.49.

The solid transition curve $\eta_{t2}(\rho)$ in Figure 4.5(b) separates the region in the parameter space where the extremum with the largest absolute value is attained at $\kappa = 0$ and $\kappa > 0$. In Figure 4.5(d) the profiles for two different values of ρ and fixed η are shown. The bottom panel of Figure 4.5(d) indicates that this transition occurs when ϕ_1^- at $\kappa \gtrsim 0$ crosses ϕ_1 (black) from above (light blue) to below (purple).

In the neighbourhood of the bifurcation, ϕ_1 as a function of κ can be expanded,

$$\phi_1(\kappa) \approx \frac{\pi}{2} + \frac{\kappa^3}{3} + \mathcal{O}\Big(\kappa^5\Big) \tag{4.51}$$

$$\phi_1^-(\kappa;\rho,\eta) \approx \frac{\pi}{2} + \frac{\eta\rho\kappa^3}{3} + \mathcal{O}\Big((\rho\kappa)^5\Big). \tag{4.52}$$

By comparing the coefficients of the third-order polynomials we obtain the transition curve

$$\eta_{t2}(\rho) = \frac{1}{\rho^2}. \tag{4.53}$$

4.9.6 The transfer function of the spiking model

The linearization of the spiking model requires a transfer function H_μ that describes the linear response of the firing rate $\delta\nu(\omega)$ to changes in the input statistics, particularly the mean $\delta\mu(\omega)$,

$$\delta\nu(\omega) = H_\mu(\omega)\,\delta\mu(\omega) + o(\delta\mu^2).$$

In this chapter we present the results derived originally in (Schuecker et al., 2015, Eq. 29). The transfer function reads

$$H_\mu(\omega) = H_G(\omega)\,\frac{1}{1+i\omega\tau_\mathrm{s}}. \tag{4.54}$$

with

$$H_G(\omega) = \frac{\nu_0\frac{\sqrt{2}}{\sigma}}{1+i\omega\tau_\mathrm{m}}\frac{\Phi'_\omega|_{x\theta}^{x_\mathrm{r}}}{\Phi_\omega|_{x\theta}^{x_\mathrm{r}}}, \tag{4.55}$$

for the oscillation frequency ω and the boundaries $x_{\{\mathrm{r},\theta\}} = \sqrt{2}y_{\{\theta,r\}}$. The first order low-pass filter on the right hand-side of Equation 4.54 comes from the exponential time course of the current-based synapses. The function $\Phi_\omega(x) = e^{\frac{1}{4}x^2}\,U\left(i\omega\tau_\mathrm{m} - \frac{1}{2}, x\right)$ is defined by parabolic cylinder functions U (Abramowitz and Stegun, 1974; Lindner and Schimansky-Geier, 2001) and $\Phi'_\omega = \partial_x\Phi_\omega$. $\Phi_\omega|_{x\theta}^{x_\mathrm{r}}$ is a short-hand notation for $\Phi_\omega(x_\mathrm{r}) - \Phi_\omega(x_\theta)$. The function h_μ from (Schuecker et al., 2015, Eq. 29) is then obtained as an inverse Fourier transform of H_μ,

$$\begin{aligned} h_\mu(t) &= \mathcal{F}^{-1}[H_\mu](t) \\ H_\mu(\lambda) &= \mathcal{L}[h_\mu](\lambda). \end{aligned} \tag{4.56}$$

Equation 4.56 implies $i\omega \to \lambda$ in Equation 4.55. The transfer function can also depend on the variance of the input,

$$H_{\sigma^2}(\omega) = \frac{1}{\sigma^2}\frac{\nu_0}{2+i\omega}\frac{\Phi''_\omega|_{x_\theta}^{x_\mathrm{r}}}{\Phi_\omega|_{x_\theta}^{x_\mathrm{r}}}.$$

In the current work we assumed that the contribution of H_{σ^2} is small and can be neglected.

4.9.7 Fixing the working point

Linearized stability analysis can only be done in the vicinity of a given steady state. To fix the working point of the spiking model, we assume a constant mean μ^* and variance σ^* of the input. Moreover, external excitatory and inhibitory input with Poisson-distributed interspike intervals is added to the recurrent input,

$$\begin{aligned} \mu^* &= \mu + \tau_\mathrm{m} J(\nu_\mathrm{E,ext} - g\nu_\mathrm{I,ext}) \\ \sigma^* &= \sigma + \tau_\mathrm{m} J^2 \Big(\nu_\mathrm{E,ext} + g^2 \nu_\mathrm{I,ext}\Big). \end{aligned} \tag{4.57}$$

with the excitatory and inhibitory connection strengths J and $-gJ$, respectively, and

$$\nu_\mathrm{E,ext} = \frac{\widetilde{\sigma}^2 + g\widetilde{\mu}}{1+g} \qquad \text{and} \qquad \nu_\mathrm{I,ext} \frac{\widetilde{\sigma}^2 - \widetilde{\mu}}{g(1+g)} \tag{4.58}$$

$$\text{with} \qquad \widetilde{\mu} = \frac{\mu^* - \mu}{\tau_\mathrm{m} J} \qquad \text{and} \qquad \widetilde{\sigma}^2 = \frac{(\sigma^*)^2 - \sigma^2}{\tau_\mathrm{m} J^2}.$$

4.9.8 Physical units

In order to simplify the calculations, we rescaled the equations that describe the sub-threshold dynamics of the LIF neuron (Equation 4.16), where the quantities V, J and I all have the unit Volt. Let us denote the original electric currents in the unit Ampere by $I^{'}$ and $J^{'}$. Then the relation between the original and rescaled quantities is given by

$$\begin{aligned} \tau_\mathrm{m} \frac{\partial V_i^{'}}{\partial t} &= -\Big(V_i^{'} - E_\mathrm{L}\Big) + R_\mathrm{m} I_i^{'}(t) \\ \tau_\mathrm{s} \frac{\partial I_i^{'}}{\partial t} &= -I_i^{'} + \tau_\mathrm{s} \sum_j J_{ij}^{'} s_j(t-d). \end{aligned} \tag{4.59}$$

The threshold and reset potential are then expressed as $V_\theta' = V_\theta + E_\mathrm{L}$ and $V_r' = V_r + E_\mathrm{L}$, respectively, with the reversal potential E_L. The membrane time constant is defined using the membrane resistance R_m and capacitance C_m, $\tau_\mathrm{m} = R_\mathrm{m} C_\mathrm{m}$ The total current input reads $I^{'} = I/R_\mathrm{m}$ and the synaptic weight amplitude $J^{'} = C_\mathrm{m} J/\tau_\mathrm{s}$.

4.9.9 Network simulation

The network simulation was written using the simulator NEST (Gewaltig and Diesmann, 2007; Hahne et al., 2017). The parameters for both neuron models and

Model summary	
Populations	Excitatory (E), inhibitory (I)
Topology	Ring network: Neurons positioned equally spaced on one-dimensional domain of length L; periodic boundary conditions
Connectivity	Random convergent connections with fixed in-degree, distance-dependent boxcar-shaped spatial profiles realized with cut-off masks
Spiking model	
Neuron model	Leaky integrate-and-fire (LIF), fixed threshold, absolute refractory time
Synapse model	Static weights and delays, exponentially shaped postsynaptic currents
Input	Independent fixed-rate Poisson spike trains to all neurons (excitatory and inhibitory Poisson sources)
Measurement	Spike activity
Rate model	
Neuron model	Rate neuron with tanh gain function
Synapse model	Delayed rate connection
Input	-
Measurement	Activity

Table 4.2: Summary of network models following the guidelines of Nordlie et al. (Nordlie et al., 2009). Separation between nonlinear spiking and rate neurons as used in NEST simulations. Reproduced from (Senk et al., 2020a).

Network models	
Distance-dependent connectivity	Neural units $j \in X$ at location x_j and $i \in Y$ at x_i in pre- and postsynaptic populations X and Y, respectively. Displacement between units i and j: $r_{ij} = x_i - x_j$ Boxcar-shaped spatial profile with width R and Heaviside function Θ: $p(r_{ij}) = \frac{1}{2R}\Theta(R - \lvert r_{ij}\rvert)$
Spiking model	
Subthreshold dynamics	If $t > t^* + \tau_{\text{ref}}$ $\frac{\mathrm{d}V}{\mathrm{d}t} = -\frac{V - E_{\text{L}}}{\tau_{\text{m}}} + \frac{I_{\text{syn}}(t)}{C_{\text{m}}}$ $I_{\text{syn}}(t) = \sum_j J_j I_{\text{PSC}}\Big(t - t_j^* - d\Big)$ with connection strength J_j, presynaptic spike time t_j^* and conduction delay d $I_{\text{PSC}}(t) = \mathrm{e}^{-t/\tau_{\text{s}}}\Theta(t)$ with Heaviside function Θ else $V(t) = V_r$
Spiking	If $V(t-) < V_\theta \wedge V(t+) \geq V_\theta$ 1. set $t^* = t$ 2. emit spike with timestamp t^* 3. reset $V(t) = V_{\text{r}}$
Rate model	
Differential equation	$\tau\frac{\partial u}{\partial t}(t) = -u(t) + \sum_{j=1} w_j \psi(u_j(t-d))$ with the nonlinearity $\psi(u) = \tanh(u)$

Table 4.3: Description of network models. Separation between nonlinear spiking and rate neurons as used in NEST simulations. Reproduced from (Senk et al., 2020a).

A: Global simulation parameters		
Symbol	**Value**	**Description**
T_{sim}	450 ms	Simulation duration
T_{trans}	250 ms	Start-up transient
dt	0.1 ms	Temporal resolution
B: Populations and external input		
Symbol	**Value**	**Description**
N_{E}	$4,000$	Population size of excitatory neurons
N_{I}	$1,000$	Population size of inhibitory neurons
L	1 mm	Domain length
Spiking model		
μ^*	10 mV	Mean input relative to resting potential
σ^*	10 mV	Variance of input relative to resting potential
$\nu_{\mathrm{E,ext}}$	$96,463$ Hz	⊛ Excitatory external rate (by fixing working point)
$\nu_{\mathrm{I,ext}}$	$15,958$ Hz	⊛ Inhibitory external rate (by fixing working point)
C: Connection parameters		
Symbol	**Value**	**Description**
R_{E}	0.2 mm	⊛ Profile width of excitatory neurons
R_{I}	0.07 mm	⊛ Profile width of inhibitory neurons
d	3 ms	⊛ Delay
Spiking model		
K_{E}	400	In-degree from excitatory neurons
γ	0.25	Relative in-degree, $\gamma = K_{\mathrm{I}}/K_{\mathrm{E}}$
J'_{E}	87.8 pA	⊛ Reference synaptic strength
g	5	⊛ Relative synaptic strength, $g = -J_{\mathrm{I}}/J_{\mathrm{E}}$
Rate model		
w_{E}	2.73	⊛ Excitatory weight (by parameter mapping)
w_{I}	−3.42	⊛ Inhibitory weight (by parameter mapping)
D: Neuron model		
Symbol	**Value**	**Description**
Spiking model		
C_{m}	250 pF	Membrane capacitance
τ_{m}	5 ms	Membrane time constant
E_{L}	−65 mV	Resting potential
V_θ	−50 mV	Firing threshold
V_{r}	−65 mV	Reset potential
τ_{ref}	0 ms	Absolute refractory period
τ_{s}	0.5 ms	Postsynaptic current time constant
Rate model		
τ	1.94 ms	Time constant (by parameter mapping)

Table 4.4: Simulation and network parameters. Parameters according to setting for wave trains as shown in Figure 4.1(d), Figure 4.3(d) and Figure 4.4(c) (black star marker). Deviant parameters are given in the captions of the respective figures and indicated by different markers. Reproduced from (Senk et al., 2020a).

network connectivity are given in Tables 4.2 and 4.3. The specific parameters used to generate wave trains in the simulations are presented in Table 4.4. Other network states were obtained with parameters marked by ⊛ in Table 4.4 and specified in the figure captions.

Neurons were positioned on a ring with perimeter L and spacing $\Delta x = L/N_{\mathrm{I}}$. The excitatory and inhibitory population sizes N_{E} and N_{I} were related as $N_{\mathrm{E}} = 4N_{\mathrm{I}}$ (Braitenberg, 2001), so on each position on the grid there is one inhibitory neuron and four excitatory neurons. The activity in Figs. 4.1, 4.3 and 4.4 was plotted for all inhibitory neurons and one excitatory neuron at each position. Connections between neurons were created using the NEST Topology module as random, distance-dependent and periodic at the boundary. The probability that two neurons are connected was 0.1 and the number of incoming connections to a neuron was fixed to $K_{\{\mathrm{E,I}\}} = 0.1 \cdot (N_{\mathrm{E}} + N_{\mathrm{I}})$. The spatial profile $R_{\{\mathrm{E,I}\}}$ is defined for each presynaptic population as a distance-dependent boxcar function, leading to a uniform connection probability within $R_{\{\mathrm{E,I}\}}$ from the postsynaptic neuron. A neuron can be connected to another one multiple times, but not to oneself. In each realization, a neuron may be connected to more neurons on the left than on the right or vice versa, leading to small drifts in the spatial pattern visible in Figure 4.3(b). Such drifts disappear when symmetric connectivity scheme is required (Senk et al., 2020a).

For the spiking neuron model, the leaky integrate-and-fire model with exponential postsynaptic currents was chosen (called `iaf_psc_exp` in the NEST simulator). Neurons receive both excitatory and inhibitory external input created by a Poisson generator with rates $\nu_{\{\mathrm{E,I}\},\mathrm{ext}}$ determined based on Equation 4.58 for fixing the working point (μ, σ). The rate neuron model was chosen as the NEST `tanh_ipn` with a hyperbolic gain function and the variance of the input set to zero. Simulation plots omit the initial period of T_{trans}.

4.9.10 Software and implementation

All simulations were implemented in the NEST simulator v2.18.0 (Jordan et al., 2019) with Python v3.6.9. Analysis of the results was written in Python, using the packages NumPy v1.16.4, SciPy v1.2.1, and Matplotlib v3.0.2. The python code that was used to produce the results and figures contained in the manuscript is available at Zenodo (Senk et al., 2020b). The core functions are also available as part of the Python package LIF Meanfield Tools (https://github.com/INM-6/lif_meanfield_tools), v0.2 and higher (Layer et al., 2020).

5 Discussion

In Chapter 2, we demonstrated that a brief continuous optical stimulation of MSDB VGluT2 neurons initiated locomotion accompanied by the hippocampal theta oscillation. The role of the VGluT2 neurons was previously attributed to providing tonic excitatory input to the MSDB PV subpopulation that in turn generates the theta rhythm (Robinson et al., 2016; Kocsis et al., 2021). Our results are in agreement with this hypothesis and identify a possible mechanism how the tonic excitation is generated. In particular, we observed robust persistent firing in a MSDB subpopulation upon a brief continuous light stimulation of MSDB VGluT2 neurons, that might be necessary for the theta generation. We provided evidence supporting the hypothesis that the persistent firing is generated intrinsically by the MSDB VGluT2 neurons. Furthermore, we showed that optogenetic activation of the MSDB VGluT2 neurons by a brief continuous pulse is sufficient to induce locomotion, independently of the synaptic connectivity within the MSDB. As the hippocampal theta oscillation was abolished by blocking synaptic transmission within the MSDB, the motor-generating circuit is distinct from the theta generating circuit and, in particular the hippocampal theta oscillation is not a prerequisite for locomotion. However, many questions still remain to be answered. Firstly, our results support the hypothesis that the observed persistent firing is generated intrinsically by the MSDB VGluT2 neurons, but the exact mechanism still remains to be identified. In particular, we could not completely exclude the possibility that other cell types than VGluT2 take part in the persistent firing due to the activation of metabotropic glutamate receptors. Secondly, identifying the septo-fugal axonal projections of MSDB cells that produce persistent firing would yield better understanding of the functional role that the persistent firing plays for both the hippocampal theta oscillation and locomotion.

The analysis of MSDB neural activity in relation to locomotion resulted in an additional prospective direction of research. We noticed a pronounced beta power (15-30 Hz) in the MSDB extracellular potential that was strongly temporally correlated with locomotion (Figure 5.1A). The beta power was also triggered by a

brief continuous optical stimulation (Figure 5.1B). This effect was strongest in the first recording session and faded away in the following sessions (Figure 5.1C). In the first recording session, the difference between the average beta power at rest versus locomotion, both voluntary and stimulus-induced, was very prominent (Figures 5.1D,E). We didn't observe any locomotion-related modulation of the MSDB beta power after blocking synaptic transmission (Figures 5.1F-H). Furthermore, in 1 out of 19 acute MSDB slice preparations, a clear beta power increase was detected in the local-field potential in response to a brief continuous optical stimulation of the MSDB VGluT2 neurons (Figure 5.2). Our results are consistent with the previously observed learning-dependent modulation of the beta power in the basal forebrain (Quinn et al., 2010). Tingley et al. (2018) related beta power modulation in the basal forebrain to variations in experience and performance-related cognitive processing. Additional experiments will be necessary to assess the mechanism of generation and the functional role of the MSDB beta power modulation.

In Chapter 3 we further explored the possible mechanisms of MSDB theta generation by analyzing spontaneous spiking activity in an acute MSDB slice preparation. We found significant cross-correlations between MSDB units in the theta frequency range, irrespective of their distance. Blocking synaptic transmission led to even more regular spiking of individual units and although less prominent, theta-band cross-correlations between units even at long distances were still present. These results provide further support for the view formulated by Kocsis et al. (2021) that the MSDB neurons intrinsically produce regular firing in the theta frequency range, and the main role of the synaptic network is to synchronize them. Moreover, our results suggest that other mechanisms such as gap junctions further support the synchronization. An additional experiment will be needed to confirm this hypothesis and to describe how the theta-rhythmic firing is generated on the cellular level.

Another open question is how the spatio-temporal organization of the hippocampal theta activity emerges. To better understand the role of the MSDB in the generation of the hippocampal wave train, it would be neccessary to map the MSDB input to the hippocampus, e.g. by two-photon imaging of the septo-hippocampal axons. Possible mechanisms how the MSDB might contribute to a phase-offset of the theta oscillation between different hippocampal sites include localized input to a certain hippocampal site from which the wave train spreads, or spatially organized projections from different MSDB subpopulations with a phase offset (Borhegyi et al., 2004).

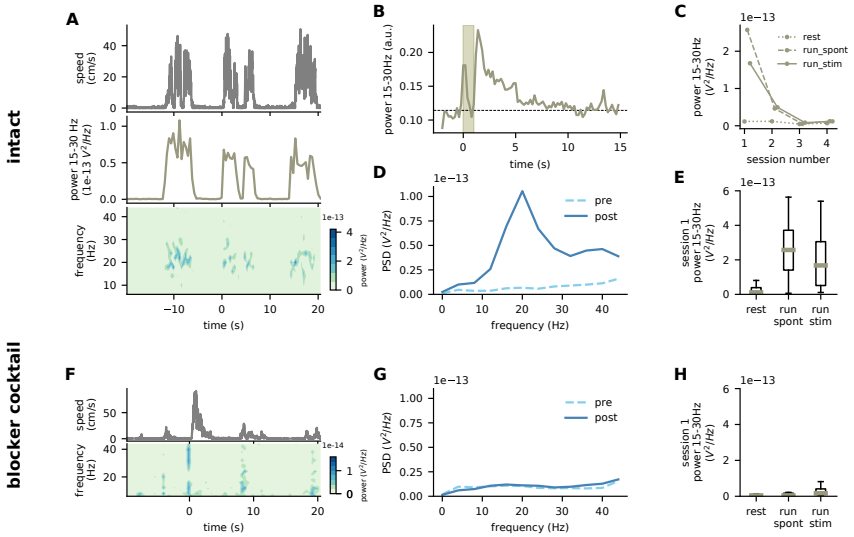

Figure 5.1: **MSDB beta power modulation during locomotion. A.** Single-trial example of locomotion speed (upper panel), average beta power in the MSDB local-field potential (middle panel) and the corresponding spectrogram (lower panel). **B.** Trial-averaged power in the beta frequency band. Gray region marks the period of continuous light stimulation of the MSDB VGluT2 neurons. **C.** Beta power averaged across trials within each recording session. Traces correspond to rest, spontaneous running and stimulus-induced running. **D.** Trial-averaged power-spectral density with 2 seconds before (pre) and 2 seconds after (post) the stimulus. **E.** Mean beta power across trials during rest, spontaneous and stimulus-induced running. **F.-H.** As A,D,E respectively with blocked synaptic transmission in the MSDB.

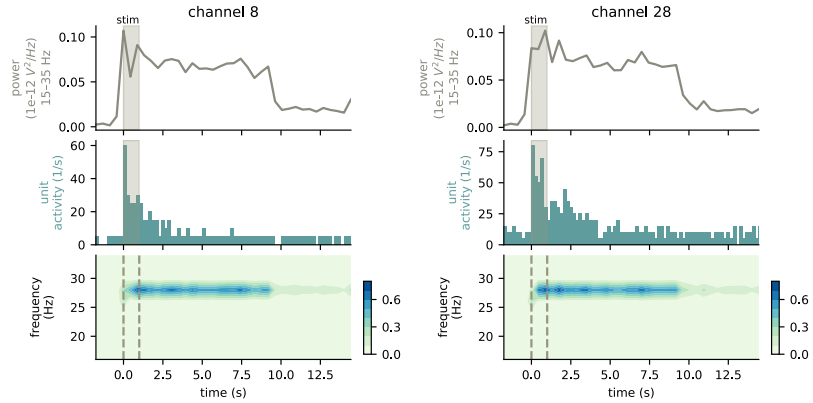

Figure 5.2: **Stimulus-induced beta oscillation in a MSDB slice preparation.** Single trial example of stimulus-induced beta oscillations in two representative channels recorded from an acute MSDB slice preparation. MSDB VGluT2 neurons were stimulated with a 1s continuous light pulse (see Section 2.5 for details). Stimulus period is marked by the gray region, resp. dashed line. Mean beta power in the interval 15-35 Hz (upper row), single-unit instantaneous firing rate (middle row, bin size 200ms) and a spectrogram of the local-field potential (bottom row, frequency resolution 2 Hz).

In Chapter 4, a systematic mapping between a spatially-resolved model of a spiking neural network and the corresponding population neural field model was derived. This parameter mapping constitutes a tool for the transfer of results obtained from the population neural field model to a spiking neural network model. Concretely, we provided conditions for parameters of the spiking neural network that produce temporal oscillations, spatial patterns or travelling waves. Conversely, the mapping can be used to define the parameters of the neural field model based on experimental results. The presented method also has an important didactical value, as it intuitively explains the meaning of the parameters in the neural field model. The practical value of the parameter mapping is limited by the underlying assumptions such as homogeneity of the network and the leaky-integrate-and-fire neuron model with exponential synapses. Extending the framework to existing more complex models of cortical processing, for instance by including other neuron and synapse types, would be of great value. Relatively straightforward extensions of the framework are the generalization to a two-dimensional spatial domain, including more realistic connectivity profiles or multiple neural populations. Last but not least, the framework will only gain its full value when it is applied to a concrete biological problem and generates predictions that can be experimentally tested.

Bibliography

Abramowitz, M. and Stegun, I. A. (1974). *Handbook of Mathematical Functions: with Formulas, Graphs, and Mathematical Tables.* Dover Publications, New York.

Amari, S.-I. (1977). Dynamics of pattern formation in lateral-inhibition type neural fields. *Biol. Cybern.*, 27(2):77–87.

Amit, D. J. and Brunel, N. (1997a). Dynamics of a recurrent network of spiking neurons before and following learning. *Netw. Comput. Neural Syst.*, 8(4):373–404.

Amit, D. J. and Brunel, N. (1997b). Model of global spontaneous activity and local structured activity during delay periods in the cerebral cortex. *Cerebral Cortex*, 7:237–252.

Anastassiou, C. A., Perin, R., Markram, H., and Koch, C. (2011). Ephaptic coupling of cortical neurons. *Nature Neuroscience*, 14:217–223.

Atay, F. M. and Hutt, A. (2005). Stability and bifurcations in neural fields with finite propagation speed and general connectivity. *SIAM J. Appl. Dyn. Syst.*, 65(2):664–666.

Atay, F. M. and Hutt, A. (2006). Neural fields with distributed transmission speeds and long-range feedback delays. *SIAM J. Appl. Dyn. Syst.*, 5(4):670–698.

Avitable, D. and Wedgwood, K. C. A. (2017). Macroscopic coherent structures in a stochastic neural network: from interface dynamics to coarse-grained bifurcation analysis. *J. Math. Biol.*, 75(4):885–928.

Barak, O. and Tsodyks, M. (2007). Persistent activity in neural networks with dynamic synapses. *PLoS Computational Biology*, 3:0323–0332.

Barak, O. and Tsodyks, M. (2014). Working models of working memory. *Current Opinion in Neurobiology*, 25:20–24.

Barnett, A. H., Magland, J. F., and Greengard, L. F. (2016). Validation of neural spike sorting algorithms without ground-truth information. *Journal of Neuroscience Methods*, 264:65–77.

Barraclough, D. J., Conroy, M. L., and Lee, D. (2004). Prefrontal cortex and decision making in a mixed-strategy game. *Nature Neuroscience*, 7:404–410.

Bartoli, E., Bosking, W., Chen, Y., Li, Y., Sheth, S. A., Beauchamp, M. S., Yoshor, D., and Foster, B. L. (2019). Functionally distinct gamma range activity revealed by stimulus tuning in human visual cortex. *Current Biology*, 29:3345–3358.e7.

Berger, H. (1929). Über das elektrenkephalogramm des menschen. *Arch f Psychiatr.*, 87:527–570.

Bezgin, G., Reid, A. T., Schubert, D., and Kötter, R. (2009). Matching spatial with ontological brain regions using java tools for visualization, database access, and integrated data analysis. *Neuroinformatics*, 7:7–22.

Bland, B. H. (1986). The physiology and pharmacology of hippocampal formation theta rhythms. *Progress in Neurobiology*, 26:1–54.

Bland, B. H., Jackson, J., Derrie-Gillespie, D., Azad, T., Rickhi, A., and Abriam, J. (2006). Amplitude, frequency, and phase analysis of hippocampal theta during sensorimotor processing in a jump avoidance task. *Hippocampus*, 16:673–681.

Bohbot, V. D., Copara, M. S., Gotman, J., and Ekstrom, A. D. (2017). Low-frequency theta oscillations in the human hippocampus during real-world and virtual navigation. *Nature Communications*, 8:1–7.

Bojak, I. and Liley, D. T. J. (2010). Axonal velocity distributions in neural field equations. *PLOS Comput. Biol.*, 6(1):e1000653.

Bolding, K. A., Ferbinteanu, J., Fox, S. E., and Muller, R. U. (2020). Place cell firing cannot support navigation without intact septal circuits. *Hippocampus*, 30:175–191.

Borhegyi, Z., Varga, V., Szilágyi, Z., Fabo, D., and Freund, T. F. (2004). Phase segregation of medial septal gabaergic neurons during hippocampal theta activity. *Journal of Neuroscience*, 24:8470–8479.

Bose, A. and Recce, M. (2001). Phase precession and phase-locking of hippocampal pyramidal cells. *Hippocampus*, 11:204–215.

Bosman, C. A., Schoffelen, J.-M., Brunet, N., Oostenveld, R., Bastos, A. M., Womelsdorf, T., Rubehn, B., Stieglitz, T., De Weerd, P., and Fries, P. (2012). Attentional stimulus selection through selective synchronization between monkey visual areas. *Neuron*, 75:875–888.

Bragin, A., Jandó, G., Nádasdy, Z., Hetke, J., Wise, K., and Buzsáki, G. (1995). Gamma (40-100 hz) oscillation in the hippocampus of the behaving rat. *Journal of Neuroscience*, 15:47–60.

Braitenberg, V. (2001). Brain size and number of neurons: an exercise in synthetic neuroanatomy. *J. Comput. Neurosci.*, 10(1):71–77.

Branco, T. and Costa, G. (2020). Scidraw | about.

Brandon, M. P., Bogaard, A. R., Libby, C. P., Connerney, M. A., Gupta, K., and Hasselmo, M. E. (2011). Reduction of theta rhythm dissociates grid cell spatial periodicity from directional tuning. *Science*, 332:595–599.

Bressloff, P. C. (2012). Spatiotemporal dynamics of continuum neural fields. *J. Phys. A: Math. Theor.*, 45(3):033001.

Bressloff, P. C. (2014). *Waves in Neural Media*. Springer New York.

Bressloff, P. C. and Coombes, S. (1998). Spike train dynamics underlying pattern formation in integrate-and-fire oscillator networks. *Phys. Rev. Lett.*, 81(11):2384–2387.

Bressloff, P. C. and Coombes, S. (2000). A dynamical theory of spike train transitions in networks of integrate-and-fire oscillators. *SIAM J. Appl. Math.*, 60(3):820–841.

Bressloff, P. C. and Kilpatrick, Z. P. (2008). Nonlocal Ginzburg-Landau equation for cortical pattern formation. *Phys. Rev. E*, 78(4):–.

Brunel, N. (2000). Dynamics of sparsely connected networks of excitatory and inhibitory spiking neurons. *J. Comput. Neurosci.*, 8(3):183–208.

Brunel, N., Chance, F. S., Fourcaud, N., and Abbott, L. F. (2001). Effects of synaptic noise and filtering on the frequency response of spiking neurons. *Phys. Rev. Lett.*, 86(10):2186–2189.

Brunel, N. and Hakim, V. (1999). Fast global oscillations in networks of integrate-and-fire neurons with low firing rates. *Neural Comput.*, 11(7):1621–1671.

Brunel, N. and Latham, P. (2003). Firing rate of the noisy quadratic integrate-and-fire neuron. *Neural Comput.*, 15(10):2281–2306.

Buice, M. A., Cowan, J. D., and Chow, C. C. (2010). Systematic fluctuation expansion for neural network activity equations. *Neural Comput.*, 22:377–426.

Bush, D., Bisby, J. A., Bird, C. M., Gollwitzer, S., Rodionov, R., Diehl, B., McEvoy, A. W., Walker, M. C., and Burgess, N. (2017). Human hippocampal theta power indicates movement onset and distance travelled. *Proceedings of the National Academy of Sciences of the United States of America*, 114:12297–12302.

Buzsáki, G. (2002). Theta oscillations in the hippocampus. *Neuron*, 33:325–340.

Buzsáki, G. (2005). Theta rhythm of navigation: Link between path integration and landmark navigation, episodic and semantic memory. *Hippocampus*, 15:827–840.

Buzsáki, G. (2009). Rhythms of the brain. *Rhythms of the Brain*, pages 1–464.

Buzsáki, G. (2019). *The Brain from Inside Out*. Oxford University Press.

Buzsáki, G., Buhl, D. L., Harris, K. D., Csicsvari, J., Czéh, B., and Morozov, A. (2003). Hippocampal network patterns of activity in the mouse. *Neuroscience*, 116:201–211.

Buzsáki, G., Logothetis, N., and Singer, W. (2013). Scaling brain size, keeping timing: Evolutionary preservation of brain rhythms. *Neuron*, 80:751–764.

Buzsáki, G. and Watson, B. O. (2012). Brain rhythms and neural syntax: Implications for efficient coding of cognitive content and neuropsychiatric disease. *Dialogues in Clinical Neuroscience*, 14:345–367.

Canolty, R. T. and Knight, R. T. (2010). The functional role of cross-frequency coupling. *Trends in Cognitive Sciences*, 14:506–515.

Cashdollar, N., Malecki, U., Rugg-Gunn, F. J., Duncan, J. S., Lavie, N., and Duzel, E. (2009). Hippocampus-dependent and -independent theta-networks of active maintenance. *Proceedings of the National Academy of Sciences of the United States of America*, 106:20493–20498.

Colgin, L. L., Denninger, T., Fyhn, M., Hafting, T., Bonnevie, T., Jensen, O., Moser, M. B., and Moser, E. I. (2009). Frequency of gamma oscillations routes flow of information in the hippocampus. *Nature*, 462:353–357.

Collins, A. L. and Saunders, B. T. (2019). Brain reward network effects underlie septo-hippocampal control of flexible decision making. *Neuropsychopharmacology*, 44:2153–2154.

Colom, L. V. (2006). Septal networks: Relevance to theta rhythm, epilepsy and alzheimer's disease. *Journal of Neurochemistry*, 96:609–623.

Compte, A. (2006). Computational and in vitro studies of persistent activity: Edging towards cellular and synaptic mechanisms of working memory. *Neuroscience*, 139:135–151.

Coombes, S. (2005). Waves, bumps, and patterns in neural field theories. *Biol. Cybern.*, 93:91–108.

Coombes, S. (2010). Large-scale neural dynamics: Simple and complex. *NeuroImage*, 52(3):731–739.

Coombes, S., beim Graben, P., Potthast, R., and Wright, J., editors (2014). *Neural Fields*. Springer Berlin Heidelberg.

Coombes, S., Venkov, N. A., Shiau, L., Bojak, I., Liley, D. T. J., and Laing, C. R. (2007). Modeling electrocortical activity through improved local approximations of integral neural field equations. *Phys. Rev. E*, 76(5):–.

Corless, R. M., Gonnet, G. H., Hare, D. E. G., Jeffrey, D. J., and Knuth, D. E. (1996). On the Lambert W function. *Adv. Comput. Math.*, 5(1):329–359.

Crook, S. M., Ermentrout, G. B., Vanier, M. C., and Bower, J. M. (1997). The role of axonal delay in the synchronization of networks of coupled cortical oscillators. *J. Comput. Neurosci.*, 4(2):161–172.

Dannenberg, H., Kelley, C., Hoyland, A., Monaghan, C. K., and Hasselmo, M. E. (2019). The firing rate speed code of entorhinal speed cells differs across behaviorally relevant time scales and does not depend on medial septum inputs. *Journal of Neuroscience*, 39:3434–3453.

Deco, G., Jirsa, V. K., Robinson, P. A., Breakspear, M., and Friston, K. (2008). The dynamic brain: From spiking neurons to neural masses and cortical fields. *PLOS Comput. Biol.*, 4(8):e1000092.

Diekmann, O. and Korvasová, K. (2016). Linearization of solution operators for state-dependent delay equations: A simple example. *Discrete and Continuous Dynamical Systems- Series A*, 36:137–149.

Dugué, L., Marque, P., and VanRullen, R. (2015). Theta oscillations modulate attentional search performance periodically. *Journal of Cognitive Neuroscience*, 27:945–958.

Eccles, J. C., P., F., and Koketsu, K. (1954). Cholinergic and inhibitory synapses in a pathway from motor-axon collaterals to motoneurones. *J. Physiol. (Lond.)*, 126(3):524–562.

Ekstrom, A. D., Kahana, M. J., Caplan, J. B., Fields, T. A., Isham, E. A., Newman, E. L., and Fried, I. (2003). Cellular networks underlying human spatial navigation. *Nature*, 425(6954):184–188.

El Boustani, S. and Destexhe, A. (2009). A master equation formalism for macroscopicmodeling of asynchronous irregular activity states. *Neural Comput.*, 21:46–100.

Ermentrout, B. (1994). Reduction of conductance-based models with slow synapses to neural nets. *Neural Comput.*, 6(4):679–695.

Ermentrout, B. (1998). Neural networks as spatio-temporal pattern-forming systems. *Rep. Prog. Phys.*, 61(4):353–430.

Ermentrout, B. G. and Cowan, J. D. (1980a). Large scale spatially organized activity in neural nets. *SIAM J. Appl. Math.*, 38(1):1–21.

Ermentrout, G. B. and Cowan, J. D. (1979a). A mathematical theory of visual hallucination patterns. *Biol. Cybern.*, 34(3):137–150.

Ermentrout, G. B. and Cowan, J. D. (1979b). Temporal oscillations in neuronal nets. *J. Math. Biol.*, 7(3):265–280.

Ermentrout, G. B. and Cowan, J. D. (1980b). Secondary bifurcation in neuronal nets. *SIAM J. Appl. Math.*, 39(2):323–340.

Ermentrout, G. B. and Kleinfeld, D. (2001). Traveling electrical waves in cortex: Insights from phase dynamics and speculation on a computational role. *Neuron*, 29:33–44.

Ermentrout, G. B. and Kopell, N. (1986). Parabolic bursting in an excitable system coupled with a slow oscillation. *SIAM Journal on Applied Mathematics*, 46(2):233–253.

Everitt, B. J. and Robbins, T. W. (1997). Central cholinergic systems and cognition. *Annual Review of Psychology*, 48:649–684.

Faye, G. and Faugeras, O. (2010). Some theoretical and numerical results for delayed neural field equations. *Physica D*, 239(9):561–578.

Fermani, F. and Richardson, M. J. E. (2015). Coarse-grained description of the spatio-temporal dynamics of network activity from experimentally verified single-neuron models and connectivity. In *24th Annual Computational Neuroscience Meeting: CNS*2015, BMC Neuroscience 2015, 16(Suppl 1):P206.*

Fisher, R. S. (2015). Stimulation of the medial septum should benefit patients with temporal lobe epilepsy. *Medical Hypotheses*, 84:543–550.

Folias, S. E. and Ermentrout, G. B. (2012). Bifurcations of stationary solutions in an interacting pair of e-i neural fields. *SIAM J. Appl. Dyn. Syst.*, 11(3):895–938.

Fourcaud, N. and Brunel, N. (2002). Dynamics of the firing probability of noisy integrate-and-fire neurons. *Neural Comput.*, 14(9):2057–2110.

Fourcaud-Trocmé, N. and Brunel, N. (2005). Dynamics of the instantaneous firing rate in response to changes in input statistics. *J. Comput. Neurosci.*, 18(3):311–321.

Fournier, J., Saleem, A. B., Diamanti, E. M., Wells, M. J., Harris, K. D., and Carandini, M. (2020). Mouse visual cortex is modulated by distance traveled and by theta oscillations. *Current Biology*, 0.

Franklin, K. and Paxinos, G. (2008). *The Mouse Brain in Stereotaxic Coordinates*. Academic Press, Elsevier.

Fransén, E., Tahvildari, B., Egorov, A. V., Hasselmo, M. E., and Alonso, A. A. (2006). Mechanism of graded persistent cellular activity of entorhinal cortex layer v neurons. *Neuron*, 49:735–746.

Fries, P. (2005). A mechanism for cognitive dynamics: neuronal communication through neuronal coherence. *Theor. Comput. Sci.*, 9(10):474–480.

Frotscher, M. and Léránth, C. (1985). Cholinergic innervation of the rat hippocampus as revealed by choline acetyltransferase immunocytochemistry: A combined light and electron microscopic study. *The Journal of Comparative Neurology*, 239:237–246.

Fuhrmann, F., Justus, D., Sosulina, L., Kaneko, H., Beutel, T., Friedrichs, D., Schoch, S., Schwarz, M., Fuhrmann, M., and Remy, S. (2015). Locomotion, theta oscillations, and the speed-correlated firing of hippocampal neurons are controlled by a medial septal glutamatergic circuit. *Neuron*, 86:1253–1264.

Fuster, J. M. (1973). Unit activity in prefrontal cortex during delayed-response performance: neuronal correlates of transient memory. *Journal of neurophysiology*, 36:61–78.

Gangadharan, G., Shin, J., Kim, S. W., Kim, A., Paydar, A., Kim, D. S., Miyazaki, T., Watanabe, M., Yanagawa, Y., Kim, J., Kim, Y. S., Kim, D., and Shin, H. S. (2016). Medial septal gabaergic projection neurons promote object exploration behavior and type 2 theta rhythm. *Proceedings of the National Academy of Sciences of the United States of America*, 113:6550–6555.

Garner, H. L., Whittington, M. A., and Henderson, Z. (2005). Induction by kainate of theta frequency rhythmic activity in the rat medial septum-diagonal band complex in vitro. *Journal of Physiology*, 564:83–102.

Gewaltig, M.-O. and Diesmann, M. (2007). NEST (NEural Simulation Tool). *Scholarpedia*, 2(4):1430.

Girard, P., Hupé, J. M., and Bullier, J. (2001). Feedforward and feedback connections between areas V1 and V2 of the monkey have similar rapid conduction velocities. *J. Neurophysiol.*, 85(3):1328–1331.

González, J., Cavelli, M., Mondino, A., Rubido, N., Tort, A. B., and Torterolo, P. (2020). Communication through coherence by means of cross-frequency coupling. *Neuroscience*, 449:157–164.

Goodman, M. S., Kumar, S., Zomorrodi, R., Ghazala, Z., Cheam, A. S. M., Barr, M. S., Daskalakis, Z. J., Blumberger, D. M., Fischer, C., Flint, A., Mah, L., Herrmann, N., Bowie, C. R., Mulsant, B. H., and Rajji, T. K. (2018). Theta-gamma coupling and working memory in alzheimer's dementia and mild cognitive impairment. *Frontiers in Aging Neuroscience*, 10:101.

Gottlieb, Y., Vaadia, E., and Abeles, M. (1989). Single unit activity in the auditory cortex of a monkey performing a short term memory task. *Experimental Brain Research*, 74:139–148.

Goyal, A., Miller, J., Qasim, S. E., Watrous, A. J., Zhang, H., Stein, J. M., Inman, C. S., Gross, R. E., Willie, J. T., Lega, B., Lin, J. J., Sharan, A., Wu, C., Sperling, M. R., Sheth, S. A., McKhann, G. M., Smith, E. H., Schevon, C., and Jacobs, J. (2020). Functionally distinct high and low theta oscillations in the human hippocampus. *Nature Communications*, 11:1–10.

Gray, C. M. (1999). The temporal correlation hypothesis of visual feature integration: Still alive and well. *Neuron*, 24:31–47.

Green, J. D. and Arduini, A. A. (1954). Hippocampal electrical activity in arousal. *Journal of neurophysiology*, 17:533–557.

Gregoriou, G. G., Paneri, S., and Sapountzis, P. (2015). Oscillatory synchrony as a mechanism of attentional processing. *Brain Res.*, 1626:165 – 182. Predictive and Attentive Processing in Perception and Action.

Hahne, J., Dahmen, D., Schuecker, J., Frommer, A., Bolten, M., Helias, M., and Diesmann, M. (2017). Integration of continuous-time dynamics in a spiking neural network simulator. *Front. Neuroinf.*, 11:34.

Hajszan, T., Alreja, M., and Leranth, C. (2004). Intrinsic vesicular glutamate transporter 2-immunoreactive input to septohippocampal parvalbumin-containing neurons: Novel glutamatergic local circuit cells. *Hippocampus*, 14:499–509.

Hangya, B., Borhegyi, Z., Szilagyi, N., Freund, T. F., and Varga, V. (2009). Gabaergic neurons of the medial septum lead the hippocampal network during theta activity. *Journal of Neuroscience*, 29:8094–8102.

Hart, E. and Huk, A. C. (2020). Recurrent circuit dynamics underlie persistent activity in the macaque frontoparietal network. *eLife*, 9:1–22.

Harvey, C. D., Coen, P., and Tank, D. W. (2012). Choice-specific sequences in parietal cortex during a virtual-navigation decision task. *Nature*, 484:62–68.

Hasselmo, M. and McGaughy, J. (2004). High acetylcholine levels set circuit dynamics for attention and encoding and low acetylcholine levels set dynamics for consolidation. *Prog Brain Res.*, 145:207–231.

Hasselmo, M. E. (2006). The role of acetylcholine in learning and memory. *Curr. Op. Neurobiol.*, 16:710–715.

Hasselmo, M. E. and Giocomo, L. M. (2006). Cholinergic modulation of cortical function. volume 30, pages 133–135. Springer.

Heiberg, T., Kriener, B., Tetzlaff, T., Casti, A., Einevoll, G., and Plesser, H. (2013). Firing-rate models capture essential response dynamics of LGN relay cells. *J. Comput. Neurosci.*, 35(3):359–375.

Helias, M., Tetzlaff, T., and Diesmann, M. (2013). Echoes in correlated neural systems. *New J Phys.*, 15:023002.

Hellwig, B. (2000). A quantitative analysis of the local connectivity between pyramidal neurons in layers 2/3 of the rat visual cortex. *Biol. Cybern.*, 2(82):111–121.

Histed, M. H., Pasupathy, A., and Miller, E. K. (2009). Learning substrates in the primate prefrontal cortex and striatum: Sustained activity related to successful actions. *Neuron*, 63:244–253.

Hodgkin, A. L. and Huxley, A. F. (1952). A quantitative description of membrane current and its application to conduction and excitation in nerve. *J. Physiol. (Lond.)*, 117:500–544.

Hughes, S. W., Lörincz, M., Cope, D. W., Blethyn, K. L., Kékesi, K. A., Parri, H. R., Juhász, G., and Crunelli, V. (2004). Synchronized oscillations at alpha and theta frequencies in the lateral geniculate nucleus. *Neuron*, 42:253–268.

Huh, C. Y. L., Goutagny, R., and Williams, S. (2010). Glutamatergic neurons of the mouse medial septum and diagonal band of broca synaptically drive hippocampal pyramidal cells: Relevance for hippocampal theta rhythm. *Journal of Neuroscience*, 30:15951–15961.

Hutt, A. (2008). Local excitation-lateral inhibition interaction yields oscillatory instabilities in nonlocally interacting systems involving finite propagation delay. *Phys. Lett. A*, 372(5):541–546.

Hutt, A., Bestehorn, M., and Wennekers, T. (2003). Pattern formation in intracortical neuronal fields. *Netw. Comput. Neural Syst.*, 14(2):351–368.

Hutt, A. and Rougier, N. (2010). Activity spread and breathers induced by finite transmission speeds in two-dimensional neural fields. *Phys. Rev. E*, 82(5):–.

Händel, B. and Haarmeier, T. (2009). Cross-frequency coupling of brain oscillations indicates the success in visual motion discrimination. *NeuroImage*, 45:1040–1046.

Iaccarino, H. F., Singer, A. C., Martorell, A. J., Rudenko, A., Gao, F., Gillingham, T. Z., Mathys, H., Seo, J., Kritskiy, O., Abdurrob, F., Adaikkan, C., Canter, R. G., Rueda, R., Brown, E. N., Boyden, E. S., and Tsai, L. H. (2016). Gamma frequency entrainment attenuates amyloid load and modifies microglia. *Nature*, 540:230–235.

Inagaki, H. K., Fontolan, L., Romani, S., and Svoboda, K. (2019). Discrete attractor dynamics underlies persistent activity in the frontal cortex. *Nature*, 566:212–217.

Izadi, A., Pevzner, A., Lee, D. J., Ekstrom, A. D., Shahlaie, K., and Gurkoff, G. G. (2019). Medial septal stimulation increases seizure threshold and improves cognition in epileptic rats. *Brain Stimulation*, 12:735–742.

Izhikevich, E. M. (2003). Simple model of spiking neurons. *IEEE Trans. Neural Netw.*, 14(6):1569–1572.

Jacobs, J. (2014). Hippocampal theta oscillations are slower in humans than in rodents: Implications for models of spatial navigation and memory. *Philosophical Transactions of the Royal Society B: Biological Sciences*, 369.

Jeong, D. U., Lee, J. E., Lee, S. E., Chang, W. S., Kim, S. J., and Chang, J. W. (2014). Improvements in memory after medial septum stimulation are associated with changes in hippocampal cholinergic activity and neurogenesis. *BioMed Research International*, 2014.

Jirsa, V. K. and Kelso, J. A. S. (2000). Spatiotemporal pattern formation in neural systems with heterogeneous connection topologies. *Phys. Rev. E*, 62(6):8462–8465.

Jochems, A. and Yoshida, M. (2015). A robust in vivo-like persistent firing supported by a hybrid of intracellular and synaptic mechanisms. *PLOS ONE*, 10:e0123799.

Jordan, J., Ippen, T., Helias, M., Kitayama, I., Sato, M., Igarashi, J., Diesmann, M., and Kunkel, S. (2018). Extremely scalable spiking neuronal network simulation code: From laptops to exascale computers. *Front. Neuroinf.*, 12:2.

Jordan, J., Mørk, H., Vennemo, S. B., Terhorst, D., Peyser, A., Ippen, T., Deepu, R., Eppler, J. M., van Meegen, A., Kunkel, S., Sinha, A., Fardet, T., Diaz, S., Morrison, A., Schenck, W., Dahmen, D., Pronold, J., Stapmanns, J., Trensch, G.,

Spreizer, S., Mitchell, J., Graber, S., Senk, J., Linssen, C., Hahne, J., Serenko, A., Naoumenko, D., Thomson, E., Kitayama, I., Berns, S., and Plesser, H. E. (2019). Nest 2.18.0.

Justus, D., Dalügge, D., Bothe, S., Fuhrmann, F., Hannes, C., Kaneko, H., Friedrichs, D., Sosulina, L., Schwarz, I., Elliott, D. A., Schoch, S., Bradke, F., Schwarz, M. K., and Remy, S. (2017). Glutamatergic synaptic integration of locomotion speed via septoentorhinal projections. *Nature Neuroscience*, 20:16–19.

Keane, A. and Gong, P. (2015). Propagating waves can explain irregular neural dynamics. *J. Neurosci.*, 35(4):1591–1605.

Kennedy, A., Kunwar, P. S., yun Li, L., Stagkourakis, S., Wagenaar, D. A., and Anderson, D. J. (2020). Stimulus-specific hypothalamic encoding of a persistent defensive state. *Nature*, 586:730–734.

Kiehn, O. and Eken, T. (1998). Functional role of plateau potentials in vertebrate motor neurons. *Current Opinion in Neurobiology*, 8(6):746–752.

King, C., Recce, M., and O'Keefe, J. (1998). The rhythmicity of cells of the medial septum/diagonal band of broca in the awake freely moving rat: Relationships with behaviour and hippocampal theta. *European Journal of Neuroscience*, 10:464–477.

Kiss, J., Patel, A. J., Baimbridge, K. G., and Freund, T. F. (1990). Topographical localization of neurons containing parvalbumin and choline acetyltransferase in the medial septum-diagonal band region of the rat. *Neuroscience*, 36:61–72.

Knauer, B., Jochems, A., Valero-Aracama, M. J., and Yoshida, M. (2013). Long-lasting intrinsic persistent firing in rat ca1 pyramidal cells: A possible mechanism for active maintenance of memory. *Hippocampus*, 23:820–831.

Kocsis, B., Martínez-Bellver, S., Fiáth, R., Domonkos, A., Sviatkó, K., Barthó, P., Freund, T. F., Ulbert, I., Káli, S., Varga, V., and Hangya, B. (2021). Huygens synchronization of medial septal pacemaker neurons generates hippocampal theta oscillation. *bioRxiv*, page 2021.01.22.427736.

Koenig, J., Linder, A. N., Leutgeb, J. K., and Leutgeb, S. (2011). The spatial periodicity of grid cells is not sustained during reduced theta oscillations. *Science*, 332:592–595.

Korvasová, K., Ludwig, F., Kaneko, H., Sosulina, L., Tetzlaff, T., Remy, S., and Mikulovic, S. (2021). Locomotion induced by medial septal glutamatergic neurons is linked to intrinsically generated persistent firing. *bioRxiv*.

Kramis, R., Vanderwolf, C., and Bland, B. (1975). Two types of hippocampal rhythmical slow activity in both the rabbit and the rat: Relations to behavior and effects of atropine, diethyl ether, urethane, and pentobarbital. *Experimental Neurology*, 49:58–85.

Kriener, B., Helias, M., Rotter, S., Diesmann, M., and Einevoll, G. T. (2014). How pattern formation in ring networks of excitatory and inhibitory spiking neurons depends on the input current regime. *Front. Comput. Neurosci.*, 7(187):187.

Kropff, E., Carmichael, J. E., Moser, E. I., and Moser, M.-B. (2021). Frequency of theta rhythm is controlled by acceleration, but not speed, in running rats. *Neuron*, 109.

Kubota, K., Iwamoto, T., and Suzuki, H. (1974). Visuokinetic activities of primate prefrontal neurons during delayed response performance. *Journal of Neurophysiology*, 37:1197–1212.

Köster, M., Finger, H., Graetz, S., Kater, M., and Gruber, T. (2018). Theta-gamma coupling binds visual perceptual features in an associative memory task. *Scientific Reports*, 8:1–9.

Lapicque, L. (1907). Recherches quantitatives sur l'excitation electrique des nerfs traitee comme une polarization. *J. Physiol. Pathol. Gen.*, 9:620–635.

Latham, P. E., Richmond, B. J., Nelson, P. G., and Nirenberg, S. (2000). Intrinsic dynamics in neuronal networks. I. Theory. *J. Neurophysiol.*, 83:808–827.

Layer, M., Senk, J., Essink, S., Korvasová, K., van Meegen, A., Bos, H., Schuecker, J., and Helias, M. (2020). LIF Meanfield Tools (Version v0.2). Zenodo.

Leao, R. N., Targino, Z. H., Colom, L. V., and Fisahn, A. (2015). Interconnection and synchronization of neuronal populations in the mouse medial septum/diagonal band of brocca. *Journal of neurophysiology*, 1986:jn.00367.2014.

Lein, E. S., Hawrylycz, M. J., Ao, N., Ayres, M., Bensinger, A., Bernard, A., Boe, A. F., Boguski, M. S., Brockway, K. S., Byrnes, E. J., Chen, L., Chen, L., Chen, T. M., Chin, M. C., Chong, J., Crook, B. E., Czaplinska, A., Dang, C. N., Datta,

S., Dee, N. R., Desaki, A. L., Desta, T., Diep, E., Dolbeare, T. A., Donelan, M. J., Dong, H. W., Dougherty, J. G., Duncan, B. J., Ebbert, A. J., Eichele, G., Estin, L. K., Faber, C., Facer, B. A., Fields, R., Fischer, S. R., Fliss, T. P., Frensley, C., Gates, S. N., Glattfelder, K. J., Halverson, K. R., Hart, M. R., Hohmann, J. G., Howell, M. P., Jeung, D. P., Johnson, R. A., Karr, P. T., Kawal, R., Kidney, J. M., Knapik, R. H., Kuan, C. L., Lake, J. H., Laramee, A. R., Larsen, K. D., Lau, C., Lemon, T. A., Liang, A. J., Liu, Y., Luong, L. T., Michaels, J., Morgan, J. J., Morgan, R. J., Mortrud, M. T., Mosqueda, N. F., Ng, L. L., Ng, R., Orta, G. J., Overly, C. C., Pak, T. H., Parry, S. E., Pathak, S. D., Pearson, O. C., Puchalski, R. B., Riley, Z. L., Rockett, H. R., Rowland, S. A., Royall, J. J., Ruiz, M. J., Sarno, N. R., Schaffnit, K., Shapovalova, N. V., Sivisay, T., Slaughterbeck, C. R., Smith, S. C., Smith, K. A., Smith, B. I., Sodt, A. J., Stewart, N. N., Stumpf, K. R., Sunkin, S. M., Sutram, M., Tam, A., Teemer, C. D., Thaller, C., Thompson, C. L., Varnam, L. R., Visel, A., Whitlock, R. M., Wohnoutka, P. E., Wolkey, C. K., Wong, V. Y., Wood, M., Yaylaoglu, M. B., Young, R. C., Youngstrom, B. L., Yuan, X. F., Zhang, B., Zwingman, T. A., and Jones, A. R. (2007). Genome-wide atlas of gene expression in the adult mouse brain. *Nature*, 445:168–176.

Leão, R. N., Mikulovic, S., Leão, K. E., Munguba, H., Gezelius, H., Enjin, A., Patra, K., Eriksson, A., Loew, L. M., Tort, A. B., and Kullander, K. (2012). Olm interneurons differentially modulate ca3 and entorhinal inputs to hippocampal ca1 neurons. *Nature Neuroscience*, 15:1524–1530.

Li, S., Zhou, X., Constantinidis, C., and Qi, X. L. (2020). Plasticity of persistent activity and its constraints. *Frontiers in Neural Circuits*, 14.

Lindner, B. and Schimansky-Geier, L. (2001). Transmission of noise coded versus additive signals through a neuronal ensemble. *Phys. Rev. Lett.*, 86:2934–2937.

Lipponen, A., Woldemichael, B. T., Gurevicius, K., and Tanila, H. (2012). Artificial theta stimulation impairs encoding of contextual fear memory. *PLoS ONE*, 7:e48506.

Lisman, J. E. and Jensen, O. (2013). The theta-gamma neural code. *Neuron*, 77:1002–1016.

Lu, C. and Henderson, Z. (2010). Nicotine induction of theta frequency oscillations in rodent hippocampus in vitro. *Neuroscience*, 166:84–93.

Lu, C. B., Ouyang, G., Henderson, Z., and Li, X. (2011). Induction of theta-frequency oscillations in the rat medial septal diagonal band slice by metabotropic glutamate receptor agonists. *Neuroscience*, 177:1–11.

Lubenov, E. V. and Siapas, A. G. (2009). Hippocampal theta oscillations are travelling waves. *Nature*, 459:534–539.

Luke, T. B., Barreto, E., and So, P. (2013). Complete classification of the macroscopic behavior of a heterogeneous network of theta neurons. *Neural Computation*, 25:3207–3234.

López-Madrona, V. J., Pérez-Montoyo, E., Álvarez Salvado, E., Moratal, D., Herreras, O., Pereda, E., Mirasso, C. R., and Canals, S. (2020). Different theta frameworks coexist in the rat hippocampus and are coordinated during memory-guided and novelty tasks. *eLife*, 9:1–35.

MacDonald, C. J., Lepage, K. Q., Eden, U. T., and Eichenbaum, H. (2011). Hippocampal "time cells" bridge the gap in memory for discontiguous events. *Neuron*, 71:737–749.

Maier, N., Morris, G., Johenning, F. W., and Schmitz, D. (2009). An approach for reliably investigating hippocampal sharp wave-ripples in vitro. *PLoS ONE*, 4:e6925.

Mamad, O., McNamara, H. M., Reilly, R. B., and Tsanov, M. (2015). Medial septum regulates the hippocampal spatial representation. *Frontiers in Behavioral Neuroscience*, 9.

Manseau, F., Danik, M., and Williams, S. (2005). A functional glutamatergic neurone network in the medial septum and diagonal band area. *Journal of Physiology*, 566:865–884.

Manseau, F., Goutagny, R., Danik, M., and Williams, S. (2008). The hippocamposeptal pathway generates rhythmic firing of gabaergic neurons in the medial septum and diagonal bands: An investigation using a complete septohippocampal preparation in vitro. *Journal of Neuroscience*, 28:4096–4107.

McFarland, W. L., Teitelbaum, H., and Hedges, E. K. (1975). Relationship between hippocampal theta activity and running speed in the rat. *Journal of Comparative and Physiological Psychology*, 88:324–328.

McLelland, D. and VanRullen, R. (2016). Theta-gamma coding meets communication-through-coherence: Neuronal oscillatory multiplexing theories reconciled. *PLoS Computational Biology*, 12:4–10.

McNaughton, N., Ruan, M., and Woodnorth, M. A. (2006). Restoring theta-like rythmicity in rats restores initial learning in the morris water maze. *Hippocampus*, 16:1102–1110.

Mehring, C., Hehl, U., Kubo, M., Diesmann, M., and Aertsen, A. (2003). Activity dynamics and propagation of synchronous spiking in locally connected random networks. *Biol. Cybern.*, 88(5):395–408.

Mikulovic, S., Restrepo, C. E., Siwani, S., Bauer, P., Pupe, S., Tort, A. B. L., Kullander, K., and Leão, R. N. (2018). Ventral hippocampal olm cells control type 2 theta oscillations and response to predator odor. *Nature Communications*, 9:3638.

Mirollo, R. E. and Strogatz, S. H. (1990). Synchronization of pulse-coupled biological oscillators. *SIAM J. Appl. Math.*, 50(6):1645–1662.

Mizumori, S. J., Barnes, C. A., and McNaughton, B. L. (1989). Reversible inactivation of the medial septum: selective effects on the spontaneous unit activity of different hippocampal cell types. *Brain Research*, 500:99–106.

Muller, L., Chavane, F., Reynolds, J., and Sejnowski, T. J. (2018). Cortical travelling waves: mechanisms and computational principles. *Nat. Rev. Neurosci.*, 19(5):255–268.

Muller, L. and Destexhe, A. (2012). Propagating waves in thalamus, cortex and the thalamocortical system: Experiments and models. *J. Physiol. (Paris)*, 106(5-6):222–238.

Müller, C. and Remy, S. (2018). Septo–hippocampal interaction. *Cell and Tissue Research*, 373:565–575.

Nachstedt, T. and Tetzlaff, C. (2017). Working memory requires a combination of transient and attractor-dominated dynamics to process unreliably timed inputs. *Scientific Reports*, 7:1–14.

Navaroli, V. L., Zhao, Y., Boguszewski, P., and Brown, T. H. (2012). Muscarinic receptor activation enables persistent firing in pyramidal neurons from superficial layers of dorsal perirhinal cortex. *Hippocampus*, 22:1392–1404.

Nordlie, E., Gewaltig, M.-O., and Plesser, H. E. (2009). Towards reproducible descriptions of neuronal network models. *PLOS Comput. Biol.*, 5(8):e1000456.

Nordlie, E., Tetzlaff, T., and Einevoll, G. T. (2010). Rate dynamics of leaky integrate-and-fire neurons with strong synapses. *Front. Comput. Neurosci.*, 4:149.

Oddie, S. D. and Bland, B. H. (1998). Hippocampal formation theta activity and movement selection. *Neuroscience and Biobehavioral Reviews*, 22:221–231.

O'Keefe, J. (1976). Place units in the hippocampus of the freely moving rat. *Experimental Neurology*, 51:78–109.

O'Keefe, J. and Dostrovsky, J. (1971). The hippocampus as a spatial map: Preliminary evidence from unit activity in the freely moving rat. *Brain Research*, 34:171–175.

O'Keefe, J. and Recce, M. (1993). Phase relationship between hippocampal place units and the eeg theta rhythm. *Hippocampus*, 3:317–330.

O'Neill, P. K., Gordon, J. A., and Sigurdsson, T. (2013). Theta oscillations in the medial prefrontal cortex are modulated by spatial working memory and synchronize with the hippocampus through its ventral subregion. *Journal of Neuroscience*, 33:14211–14224.

Ott, E. and Antonsen, T. M. (2008). Low dimensional behavior of large systems of globally coupled oscillators. *Chaos*, 18:037113.

Pastalkova, E., Itskov, V., Amarasingham, A., and Buzsáki, G. (2008). Internally generated cell assembly sequences in the rat hippocampus. *Science*, 321:1322–1327.

Patel, J., Fujisawa, S., Berényi, A., Royer, S., and Buzsáki, G. (2012). Traveling theta waves along the entire septotemporal axis of the hippocampus. *Neuron*, 75:410–417.

Paz, R., Bauer, E. P., and Paré, D. (2008). Theta synchronizes the activity of medial prefrontal neurons during learning. *Learning and Memory*, 15:524–531.

Penn, Y., Segal, M., and Moses, E. (2016). Network synchronization in hippocampal neurons. *Proceedings of the National Academy of Sciences of the United States of America*, 113:3341–3346.

Penttonen, M. and Buzsáki, G. (2003). Natural logarithmic relationship between brain oscillators. *Thalamus and Related Systems*, 2:145–152.

Perin, R., Berger, T. K., and Markram, H. (2011). A synaptic organizing principle for cortical neuronal groups. *Proc. Natl. Acad. Sci. USA*, 108(13):5419–5424.

Petsche, H., Gogolak, G., and van Zwieten, P. (1965). Rhythmicity of septal cell discharges at various levels of reticular excitation. *Electroencephalography and Clinical Neurophysiology*, 19:25–33.

Petsche, H., Stumpf, C., and Gogolak, G. (1962). The significance of the rabbit's septum as a relay station between the midbrain and the hippocampus i. the control of hippocampus arousal activity by the septum cells. *Electroencephalography and Clinical Neurophysiology*, 14:202–211.

Potjans, T. C. and Diesmann, M. (2014). The cell-type specific cortical microcircuit: Relating structure and activity in a full-scale spiking network model. *Cereb. Cortex*, 24(3):785–806.

Pressler, R. T. and Strowbridge, B. W. (2006). Blanes cells mediate persistent feedforward inhibition onto granule cells in the olfactory bulb. *Neuron*, 49:889–904.

Pryluk, R., Kfir, Y., Gelbard-Sagiv, H., Fried, I., and Correspondence, R. P. (2019). A tradeoff in the neural code across regions and species. *Cell*, 176:597–609.

Quilichini, P., Sirota, A., and Buzsáki, G. (2010). Intrinsic circuit organization and theta-gamma oscillation dynamics in the entorhinal cortex of the rat. *Journal of Neuroscience*, 30:11128–11142.

Quinn, L. K., Nitz, D. A., and Chiba, A. A. (2010). Learning-dependent dynamics of beta-frequency oscillations in the basal forebrain of rats. *European Journal of Neuroscience*, 32:1507–1515.

Ray, S. and Maunsell, J. H. R. (2010). Differences in gamma frequencies across visual cortex restrict their possible use in computation. *Neuron*, 67(5):885–896.

Ricciardi, L. M., Di Crescenzo, A., Giorno, V., and Nobile, A. G. (1999). An outline of theoretical and algorithmic approaches to first passage time problems with applications to biological modeling. *Math. Japonica*, 50(2):247–322.

Risken, H. (1996). *The Fokker-Planck Equation*. Springer Verlag Berlin Heidelberg.

Robinson, J., Manseau, F., Ducharme, G., Amilhon, B., Vigneault, E., Mestikawy, S. E., and Williams, S. (2016). Optogenetic activation of septal glutamatergic neurons drive hippocampal theta rhythms. *Journal of Neuroscience*, 36:3016–3023.

Roland, J. J., Stewart, A. L., Janke, K. L., Gielow, M. R., Kostek, J. A., Savage, L. M., Servatius, R. J., and Pang, K. C. (2014). Medial septum-diagonal band of broca (msdb) gabaergic regulation of hippocampal acetylcholine efflux is dependent on cognitive demands. *Journal of Neuroscience*, 34:506–514.

Rosenbaum, R. and Doiron, B. (2014). Balanced networks of spiking neurons with spatially dependent recurrent connections. *Phys. Rev. X*, 4(2):021039.

Rosenbaum, R., Smith, M. A., Kohn, A., Rubin, J. E., and Doiron, B. (2017). The spatial structure of correlated neuronal variability. *Nat. Neurosci.*, 20(1):107–114.

Roxin, A., Brunel, N., and Hansel, D. (2005). The role of delays in shaping spatiotemporal dynamics of neuronal activity in large networks. *Phys. Rev. Lett.*, 94(23):238103.

Roxin, A., Brunel, N., and Hansel, D. (2006). Rate models with delays and the dynamics of large networks of spiking neurons. *Prog. Theor. Phys. Supp.*, 161:68–85.

Sainsbury, R. S., Heynen, A., and Montoya, C. P. (1987). Behavioral correlates of hippocampal type 2 theta in the rat. *Physiology and Behavior*, 39:513–519.

Schluppeck, D., Curtis, C. E., Glimcher, P. W., and Heeger, D. J. (2006). Sustained activity in topographic areas of human posterior parietal cortex during memory-guided saccades. *Journal of Neuroscience*, 26:5098–5108.

Schneider, M., Dann, B., Sheshadri, S., Scherberger, H., and Vinck, M. (2020). A general theory of coherence between brain areas. *bioRxiv*, page 2020.06.17.156190.

Schnepel, P., Kumar, A., Zohar, M., Aertsen, A., and Boucsein, C. (2015). Physiology and impact of horizontal connections in rat neocortex. *Cereb. Cortex*, 25(10):3818–3835.

Schuecker, J., Diesmann, M., and Helias, M. (2015). Modulated escape from a metastable state driven by colored noise. *Phys. Rev. E*, 92:052119.

Schwalger, T., Deger, M., and Gerstner, W. (2017). Towards a theory of cortical columns: From spiking neurons to interacting neural populations of finite size. *PLOS Comput. Biol.*, 13(4):e1005507.

Sejnowski, T. and Paulsen, O. (2006). Network oscillations: Emerging computational principles. *The Journal of Neuroscience*, 26:1673–1676.

Senk, J., Korvasová, K., Schuecker, J., Hagen, E., Tetzlaff, T., Diesmann, M., and Helias, M. (2020a). Conditions for wave trains in spiking neural networks. *Phys. Rev. Research*, 2:023174.

Senk, J., Korvasová, K., Schuecker, J., Hagen, E., Tetzlaff, T., Diesmann, M., and Helias, M. (2020b). Wave trains. Zenodo.

Seo, H., Barraclough, D. J., and Lee, D. (2007). Dynamic signals related to choices and outcomes in the dorsolateral prefrontal cortex. *Cerebral Cortex*, 17:i110–i117.

Seo, H., Barraclough, D. J., and Lee, D. (2009). Lateral intraparietal cortex and reinforcement learning during a mixed-strategy game. *Journal of Neuroscience*, 29:7278–7279.

Shirvalkar, P. R., Rapp, P. R., and Shapiro, M. L. (2010). Bidirectional changes to hippocampal theta-gamma comodulation predict memory for recent spatial episodes. *Proceedings of the National Academy of Sciences of the United States of America*, 107:7054–7059.

Simon, A. P., Poindessous-Jazat, F., Dutar, P., Epelbaum, J., and Bassant, M. H. (2006). Firing properties of anatomically identified neurons in the medial septum of anesthetized and unanesthetized restrained rats. *Journal of Neuroscience*, 26:9038–9046.

Singer, W. (1999). Neural synchrony: a versatile code for the definition of relations. *Neuron*, 24:49–65.

Singer, W. (2000). Response synchronization, a universal coding strategy for the definition of relations. In Gazzaniga, M. S., editor, *The Cognitive Neurosciences*. MIT Press, second edition.

Singer, W. (2018). Neuronal oscillations: unavoidable and useful? *European Journal of Neuroscience*, 48:2389–2398.

Singer, W. and Gray, C. (1995). Visual feature integration and the temporal correlation hypothesis. *Annu. Rev. Neurosci.*, 18:555–586.

Skaggs, W. E., McNaughton, B. L., Wilson, M. A., and Barnes, C. A. (1996). Theta phase precession in hippocampal neuronal populations and the compression of temporal sequences. *Hippocampus*, 6:149–172.

Skinner, F. K., Wu, C., and Zhang, L. (2001). Phase-coupled oscillator models can predict hippocampal inhibitory synaptic connections. *European Journal of Neuroscience*, 13:2183–2194.

Sosulina, L., Mittag, M., Geis, H.-R., Hoffmann, K., Klyubin, I., Qi, Y., Steffen, J., Friedrichs, D., Henneberg, N., Fuhrmann, F., Justus, D., Keppler, K., Cuello, A. C., Rowan, M. J., Fuhrmann, M., and Remy, S. (2021). Hippocampal hyperactivity in a rat model of alzheimer's disease. *Journal of Neurochemistry*.

Spaak, E. and de Lange, F. P. (2020). Hippocampal and prefrontal theta-band mechanisms underpin implicit spatial context learning. *Journal of Neuroscience*, 40:191–202.

Srimal, R. and Curtis, C. E. (2008). Persistent neural activity during the maintenance of spatial position in working memory. *NeuroImage*, 39:455–468.

Stein, R. B. (1967). Some models of neuronal variability. *Biophys. J.*, 7(1):37–68.

Sun, Y. J., Kim, Y.-J., Ibrahim, L. A., Tao, H. W., and Zhang, L. I. (2013). Synaptic mechanisms underlying functional dichotomy between intrinsic-bursting and regular-spiking neurons in auditory cortical layer 5. *Journal of Neuroscience*, 33(12):5326–5339.

Supèr, H., Spekreijse, H., and Lamme, V. A. (2001). A neural correlate of working memory in the monkey primary visual cortex. *Science*, 293:120–124.

Swanson, L. W. and Cowan, W. M. (1979). The connections of the septal region in the rat. *The Journal of Comparative Neurology*, 186:621–655.

Swanson, L. W. and Risold, P.-Y. (2000). *On the Basic Architecture of the Septal Region*. Springer New York.

Takeuchi, Y., Harangozo, M., Pedraza, L., Foldi, T., Kozak, G., and Berenyi, A. (2020). Closed-loop stimulation of the medial septum terminates epilepsy seizures

in rats. *Proceedings for Annual Meeting of The Japanese Pharmacological Society*, 93:3–O–103.

Teitelbaum, H., Lee, J. F., and Johannessen, J. N. (1975). Behaviorally evoked hippocampal theta waves: A cholinergic response. *Science*, 188:1114–1116.

Tingley, D., Alexander, A. S., Quinn, L. K., Chiba, A. A., and Nitz, D. (2018). Multiplexed oscillations and phase rate coding in the basal forebrain. *Science Advances*, 4:eaar3230.

Tingley, D. and Buzsáki, G. (2018). Transformation of a spatial map across the hippocampal-lateral septal circuit. *Neuron*, 98:1229–1242.e5.

Todd, J. J. and Marois, R. (2004). Capacity limit of visual short-term memory in human posterior parietal cortex. *Nature*, 428:751–754.

Tort, A. B., Kramer, M. A., Thorn, C., Gibson, D. J., Kubota, Y., Graybiel, A. M., and Kopell, N. J. (2008). Dynamic cross-frequency couplings of local field potential oscillations in rat striatum and hippocampus during performance of a t-maze task. *Proceedings of the National Academy of Sciences of the United States of America*, 105:20517–20522.

Tort, A. B. L., Komorowskie, R. W., Manns, J. R., Kopell, N. J., and Eichenbaum, H. (2009). Theta-gamma coupling increases during the learning of item-context associations. *Proc. Natl. Acad. Sci. USA*, 106(49):20942–20947.

Tsanov, M. (2018). Differential and complementary roles of medial and lateral septum in the orchestration of limbic oscillations and signal integration. *European Journal of Neuroscience*, 48:2783–2794.

Turing, A. M. (1952). The chemical basis of morphogenesis. *Phil. Transact. Royal Soc.*, 237:37–72.

Turnbull, J., Jiang, F., and Racine, R. (1994). Hippocampal stimulation of fornical-lesioned rats improves working memory. *Canadian Journal of Neurological Sciences / Journal Canadien des Sciences Neurologiques*, 21:100–103.

Vandecasteele, M., Varga, V., Berényi, A., Papp, E., Barthó, P., Venance, L., Freund, T. F., and Buzsáki, G. (2014). Optogenetic activation of septal cholinergic neurons suppresses sharp wave ripples and enhances theta oscillations in the hippocampus. *Proceedings of the National Academy of Sciences of the United States of America*, 111:13535–13540.

Vanderwolf, C. H. (1969). Hippocampal electrical activity and voluntary movement in the rat. *Electroencephalography and Clinical Neurophysiology*, 26:407–418.

Varga, V., Hangya, B., Kránitz, K., Ludányi, A., Zemankovics, R., Katona, I., Shigemoto, R., Freund, T. F., and Borhegyi, Z. (2008). The presence of pacemaker hcn channels identifies theta rhythmic gabaergic neurons in the medial septum. *Journal of Physiology*, 586:3893–3915.

Veltz, R. (2011). An analytical method for computing hopf bifurcation curves in neural field networks with space-dependent delays. *C. R. Math.*, 349(13-14):749–752.

Veltz, R. (2013). Interplay between synaptic delays and propagation delays in neural field equations. *SIAM J. Appl. Dyn. Syst.*, 12(3):1566–1612.

Veltz, R. and Faugeras, O. (2011). Stability of the stationary solutions of neural field equations with propagation delays. *J. Math. Neurosci.*, 1(1):1.

Venkov, N. A., Coombes, S., and Matthews, P. C. (2007). Dynamic instabilities in scalar neural field equations with space-dependent delays. *Physica D*, 232(1):1–15.

Vinogradova, O. S. (1995). Expression, control, and probable functional significance of the neuronal theta-rhythm. *Progress in Neurobiology*, 45:523–583.

Vivekananda, U., Bush, D., Bisby, J. A., Baxendale, S., Rodionov, R., Diehl, B., Chowdhury, F. A., McEvoy, A. W., Miserocchi, A., Walker, M. C., and Burgess, N. (2020). Theta power and theta-gamma coupling support long-term spatial memory retrieval. *Hippocampus*, 31.

Voges, N. and Perrinet, L. (2012). Complex dynamics in recurrent cortical networks based on spatially realistic connectivities. *Front. Comput. Neurosci.*, 6:41.

Wang, Y., Romani, S., Lustig, B., Leonardo, A., and Pastalkova, E. (2015). Theta sequences are essential for internally generated hippocampal firing fields. *Nature Neuroscience*, 18:282–288.

Wells, C. E., Amos, D. P., Jeewajee, A., Douchamps, V., Rodgers, J., O'Keefe, J., Burgess, N., and Lever, C. (2013). Novelty and anxiolytic drugs dissociate two components of hippocampal theta in behaving rats. *Journal of Neuroscience*, 33:8650–8667.

Wen, D., Peng, C., xiang Ou-yang, G., Henderson, Z., li Li, X., and biao Lu, C. (2013). Effects of nicotine stimulation on spikes, theta frequency oscillations, and spike-theta oscillation relationship in rat medial septum diagonal band broca slices. *Acta Pharmacologica Sinica*, 34:464–472.

Whishaw, I. Q. and Vanderwolf, C. H. (1973). Hippocampal eeg and behavior: Change in amplitude and frequency of rsa (theta rhythm) associated with spontaneous and learned movement patterns in rats and cats. *Behavioral Biology*, 8:461–484.

Wilson, H. R. and Cowan, J. D. (1972a). Excitatory and inhibitory interactions in localized populations of model neurons. *Biophysical Journal*, 12(1):1 – 24.

Wilson, H. R. and Cowan, J. D. (1972b). Excitatory and inhibitory interactions in localized populations of model neurons. *Biophys. J.*, 12(1):1–24.

Wilson, H. R. and Cowan, J. D. (1973a). A mathematical theory of the functional dynamics of cortical and thalamic nervous tissue. *Kybernetik*, 13(2):55–80.

Wilson, H. R. and Cowan, J. D. (1973b). A mathematical theory of the functional dynamics of cortical and thalamic nervous tissue. *Kybernetik*, 13(2):55–80.

Winson, J. (1978). Loss of hippocampal theta rhythm results in spatial memory deficit in the rat. *Science*, 201:160–163.

Witter, M. P. and Amaral, D. G. (2004). Hippocampal formation. *The Rat Nervous System*, pages 635–704.

Wyller, J., Blomquist, P., and Einevoll, G. T. (2007a). On the origin and properties of two-population neural field models - a tutorial introduction. *Biophys. Rev. Lett.*, 02(01):79–98.

Wyller, J., Blomquist, P., and Einevoll, G. T. (2007b). Turing instability and pattern formation in a two-population neuronal network model. *Physica D*, 225(1):75–93.

Yamakawa, G. R., Basu, P., Cortese, F., MacDonnell, J., Whalley, D., Smith, V. M., and Antle, M. C. (2016). The cholinergic forebrain arousal system acts directly on the circadian pacemaker. *Proceedings of the National Academy of Sciences of the United States of America*, 113:13498–13503.

Yger, P., El Boustani, S., Destexhe, A., and Frégnac, Y. (2011). Topologically invariant macroscopic statistics in balanced networks of conductance-based integrate-and-fire neurons. *J. Comput. Neurosci.*, 31:229–245.

Yoshida, M. and Hasselmo, M. E. (2009). Persistent firing supported by an intrinsic cellular mechanism in a component of the head direction system. *Journal of Neuroscience*, 29:4945–4952.

Zhang, G.-W., Shen, L., Zhong, W., Xiong, Y., Zhang, L. I., and Tao, H. W. (2018). Transforming sensory cues into aversive emotion via septal-habenular pathway. *Neuron*, 99:1016–1028.e5.

Zhang, H. and Jacobs, J. (2015). Traveling theta waves in the human hippocampus. *The Journal of neuroscience : the official journal of the Society for Neuroscience*, 35:12477–87.

Zhang, H., Lin, S. C., and Nicolelis, M. A. (2010). Spatiotemporal coupling between hippocampal acetylcholine release and theta oscillations in vivo. *Journal of Neuroscience*, 30:13431–13440.

Zhou, Y. D. and Fuster, J. M. (1996). Mnemonic neuronal activity in somatosensory cortex. *Proceedings of the National Academy of Sciences of the United States of America*, 93:10533–10537.

Zutshi, I., Brandon, M. P., Fu, M. L., Donegan, M. L., Leutgeb, J. K., and Leutgeb, S. (2018). Hippocampal neural circuits respond to optogenetic pacing of theta frequencies by generating accelerated oscillation frequencies. *Current Biology*, 28:1179–1188.e3.

Zylberberg, J. and Strowbridge, B. W. (2017). Mechanisms of persistent activity in cortical circuits: Possible neural substrates for working memory. *Annual Review of Neuroscience*, 40:603–627.

Band / Volume 72
Three-Dimensional Polymeric Topographies for Neural Interfaces
F. Milos (2021), 133 pp
ISBN: 978-3-95806-586-4

Band / Volume 73
Development, characterization, and application of compliantintracortical implants
K. Srikantharajah (2021), xiv, 155, xv-xvii pp
ISBN: 978-3-95806-587-1

Band / Volume 74
Modelling, implementation and characterization of a Bias-DAC in CMOS as a building block for scalable cryogenic control electronics for future quantum computers
P. N. Vliex (2021), xiv, 107, xv-xxviii pp
ISBN: 978-3-95806-588-8

Band / Volume 75
Development of Electrochemical Aptasensors for the Highly Sensitive, Selective, and Discriminatory Detection of Malaria Biomarkers
G. Figueroa Miranda (2021), XI, 135 pp
ISBN: 978-3-95806-589-5

Band / Volume 76
Nanostraw- Nanocavity MEAs as a new tool for long-term and high sensitive recording of neuronal signals
P. Shokoohimehr (2021), xi, 136 pp
ISBN: 978-3-95806-593-2

Band / Volume 77
Surface plasmon-enhanced molecular switching for optoelectronic applications
B. Lenyk (2021), x, 129 pp
ISBN: 978-3-95806-595-6

Band / Volume 78
Engineering neuronal networks in vitro: From single cells to population connectivity
I. Tihaa (2021), viii, 242 pp
ISBN: 978-3-95806-597-0

Band / Volume 79
Spectromicroscopic investigation of local redox processes in resistive switching transition metal oxides
T. Heisig (2022), vi, 186 pp
ISBN: 978-3-95806-609-0

Band / Volume 80
Integrated Control Electronics for Qubits at Ultra Low Temperature
D. Nielinger (2022), xviii, 94, xix-xxvi
ISBN: 978-3-95806-631-1

Band / Volume 81
Higher-order correlation analysis in massively parallel recordings in behaving monkey
A. Stella (2022), xiv, 184 pp
ISBN: 978-3-95806-640-3

Band / Volume 82
Denoising with Quantum Machine Learning
J. Pazem (2022), 106 pp
ISBN: 978-3-95806-641-0

Band / Volume 83
Hybrid hydrogels promote physiological functionality of long-term cultured primary neuronal cells in vitro
C. Meeßen (2022), x, 120 pp
ISBN: 978-3-95806-643-4

Band / Volume 84
Surface states and Fermi-level pinning on non-polar binary and ternary (Al,Ga)N surfaces
L. Freter (2022), 137 pp
ISBN: 978-3-95806-644-1

Band / Volume 85
Dynamical and statistical structure of spatially organized neuronal networks
M. Layer (2022), xiii, 167 pp
ISBN: 978-3-95806-651-9

Band / Volume 86
Persistent firing and oscillations in the septo-hippocampal system and their relation to locomotion
K. Korvasová (2022), 111 pp
ISBN: 978-3-95806-654-0

Information
Band / Volume 86
ISBN 978-3-95806-654-0

Mitglied der Helmholtz-Gemeinschaft

JÜLICH
Forschungszentrum